Modeling and Validation of Particle Drying and Coating in a Continuously Operated Horizontal Fluidized Bed

Dissertation
zur Erlangung des akademischen Grades

Doktoringenieur
Dr.-Ing.

von **MSc Kaicheng Chen**
geb. am 19.11.1988 in Fujian, China

genehmigt durch die Fakultät für Verfahrens- und Systemtechnik
der Otto-von-Guericke-Universität Magdeburg

Promotionskommission	Prof. Dr. Berend van Wachem (Vorsitz)
	Prof. Dr.-Ing. habil. Evangelos Tsotsas (Gutachter)
	Prof. Dr.-Ing. Andreas Bück (Gutachter)
	Dr.-Ing. Michael Jacob (Gutachter)
eingereicht am:	07. August 2019
Promotionskolloquium am:	24. Januar 2020

Declaration

I hereby declare that the dissertation with the title:

Modeling and Validation of Particle Drying and Coating in a Continuously Operated Horizontal Fluidized Bed

is my own work and effort and that it has not been submitted anywhere for any purpose. Where other sources of facts or ideas have been used, either directly or indirectly, they have been clearly stated.

The work has not been submitted in the same or a similar form to any other testing authority and has also not yet been published anywhere.

Magdeburg, August 07, 2019
MSc Kaicheng Chen

Abstract

Horizontal fluidized bed is a type of commonly used apparatus for material drying and particle formation processes in industry. In contrast with the batch device, one significant advantage of such fluidized bed is that it can achieve high throughput by being operated continuously.

However, the continuous process has typically some specific features, for instance, an uneven residence time distribution (RTD) of particles. A broad distribution of residence time among particles is usually unfavorable, in particular for materials which are sensitive to the process duration. Accordingly, RTD is one of the most important aspects when investigating continuous processes. In the present work, the RTDs of γ-Al_2O_3 particles in a pilot scale fluidized bed were firstly experimentally measured. The same material and device were used for the upcoming drying and coating researches as well. The influences of various operation and configuration parameters on the RTD of the particles were discussed. In order to obtain characteristic properties of the RTD, e.g., the dispersion coefficient of the particles and the number of theoretical tanks, numerical models were solved. Later, two alternative methods, the species method and the multi-solid method, were developed for estimating particle RTD via computational fluid dynamics (CFD). The results indicate that both methods are able to simulate particle RTD in the transient CFD mode. The complex interrelation between particle diffusivity and dispersion coefficient was then discussed on the basis of the simulation results. Moreover, possibilities for accelerating the simulation were addressed.

The second research focus of this study is the modeling of the particle drying process in a horizontal fluidized bed. Several drying experiments have been used for model validation. The moisture content distribution and RTD of wet particles were measured in these experiments. The influence of some

geometrical parameters (e.g., outlet weir height and internal baffles) on the RTD of wet particles was qualitatively discussed and compared with the corresponding results of dry particles. On the basis of a single particle drying approach combined with different particle flow assumptions in the horizontal fluidized bed, in total five drying models were developed: plug flow (PF) model, continuous-flow stirred-tank reactor model, tank-in-series mixed flow model, one dimensional population balance drying model and two dimensional population balance drying (2D-PBD) model. Simulation results from each model were not only compared with experimental data but also with each other. The particular meaning of each model was discussed. Finally, the influences of operation parameters on the particle drying process in the horizontal fluidized bed were evaluated in the frame of parameter studies based on the PF and 2D-PBD models.

Spray coating, an essential branch of the wet formulation of particles, is applied when it is necessary to change the surface properties of a specific particulate material. The last investigation of the present work concerned the modeling of particle coating process in a horizontal fluidized bed. Like in the development of the drying model, coating experiments from our group were applied for validation of the model. In these experiments, γ-Al_2O_3 particles were coated with sodium benzoate solution, and the corresponding particle size distributions (PSDs) at the inlet and outlet were respectively attained. To account for the particle back-mixing effect in the horizontal fluidized bed, a single particle coating model was expanded into a one-dimensional population balance coating model that considers the particle RTD. Moreover, it was found that the RTD of particles under specific conditions could be accurately determined using recently developed empirical correlations. Later, the PSD was implemented as a second dimension of the population balance to the model. The simulation results from both models were validated and discussed by comparing with the experimental data. Generally, the two-dimensional population balance coating model provided more reliable results. Lastly, the influences of different operating and geometric parameters (outlet weir height, superficial gas velocity, etc.) on the PSD of the coated particles were investigated via model-based numerical experiments.

Kurzzusammenfassung

Die horizontale Wirbelschicht ist eine Apparatur, die sehr häufig für Materialtrocknungsprozesse und Partikelformulierungsprozesse in der Industrie ihren Einsatz findet. Im Gegensatz zu Wirbelschichten, die absatzweise betrieben werden, besteht ein wesentlicher Vorteil einer horizontalen Wirbelschicht darin, dass durch den kontinuierlichen Betrieb ein hoher Durchsatz erreicht werden kann.

Ein kontinuierlicher Prozess hat jedoch einige charakteristische Merkmale; beispielsweise treten ungleichmäßige Verweilzeitverteilungen (RTD) der behandelten Partikel auf. Eine breite Verteilung der Verweilzeit der Partikel ist in der Regel ungünstig, insbesondere für empfindliche Materialien, die einer langen Prozessdauer ausgesetzt sind. Daher ist die RTD eine der wichtigsten Aspekte bei der Untersuchung von kontinuierlichen Prozessen.

In der vorliegenden Arbeit wurden zunächst die Verweilzeitverteilungen von γ-Al_2O_3-Partikeln in einer pilotmaßstäblichen Wirbelschicht experimentell vermessen. Für nachfolgende Trocknungs- und Beschichtungsversuche wurde sowohl die gleiche Anlage als auch das gleiche Versuchsmaterial verwendet. Die Einflüsse verschiedener Betriebs- und Konfigurationsparameter auf die RTD der Partikel wurden jeweils diskutiert. Um charakteristische Eigenschaften der RTD zu erhalten, z. B. den Dispersionskoeffizienten der Partikel und die Anzahl der theoretischen Stufen, wurden numerische Modelle aufgestellt. Es folgte die Entwicklung zweier alternativen Methoden, der Speziesmethode und der Multi-Solid-Methode, um die RTD der Partikel mithilfe der CFD (Computational Fluid Dynamics) zu erhalten. Anhand der Simulationsergebnisse konnte gezeigt werden, dass beide Methoden die Partikel-RTD im transienten CFD-Modus simulieren können. Der komplexe Zusammenhang zwischen Partikeldiffusivität und Dispersionskoeffizienten wurde auf Basis der Simulationsergebnisse

diskutiert, sowie Möglichkeiten der Beschleunigung der Simulationen betrachtet.

Der zweite Forschungsschwerpunkt dieser Studie betrat die Modellierung des Trocknungsprozesses von Partikeln in einer horizontalen Wirbelschicht. Zur anschließenden Modellvalidierung wurden mehrere Trocknungsexperimente verwendet. Die Feuchteverteilung und die RTD von feuchten γ-Al_2O_3-Partikeln wurden in diesen Experimenten gemessen. Der Einfluss geometrischer Parameter (z. B. Austrittsüberlaufhöhe und innere Wehre) auf die RTD von feuchten Partikeln wurde qualitativ diskutiert und mit entsprechenden Ergebnissen von trockenen Partikeln verglichen. Auf der Grundlage eines Einzelpartikel-Trocknungsansatzes kombiniert mit unterschiedlichen Partikelströmungsannahmen in der horizontalen Wirbelschicht wurden insgesamt fünf Trocknungsmodelle entwickelt: Kolbenströmungsmodell (PF-Modell), Rührkesselmodell, Rührkesselkaskademodell, eindimensionales Populationsbilanzmodell für die Trocknung und zweidimensionales Populationsbilanzmodell für die Trocknung (2D-PBD). Die Simulationsergebnisse jedes Modells wurden sowohl untereinander als auch mit den experimentellen Daten verglichen. Schließlich wurden die Einflüsse einiger Betriebsparameter auf den Trocknungsprozess der Partikel in der horizontalen Wirbelschicht jeweils in Parameterstudien auf der Grundlage der PF- und 2D-PBD-Modelle bewertet und diskutiert.

Sprühbeschichten ist wichtig in der Partikelformulierung und wird angewendet, wenn die Oberflächeneigenschaften eines bestimmten Partikelmaterials geändert werden müssen. Die letzte Untersuchung der vorliegenden Arbeit betraf die Modellierung des Partikelbeschichtungsprozesses in der horizontalen Wirbelschicht. Ähnlich wie bei der Entwicklung des Trocknungsmodells wurden Beschichtungsexperimente aus der Lehrstuhlliteratur zur Validierung des Modells eingesetzt. In diesen Experimenten wurden γ-Al_2O_3-Partikel mit Natriumbenzoat beschichtet und Partikelgrößenverteilungen (PSD) sowohl am Einlass als auch am Auslass bestimmt. Zur Beschreibung des Partikel-Rückvermischungseffekts in der horizontalen Wirbelschicht wurde ein Einzelpartikel-Beschichtungsmodell zu einem eindimensionalen Populationsbilanzmodell für das Coating erweitert, welches die Partikel-RTD berücksichtigt. Es wurde festgestellt, dass die RTD unter bestimmten Bedingungen mit Hilfe jüngst entwickelt empirischer Korrelationen genau bestimmt werden kann. Die PSD wurde folglich als zweite Dimension der Populationsbilanz in das Modell implementiert und die Simulationsergebnisse beider Modelle wurden validiert und vergleichend mit den experimentellen Daten diskutiert. Es stellte sich heraus,

dass das zweidimensionale Populationsbilanzmodell zuverlässigere Ergebnisse liefert. Abschließend wurden die Einflüsse verschiedener Betriebs- und Geometrieparameter (Austrittswehrhöhe, Leerrohrgeschwindigkeit usw.) auf die PSD der beschichteten Partikel durch modellbasierte numerische Experimente untersucht.

Contents

1 Background and Scope of the Work **1**
1.1 Overview . . . 1
1.2 Background . . . 1
1.2.1 Fluidization behavior . . . 1
1.2.2 Types of particulate solids . . . 3
1.2.3 Fluidized bed systems . . . 5
1.2.4 Particle drying in the fluidized bed . . . 7
1.2.5 Wet formulation of particles in fluidized beds . . . 9
1.3 Scope of the work . . . 12

2 Particle Residence Time Distribution in Horizontal Fluidized Bed **14**
2.1 Overview . . . 14
2.2 Fundamentals and theories for RTD research . . . 15
2.2.1 Plug flow, mixed flow, and back-mixing flow . . . 15
2.2.2 RTD measurement methodology . . . 15
2.2.3 The mean and variance . . . 16
2.2.4 The theoretical tank number and TIS model . . . 17
2.2.5 The dispersion coefficient and diffusion coefficient . . . 17
2.2.6 The dispersion model . . . 18
2.2.7 The Bodenstein number . . . 18
2.3 RTD experiments . . . 19
2.3.1 Previous work . . . 19
2.3.2 Apparatus . . . 21
2.3.3 Material . . . 21
2.3.4 RTD experiment series . . . 22
2.3.5 Experimental results . . . 23

2.3.6 Numerical results 24
2.3.6.1 TIS model 24
2.3.6.2 Dispersion model 27
2.4 Computational fluid dynamics (CFD) simulations 29
2.4.1 Previous RTD researches by CFD 29
2.4.2 Mathematical models 32
2.4.2.1 The Eulerian multiphase model 32
2.4.2.2 The governing equations for the gas phase . . . 32
2.4.2.3 The governing equations for the solid phase . . 34
2.4.2.4 The RTD simulations 36
2.4.3 Pre-simulation 37
2.4.3.1 Simulation conditions 37
2.4.3.2 Grid independence study 39
2.4.4 Main simulation 40
2.4.4.1 Mesh and settings 40
2.4.4.2 Validation of bed mass and mean residence time 41
2.4.4.3 RTD simulations: species method 42
2.4.4.4 RTD simulations: multi-solid method 47
2.4.4.5 Simulation acceleration 48
2.5 Conclusion 50

3 Particle Drying in Horizontal Fluidized Bed 52
3.1 Overview 52
3.2 Model development 53
3.2.1 Modeling of particle movement 53
3.2.1.1 Non-mixing flow: plug flow (PF) model 53
3.2.1.2 Mixing flow: mixed flow model and back-mixing flow model 54
3.2.2 Particle drying model 57
3.2.2.1 General assumptions 58
3.2.2.2 Drying kinetics 58
3.2.2.3 Balance equations of gas phase 60
3.2.2.4 Balance equations of wall 61
3.2.2.5 Hydrodynamic parameters of fluidized bed . . . 62
3.3 Experiments 63
3.3.1 Experimental apparatus and material 64

3.3.2 Experimental series . . . 64
3.3.3 Moisture content distribution . . . 64
3.3.4 Experimental results . . . 65
3.3.4.1 Drying experiments . . . 65
3.3.4.2 Residence time experiments . . . 67
3.4 Results and discussion . . . 69
3.4.1 The plug flow (PF) model . . . 69
3.4.1.1 Model validation . . . 69
3.4.1.2 Parametric study . . . 70
3.4.2 The mixed flow model . . . 73
3.4.3 The back-mixing flow model . . . 74
3.4.3.1 One-dimensional population balance drying (1D-PBD) model . . . 75
3.4.3.2 Two-dimensional population balance drying (2D-PBD) model . . . 77
3.4.3.3 Parametric study . . . 78
3.5 Conclusion . . . 82

4 Particle Coating in Horizontal Fluidized Bed 84
4.1 Introduction . . . 84
4.1.1 A review of fluidized bed coating . . . 84
4.1.2 Overview . . . 86
4.2 Model development . . . 87
4.2.1 General hypothesis . . . 87
4.2.2 One-dimensional population balance coating (1D-PBC) model . . . 88
4.2.3 Two-dimensional population balance coating (2D-PBC) model . . . 92
4.3 Reference work . . . 92
4.3.1 Experimental plant . . . 93
4.3.2 Experimental series . . . 93
4.3.3 Experimental data . . . 95
4.4 Simulation, results, and discussion . . . 96
4.4.1 Pre-simulation . . . 96
4.4.2 Model validation . . . 97
4.4.3 Parametric study . . . 99

4.5 Conclusion 105

5 Summary and Outlook **108**

5.1 Summary 108

5.2 Outlook 111

Bibliography **112**

Appendices **127**

A Gas-solid heat and mass transfer in fluidized bed 127

B Material values 128

B.1 Properties of dry air 128

B.2 Properties of wet air 130

Nomenclature

Symbols

a	Dimensionless ratio	$-$
A	Area	m^2
Ar	Archimedes number	$-$
A_V	Particle surface area per volume	$\mathrm{m}^2\mathrm{m}^{-3}$
Bo	Bodenstein number	$-$
c	Specific heat capacity	$\mathrm{Jkg}^{-1}\mathrm{K}^{-1}$
C	Mass fraction of tracer	kgkg^{-1}
C_D	Drag coefficient	$-$
$\tilde{C}$	Heat capacity	JK^{-1}
d	Diameter	m
D	Longitudinal dispersion coefficient of the particles	$\mathrm{m}^2\mathrm{s}^{-1}$
$\tilde{D}$	Diffusion coefficient	$\mathrm{m}^2\mathrm{s}^{-1}$
e	Restitution coefficient	$-$
E	Normalized mass fraction of tracer in the outflow for pulse input	s^{-1}
F	Normalized mass fraction of tracer in the outflow for step input	$-$
g_0	Radial distribution function	$-$
$\vec{g}$	Acceleration of gravity	ms^{-2}
G_k	Production of turbulent kinetic energy due to the mean velocity gradients	J
Δh_v	Specific enthalpy of vaporization	Jkg^{-1}
h	Specific enthalpy	Jkg^{-1}

$\bar{h}$	Average specific enthalpy	$\mathrm{Jkg^{-1}}$
H	Enthalpy	J
$\bar{H}$	Average enthalpy	J
$\tilde{H}$	Height	m
$\dot{H}$	Enthalpy flow rate	$\mathrm{Js^{-1}}$
$\bar{\bar{I}}$	Unit tensor	–
J	Number of classes in respect to residence time	–
$\vec{J}$	Diffusion flux	$\mathrm{kgm^{-2}s^{-1}}$
k	Kinetic energy per unit mass	$\mathrm{Jkg^{-1}}$
K	Number of theoretical tanks	–
$\vec{K}$	Interaction between phases	$\mathrm{kgm^{-2}s^{-3}}$
L	Length of the horizontal fluidized bed	m
Le	Lewis number	–
m	Exponent	–
M	Mass	kg
$\dot{M}$	Mass flow rate	$\mathrm{kgs^{-1}}$
$\tilde{M}$	Molecular mass	$\mathrm{kgkmol^{-1}}$
n	Number density function regarding residence time	$\mathrm{s^{-1}}$
$\tilde{n}$	Number density function regarding residence time and moisture content	$\mathrm{kgs^{-1}kg^{-1}}$
$\hat{n}$	Number density function regarding residence time and particle size	$\mathrm{s^{-1}m^{-1}}$
N	Number	–
Nu	Nusselt number	–
p	Pressure	Pa
Q_0	Normalized particle size distribution with respect to particle number	–
$\dot{Q}$	Heat flow rate	$\mathrm{Js^{-1}}$
R	Specific gas constant	$\mathrm{Jkg^{-1}K^{-1}}$
Re	Reynolds number	–
Pe	Peclet number	–
Pr	Prandtl number	–
Sc	Schmidt number	–
Sh	Sherwood number	–
t	Time	s

u	Velocity	ms^{-1}
$\vec{v}$	Velocity of the Eulerian phase in CFD simulation	ms^{-1}
V	Diffusion volume of simple molecule	$-$
$\tilde{V}$	Volume	m^3
W	Width of the horizontal fluidized bed	m
x	Mass fraction of the solute in the solution	kg/kg
X	Moisture content (solid phase)	kg/kg
$\bar{X}$	Mean moisture content (solid phase)	kg/kg
Y	Moisture content (gas phase)	kg/kg
z	Spatial coordinate (longitudinal direction)	m
$\tilde{z}$	Spatial coordinate (gas phase vertical direction)	m

Greek symbols

α	Volume fraction	$-$
$\tilde{\alpha}$	Heat transfer coefficient	$\mathrm{Wm}^{-2}\mathrm{K}^{-1}$
β	Interphase drag coefficients	$\mathrm{kgm}^{-3}\mathrm{s}^{-1}$
$\tilde{\beta}$	Mass transfer coefficient	ms^{-1}
γ	Collisional dissipation of energy	$\mathrm{kgm}^{-1}\mathrm{s}^{-3}$
δ	Relative error	$-$
$\bar{\delta}$	Average relative error	$-$
ε	Turbulent dissipation rate	$\mathrm{m}^2\mathrm{s}^{-3}$
η	Normalized particle moisture content	$-$
$\tilde{\eta}$	Drying potential	$-$
Θ	Granular temperature	$\mathrm{m}^2\mathrm{s}^{-2}$
λ	Bulk viscosity	Pas
$\tilde{\lambda}$	Thermal conductivity	$\mathrm{Wm}^{-1}\mathrm{K}^{-1}$
μ	Shear viscosity	Pas
μ_{tu}	Turbulent viscosity	Pas
$\tilde{\mu}$	Dynamic viscosity	Pas
ν	Kinematic viscosity	$\mathrm{m}^2\mathrm{s}^{-1}$
$\dot{\nu}$	Normalized particle drying rate	$-$
ξ	Dimensionless spatial coordinate (gas phase)	$-$
ρ	Density	kgm^{-3}

σ	Standard deviation of particle moisture content distribution (or residence time distribution, or particle size distribution)	kg/kg (or s, or m)
σ_k	Prandtl number for turbulence kinetic energy	−
σ_ε	Prandtl number for turbulence dissipation rate	−
σ^2	Variance of RTD curve	s^2
τ	Particle mean residence time	s
$\bar{\bar{\tau}}$	Stress-strain tensor	Pa
ψ	Porosity	−
ϑ	Temperature	K (or °C)

Subscripts

ab	Apparent bed
app	Apparatus
b	Bed
baffle	Internal baffle
bu	Bubble
c	Cross-sectional
col	Collision
cr	Critical
elu	Elutriation
eq	Equilibrium
exp	Experiment
fb	Fixed bed
g	Gas
gap	Gap
gs	Gas-solid
gp	Gas phase to particle phase
gW	Gas phase to wall
i	Particle class in respect to residence time
in	Inflow
j	j^{th} solid phase
k	k^{th} solid phase
kin	Kinetic
l	l^{th} control volume

lam	Laminar
m	Particle class in respect to moisture content
mat	Material
max	Maximum
mean	Mean
median	Median
mf	Minimum fluidization
nb	No internal baffle
of	Overflow
out	Outflow
p	Particle
pg	Particle phase to gas phase
pW	Particle phase to wall
pulse	Pulse input method
r	Reactor
rel	Relative
s	Solid
sat	Saturation
sh	Shell
sim	Simulation
sol	Solution
sp	Single particle
ss	Solid-solid
step	Step input method
t	Tracer
tot	Total
ts	Tracer-solid
tu	Turbulent
uf	Underflow
v	Vapor
w	Water
wet	Wet particle
weir	Outlet weir
W	Wall
We	Wall to environment
0	Initial moment

Abbreviations

1D	One-dimensional
2D	Two-dimensional
3D	Three-dimensional
BM	Benchmark
CFD	Computational fluid dynamics
CSTR	Continuous-flow stirred-tank reactor
IC	Initial condition
LL	Lower limit
MCD	Moisture content distribution
NMR	Nuclear magnetic resonance
No.	Number
PBM	Population balance model
PBC	Population balance coating
PBD	Population balance drying
PF	Plug flow
PS	Parameter study
PSD	Particle size distribution
RTD	Residence time distribution
Ser.	Series
TIS	Tank-in-series
TISMF	Tank-in-series mixed flow
UL	Upper limit

Chapter 1

Background and Scope of the Work

1.1 Overview

This chapter provides the necessary background for understanding the gas-solid fluidized bed system. The concept of fluidization phenomenon and the type of particulate solids, which could directly affect the gas-solid movement behavior in the fluidized bed, are first introduced. Then, since various fluidized beds have been developed for different industrial purposes, a general description of fluidized bed system is carried out, and later, is narrowed down to the fluidized beds specialized for the drying and formation of particles, which both are strictly related to the content of this work. Consequently, the drying and wet formation process of particles are explained further in detail. In the end, the goal and scope of this dissertation are specified.

1.2 Background

1.2.1 Fluidization behavior

Nowadays, gas-solid fluidized beds play an essential role in various industries, e.g., chemical, pharmaceutical, agricultural, food, etc.. In simple terms, a fluidized bed can be formed, when the process gas passes through a bed of solids on the air distributor with a certain velocity, and the phenomenon of the liquid-like movement of solids is named as fluidization. Normally, the hydrodynamic behavior of the solids in vertical direction (the direction of process gas) is directly related to the gas velocity. A rough classification of the types of fluidization was made by Grace (1986) and presented in Fig. 1.1. As

can be seen, except the extreme cases (the packed bed and the conveying of solids), the fluidization can coarsely be divided into two categories: aggregative fluidization and fast fluidization. Besides, aggregative fluidization can be further broken down into three types: a) bubbling fluidization; b) slugging fluidization; c) turbulent fluidization.

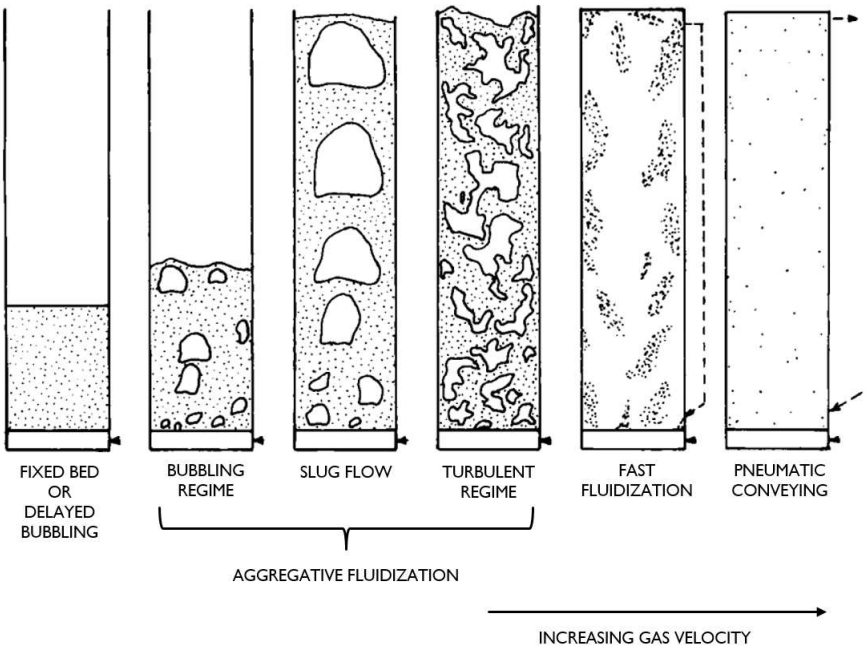

Figure 1.1: The scheme of various flow regimes of fluidization with increasing gas velocity (Grace (1986)).

Based on the work from Čatipović et al. (1978), van Deemter (1980), Horio et al. (1986) and Grace (1990), Kunii and Levenspiel (1991) mapped out the relationship between superficial gas velocity and particle size with the type of particle fluidization, as plotted in Fig. 1.2. It can be inferred that, on the one hand, pneumatic conveying is hard to be clearly distinguished from fast fluidization. In addition, an overlap of the flow regimes between turbulent fluidization and fast fluidization can also be observed, and accordingly, they are generalized as high-velocity fluidization by Kunii and Levenspiel (1991). On the other hand, due to slugging fluidization being usually unlikely to exist in industrial scale fluidized beds, the flow regime shifts directly from bubbling fluidization to turbulent fluidization in the map.

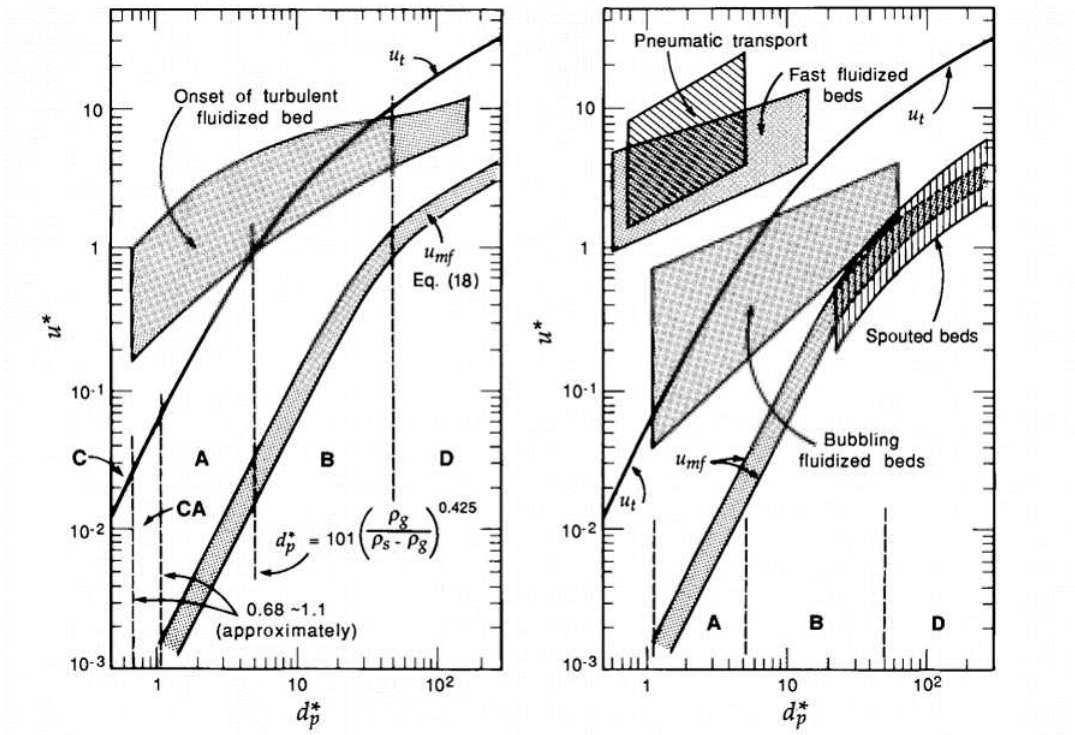

Figure 1.2: A summary of the relationships between different gas-solid flow regimes with dimensionless particle diameter d_p^* and dimensionless superficial gas velocity u^* by Kunii and Levenspiel (1991). (u_{mf} is the minimum fluidization velocity; u_t is the terminal free settling velocity; A, B, C, and D represent the classification of solids by Geldart (1973)).

1.2.2 Types of particulate solids

As has been shown in Fig. 1.2, the type of fluidization of solids depends not only on gas velocity but also on particle properties. On the basis of the fluidization behavior of particles made of different materials and having different sizes, Geldart (1973) carefully classified the particulate solids into four groups as follows:

- Group **A**: These solids are usually designated as aeratable powders. They are quite small and/or have a density smaller than 1400 kg/m^3. The bed of these powders, on the one side, would expand fast when the superficial gas velocity is larger than the minimum fluidization velocity but smaller than the velocity at which bubbles start to appear; on the other side, the expanded powders would have a slow deaeration rate (i.e., the expanded bed is hard to be collapsed) when the gas is suddenly switched off.

- Group **B**: The "sand-like" or bubbly powders, are powders which have a Sauter mean diameter in the range from 40 μm to 500 μm, whereas the particle density ranges from 1400 kg/m^3 to 4000 kg/m^3. In fluidized beds made of these powders, bubbles already appear at the minimum fluidization velocity. Moreover, the bed expansion rate is more moderate, and the bed deaeration rate is much faster in comparison with group A powders.

- Group **C**: The powders that belong to this group are extremely fine, soft and consequently quite cohesive. Therefore, such material is difficult to fluidize.

- Group **D**: In this group, the particles are large, coarse and/or dense. The gas flow pattern in a bed with these particles is different from that in group A and B powders. Accordingly, the bed expansion is low, and the particles are hard to fluidize in deep beds.

Particles from different Geldart groups with a variety of sizes and densities, which are fluidized in air at atmospheric temperature and pressure but have similar fluidization characteristics, have been summarized and plotted by Geldart (1973) (Fig. 1.3). A precise specification of each boundary between the adjacent groups in Fig. 1.3 was further given by Geldart (1986a).

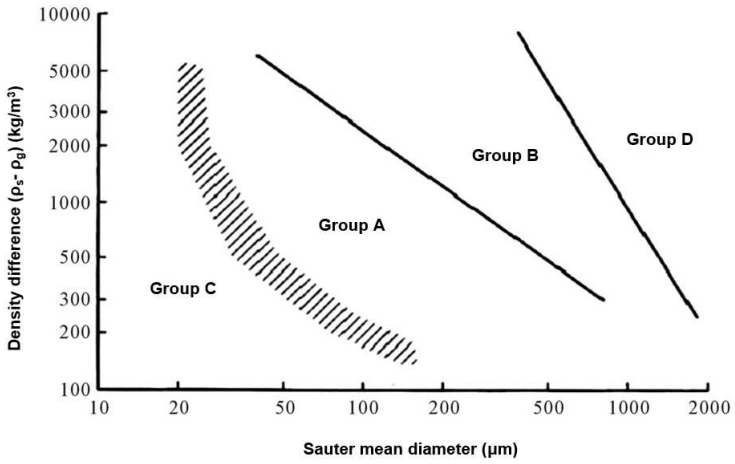

Figure 1.3: Diagram of the Geldart classification of particulate solids for fluidization in the air (Geldart (1973)).

In general, all particulate solids subjected to gas-solid fluidization can be classified based on the work from Geldart (1973, 1986a), which is meaningful

for the use and development of fluidized bed systems.

1.2.3 Fluidized bed systems

The fluidized bed system has a nearly one-century development history, as stated by Geldart (1986b). The fluidization technique was firstly used for coal gasification in 1926, and fluidized bed systems became widely used in commercial applications from the 1940s. According to the data collected by Zens (1997), fluidized bed systems have often been applied for chemical operations in various industrial applications. A typical chemical process conducted in a fluidized bed is the combustion of solids: for instance, the incineration of waste materials (Saxena and Jotshi (1994)) and the combustion of low-grade coal (Basu (1999)). Besides, fluidized bed reactors are also popularly used for reaction purposes and can be generally categorized upon the reaction mechanisms, distinguishing between:

Inorganic Reaction Mechanisms

- Calcination of limestone (Tashimo et al. (1999));
- Reactions involving solids: e.g., chlorination of metal oxides (Morris and Jensen (1976)) and reduction of iron oxides (Srinivasan (2002)).

Organic Reaction Mechanisms

- Gas synthesis reactions catalyzed by solids: e.g., Fischer–Tropsch synthesis (Schulz (1999));
- Carbonization and gasification of coal (Stone et al. (1954), Wagner et al. (2008));
- Cracking reactions of hydrocarbons, e.g., fluid catalytic cracking of petroleum (Murphree et al. (1943)) and fluid/flexi coking of heavy feeds (Furimsky (2000)).

Processes that implement different physical operations are another major area for the application of fluidized bed systems in reality, for example, adsorption (Mckay (1988)), heat exchanging (Pronk (2006)) and, especially, the drying and formulation of particulate solids, which are the relevant research fields of this work.

According to the intensity and characteristics of gas-solid flow in the process chamber, the fluidized beds used for solids drying and formulation processes

can be divided into two types, conventional fluidized beds and spouted fluidized beds (Tsotsas et al. (2008)). The conventional fluidized bed usually has a uniform flow regime of fluidization in the entire process chamber, whereas multiple flow regimes appear simultaneously in different regions of the spouted fluidized bed.

The fluidized beds can also be distinguished into batch (discontinuous) fluidized beds and continuous fluidized beds, based on different operation modes. In a batch fluidized bed (Fig. 1.4(a)), the processing times of individual particles are identical, and thus the fluidized bed of this type is most suitable when an accurate control of the processing time is expected. In literature, the drying and formulation of particulate solids in batch-type fluidized beds have been widely investigated, e.g., Burgschweiger et al. (1999), Fyhr and Kemp (1999), Hede et al. (2009), Srinivas and Setty (2013) and Rieck et al. (2015). Nevertheless, a common disadvantage of batch processes is the relatively low throughput. This shortcoming can be removed in a continuous fluidized bed, since the solids are continuously fed in and discharged from the process chamber. Continuous processes can be broadly divided into two groups: single-stage processes and multi-stage processes. Figure 1.4(b) depicts a continuous fluidized bed in single-stage operation. In a single-stage fluidized bed, the incoming and contained solids will be immediately well mixed in the bed, which leads to a large proportion of solids that only stay in the apparatus for a short period while some solids may theoretically stay forever. Thus, the single-stage continuous fluidized bed can also be named as perfectly mixed fluidized bed, and such a difference in residence time between different solids is named residence time distribution (RTD). In order to narrow down the RTD of solids in continuous mode, the multi-stage continuous fluidized beds have been developed on the basis of the tank-in-series (TIS) model (MacMullin and Weber (1935)), which will be further introduced in Section 2.2. Figure 1.4(c) sketches a common type of multi-stage continuous fluidized bed, the horizontal fluidized bed, which is in the focus of all parts of this study. The horizontal fluidized bed usually has a long narrow cuboid processing channel, and the solids are moving continuously in the horizontal direction. Because of the large volume of the processing chamber and the continuous operation mode, this fluidized bed can achieve a higher yield when compared with the other types of fluidized bed systems. Hence, the horizontal fluidized bed is also often applied for drying and formulation of particulate solids.

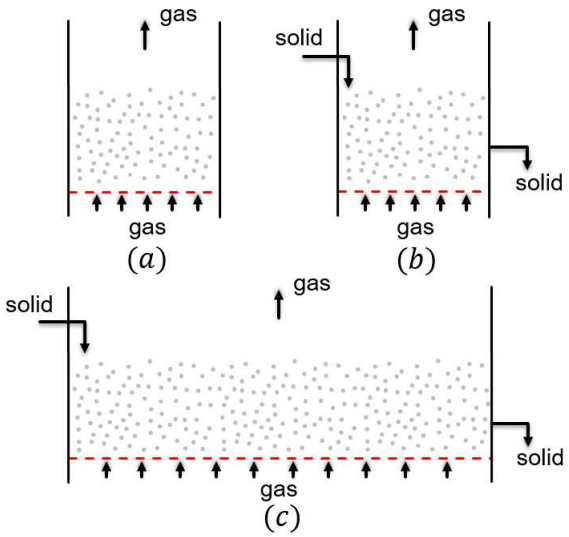

Figure 1.4: Schematic diagrams of three different fluidized beds: (a) discontinuous fluidized bed; (b) single-stage continuous fluidized bed; (c) horizontal fluidized bed.

1.2.4 Particle drying in the fluidized bed

The process of drying of particles, no matter whether they are raw materials, intermediate or final products, is ubiquitous and important in industrial production. Generally, drying is the separation process of removing liquid from wet solid material through the supply of heat, and the drying rate $\dot{m}$ is accordingly defined as the mass flow rate of the leaving liquid per unit area of the solid. Moreover, for a single particle, another drying term named normalized drying rate $\dot{\nu}$, which was firstly introduced by van Meel (1958), is closely related to the drying kinetics of a specific material.

The commonly used drying techniques can be divided into contact drying and convection drying on the basis of how the heat is transferred to the solid (Tsotsas et al. (2010)). According to the operation principle, the fluidized bed system is one type of convection dryer. In practice, the convective drying process can be divided into three periods: first, second, and third drying period. However, as depicted by Tsotsas et al. (2010), due to the fact that the transition from the second to the third drying period is usually not so obvious, many researchers have the second and the third drying periods merged together and only made a distinction between the first and the second drying period. The boundary particle moisture content between the first and second drying period is defined as critical particle moisture content $X_{p,cr}$, and the minimum moisture content

that a particle can reach is denoted by hygroscopic equilibrium particle moisture content $X_{p,eq}$. The relationship between the moisture content of particle and the drying rate can be plotted as a drying curve, which is obtainable through experiment. Léonard et al. (2008), Peglow et al. (2008b) and Stenström et al. (2008) respectively introduced different experimental methods for determining the drying curve.

As aforementioned, both the batch and the continuous fluidized bed are quite suitable for drying, because of the strong mixing and because intense heat and mass exchange between gas and solid phases can be achieved. The process of drying in a fluidized bed is influenced, on the one hand, by the characteristics of the solid material. Solids can be generally divided into two types with respect to different internal structures: non-porous and porous. The drying rate is always constant when the solid is non-porous (e.g., glass beads), and thus, one can also say, non-porous material only has the first drying period. However, for most solids with porous structure (especially with capillary porous structure) such as alumina particles, by definition, the mass transfer is gas side controlled and the normalized drying rate $\dot{\nu}$ is also equal to unity in the first drying period. In the second drying period, additional mass transfer resistances appear because, for instance, diffusion arises in the material, which leads to the normalized drying rate $\dot{\nu}$ being smaller than unity. A further description of the drying kinetics of the single particle in fluidized bed can be found in Chapter 3. On the other hand, the fluidized bed drying is also influenced by the condition of the process gas (e.g., the pressure, humidity, and temperature of the gas). This can influence many essential dimensionless numbers like the Sherwood number of particles and the Reynolds number, which are directly related to the driving force for mass transfer between gas and solids. According to different Reynolds number of particles, the Sherwood number of the single particle would differ from the corresponding value of the fluidized bed, especially when the Reynolds number is getting smaller (Kunii and Levenspiel (1991)). Nevertheless, these two quantities could properly be related (Schlünder and Tsotsas (1988), Kerkhof (1994) and Tsotsas (1994)). Gnielinski (1980) derived the Sherwood number of high Reynolds number fluidized beds based on the Sherwood number of a single particle. Later, based on the work of Gnielinski (1980), Groenewold and Tsotsas (1997, 1999) developed and validated an equation, which can accurately estimate the Sherwood numbers of both high and low Reynolds number fluidized beds.

1.2.5 Wet formulation of particles in fluidized beds

Another important application of fluidized bed system, in which drying also plays an important role, is the wet formulation of the particulate solids. This type of fluidized bed system, which can also be named as spray fluidized bed since the solution is sprayed as droplets onto a bed of primary particles during the operation, has been frequently applied for coating, granulation, and agglomeration of particles in industry (Peglow et al. (2008a)). The essential principles of these particle formation processes are schematically presented in Fig. 1.5 and specified as follows:

(a) The processes of coating and granulation both can generally be described as a particle layering process. Accordingly, the principles of spray fluidized bed **coating and granulation** (Fig. 1.5(a)) can be explained together: firstly, the solution is atomized as small droplets, which would contribute to creating a uniform liquid layer on the surface of the core particle; later, a solid shell is formed after the drying of the liquid layer, and the particle can then be considered as having being coated or granulated.

(b) In spray fluidized bed **agglomeration** (Fig. 1.5(b)), a binder material is usually added into the sprayed solution, and the binder droplets are sprayed onto the surface of primary particles through an atomizer. The collision between two primary particles may build a liquid bridge, which is quite viscous and would be dried and solidified as a real bridge between the collided particles. Afterward, the connected particles will get wet again and go on colliding with the other primary or newly formed particles. In the end, an agglomerate is created by the repetition of the processes mentioned above.

Although the principle of coating is basically the same as the principle of granulation, there are still some differences between them since they are applied for alternative purposes. Coating is often used for varying the surface function of specific material, achieving the protection of core particles from physical or chemical influence, delaying and/or controlling the release rate of the core particle, improving the appearance, taste, and odor of the final coated product, etc. (Saleh and Guigon (2007)). Coating can also be applied to increase the size of particulate material, which is the primary goal of granulation. Nevertheless, a clear distinction between coating and granulation process can be drawn,

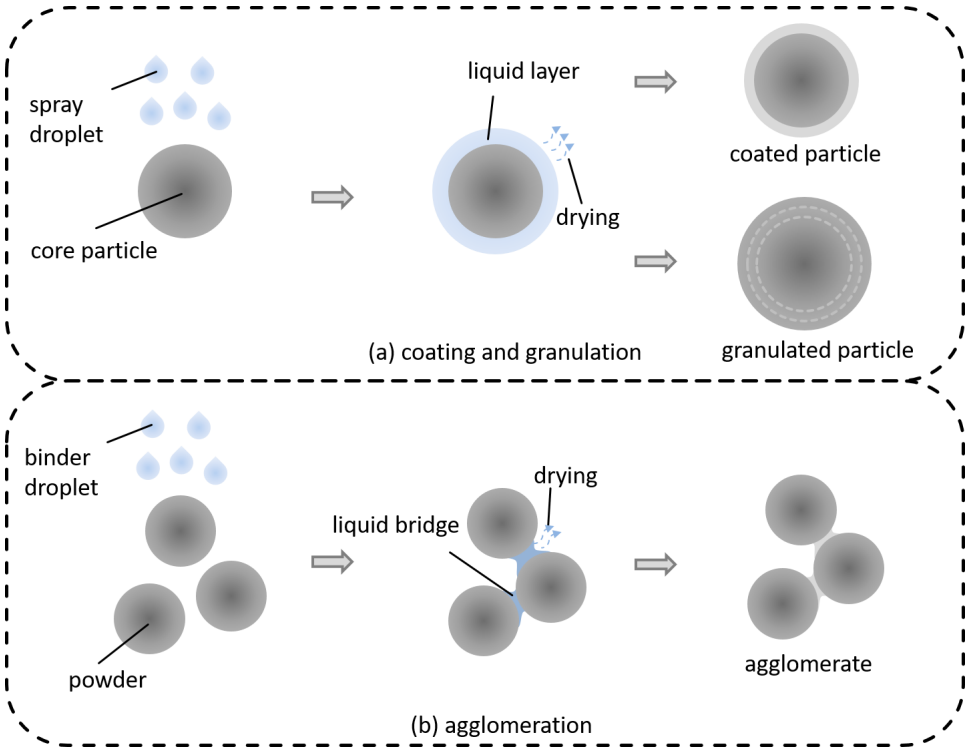

Figure 1.5: The principles of different types of spray fluidized bed processes: (a) coating and granulation; (b) agglomeration.

primarily, which is that the material used for coating is different from the core particle, whereas the shell material is the same as the core particle in granulation. The difference is much more apparent when comparing the agglomeration with coating/granulation. Unlike the layering process on every single primary particle in coating/granulation, agglomeration is a process of aggregation of primary particles and forming of secondary particles. Agglomeration is commonly used for increasing the performance of the original powders. For instance, the flowability and solubility of products such as instant coffee powder can be enhanced through agglomeration. Food products in the form of tablets are also agglomerates, which can improve the product appearance and make it easy to be recognized after agglomeration (Palzer (2007)).

In practice, however, the simultaneous occurrence of coating/granulation and agglomeration in a spray fluidized bed is usually unwanted. From a microscopic point of view, the existence or not of a liquid bridge after a collision between two particles (at least one should be wet) will first affect the type of final product. Ennis et al. (1991) applied a critical viscous Stokes number, which was firstly derived by Barnocky and Davis (1988), to classify the different

results after the collision between particles during the wet formulation process. According to their work, when the viscous Stokes number of particles is higher than the critical Stokes number, the two particles will rebound after colliding, which is preferred during the coating/granulation process. On the contrary, a coalescence of particles will most probably happen when the particles' Stokes number is smaller than the critical value. However, even though the particles have successfully coalesced, it does not mean that they have been successfully agglomerated. Because the stability of the coalesced particles depends both on the internal adhesion forces (e.g., the viscous force and the capillary force of the liquid bridge as well as the van der Waals forces between particles), and on other factors such as the strength of solid bridge after the liquid bridge has been dried. These factors are all highly influenced by the properties of the materials and the operating parameters. An overview of these factors was given in great detail by Peglow et al. (2008a).

It should also be noted that several unwanted side-effects may also happen during the wet formulation process. The reasons causing these side-processes can generally be explained based on the following two mechanisms:

(a) Collisions between droplets and particles: Uhlemann (1990) discussed the relationship between droplets and particles during the wet formulation process, and defined a series of side-processes that lead to the formation of new particles. Figure 1.6 shows several mechanisms of forming new small particles in a spray fluidized bed. As can be observed, new fine particles can be formed when the droplets are not reaching or are already dried before reaching the surface of the particle, or the particle surface is too wet to let the droplets coalesce.

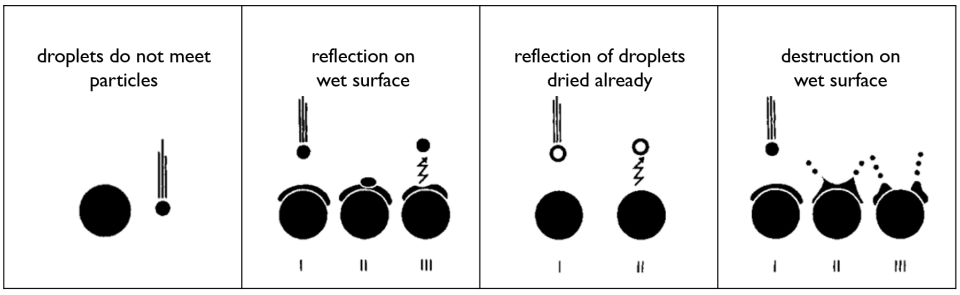

Figure 1.6: The mechanisms forming new small particles (fines) in the fluidized bed (Uhlemann (1990)).

(b) Hydrodynamic movement of particles: The breakage (attrition and fragmentation) of particles is another common side-process. For non-reactive processes operated under isothermal conditions, it is purely caused by particle-particle and particle-apparatus collisions, as has been proposed by Shamlou et al. (1990).

1.3 Scope of the work

So far, fundamental information needed for understanding the forthcoming research subjects has been offered. In order to draw an overall picture of the present work, the outline of the dissertation will be described in the rest of this chapter. This dissertation consists of five chapters. The main contents are presented in Chapters 2 to 4, and all the research topics are developed around a keyword: horizontal fluidized bed. The residence time distribution, drying and wet formulation of particles are respectively investigated in these chapters. These topics are seemingly interrelated, however, for an in-depth study of each, they need to be investigated and discussed separately. Hence, literature review and identification of research gaps as well as the motivation behind each particular topic are allocated into every major chapter.

Chapter 2 is dedicated to thoroughly investigating the research methodology of RTD of particles in the horizontal fluidized bed. Several basic concepts and properties regarding the RTD research are firstly explained. Besides, the apparatus and the material, which are used not only for RTD studies but also for the drying and particle formulation studies of the present work, are introduced in this section as well. Then, sets of data from RTD experiments are post-processed and analyzed using various numerical models. Subsequently, the theoretical tank number and the dispersion coefficient are obtained, and some further discussions around these two properties are provided. In the next section of this chapter, two alternative Eulerian methods are applied for simulating the RTD of particles employing computational fluid dynamics (CFD) tools. Accordingly, the validity of the simulation results, as well as the possibility of accelerating the simulation are discussed.

In Chapter 3, a variety of horizontal fluidized bed dryer models are presented. In total five models, i.e., the plug flow (PF) model, the continuous flow stirred-tank reactor (CSTR) model, the tank-in-series mixed flow (TISMF) model, the one-dimensional population balance drying (1D-PBD) model, and the

two-dimensional population balance (2D-PBD) model, are developed. The comprehensive descriptions of these models are offered appropriately. Later, simulation results from different models are validated and discussed based on previous experimental works. The mean moisture content and the standard deviation of moisture content distribution (MCD) are selected as the research criteria here. Moreover, some model-based parameter studies can be found in this chapter as well.

Chapter 4 is dealing with the numerical modeling of a major branch of particle growth processes, the coating process, in the horizontal fluidized bed. According to a review of the previous works in literature, two population balance coating models (i.e., 1D-PBC and 2D-PBC models) of the horizontal fluidized bed are developed. Specifically, the RTD of particles is selected as an important property coordinate in both models, and it is generated by using a series of empirical equations. The simulated mean diameter and the standard deviation of the particle size distribution (PSD) are then verified with reference data from our group. A comparison between the two models is carried out as well, and furthermore, the ability of the 2D model is exhibited by conducting sequences of numerical tests.

Lastly, based on the conclusions from each major chapter, an overall view of all the results and an outlook are provided in Chapter 5

Chapter 2

Particle Residence Time Distribution in Horizontal Fluidized Bed

This chapter has been partly taken from: Chen, K., Bachmann, P., Bück, A., Jacob, M., and Tsotsas, E. (2019). CFD simulation of particle residence time distribution in industrial scale horizontal fluidized bed. Powder Technology, 345:129–139.

2.1 Overview

For any continuous process, a main emphasis of research is on the residence time distribution (RTD) of processed materials in the apparatus. The continuous horizontal fluidized bed, as introduced in Chapter 1, is frequently used for drying and particle formulation in industry. In these processes, the material is usually time-sensitive and a broad spread of residence time should be prevented. Therefore, a comprehensive understanding of RTD of particulate solids in the horizontal fluidized bed is a helpful knowledge base for the further investigation of drying and coating processes.

This chapter is concerned with the RTD of solids in a commonly used industrial-scale horizontal fluidized bed. After completing this chapter, the following topics will have been investigated and discussed:

- A brief introduction of several basic properties regarding RTD research (Section 2.2).
- Systematic investigation of the RTD of solids in the horizontal fluidized

bed by experiment and mathematical models (Section 2.3).

- Use of computational fluid dynamics (CFD) tools to simulate the RTD of solids in the horizontal fluidized bed (Section 2.4).

2.2 Fundamentals and theories for RTD research

In this section, several basic concepts and properties regarding RTD study are firstly illustrated.

2.2.1 Plug flow, mixed flow, and back-mixing flow

As stated by Levenspiel (1999), theoretically, the ideal flow pattern of the granules without any mixing effect (no overtaking or back-mixing) in a horizontal fluidized bed should be plug flow, which means the residence time of each processed granule in the processing chamber should be identical. Levenspiel (1999) also introduced another ideal flow pattern: the mixed flow (also named ideal CSTR), which means the newly entered granules will instantaneously and completely mix with the "old" granules in a mixed flow fluidized bed. The assumptions of the plug flow and the mixed flow fluidized bed are widely used for mathematical simulations of the horizontal fluidized bed dryer, and these will be discussed in details in Chapter 3.

In the real process, however, the convection of particles (forward directed) is disturbed by the dispersion of particles (forward and backward directed), so that the ideal solid flow patterns cannot be achieved and a distribution of residence time among the solids occurs. Here, we name this type of horizontal fluidized bed device: back-mixing flow fluidized bed.

2.2.2 RTD measurement methodology

For back-mixing flow fluidized bed, the RTD is directly related to the performance of the equipment because it can directly give information about the intensity of solids mixing, segregation, and transportation. Thus, the RTD of a horizontal fluidized bed should be fully investigated, and by means of tracer, adequate tracing methods can be applied for measuring the RTD. Tracers are non-reactive materials, the physical properties of which are identical or close to the properties of the processed solids. They are widely used for RTD studies. Usually, for obtaining the RTD of particles in the fluidized bed, the

tracer is introduced into the apparatus at the inlet when a steady state of the solids flow (i.e., the mass flow rate at the outlet equals the feed rate) has been established in the process chamber, and the concentration-time curve of the tracer is simultaneously monitored at the outlet.

The pulse and stepwise input (Levenspiel (2012)) of tracer are the two most common techniques for RTD measurement. In the pulse test, as the name implies, a small amount of tracer, which will not influence the regular solid flow, is instantaneously introduced into the entering flow like a pulse. And, for the step test, the material is wholly switched from the original solids to tracer at the inlet. Accordingly, the measured RTD curves (concentration curves) are named as the C_{pulse} curve and the C_{step} curve. For more straightforward interpretation, the respective curves are often converted into the E-curve and the F-curve after normalization. These normalized RTDs are related to each other and interconvertible by using the following equations:

$$F(t) = \int_0^t E(t)dt, \tag{2.1}$$

and

$$E(t) = \frac{dF(t)}{dt}. \tag{2.2}$$

2.2.3 The mean and variance

The mean τ and variance σ^2 are the two most commonly used properties for describing the RTD curve, where the mean can tell the average time that particles stay in the fluidized bed, and the variance measures the spread of the curve in time.

From a C_{pulse} curve, the mean and variance can be calculated with the following equations:

$$\tau = \frac{\int_0^\infty tC_{pulse}\,(t)\,\mathrm{d}t}{\int_0^\infty C_{pulse}\,(t)\,\mathrm{d}t}, \tag{2.3}$$

$$\sigma^2 = \frac{\int_0^\infty t^2C_{pulse}\,(t)\,\mathrm{d}t}{\int_0^\infty C_{pulse}\,(t)\,\mathrm{d}t} - \tau^2. \tag{2.4}$$

Similarly, from a C_{step} curve, the mean and variance can also be calculated as:

$$\tau = \frac{\int_0^\infty \left(C_{step,max} - C_{step}\,(t)\right)\mathrm{d}t}{C_{step,max}}, \tag{2.5}$$

$$\sigma^2 = \frac{2\int_0^\infty t\left(C_{step,max} - C_{step}\left(t\right)\right)\mathrm{d}t}{C_{step,max}} - \tau^2. \tag{2.6}$$

2.2.4 The theoretical tank number and TIS model

Based on the mean and variance of the corresponding RTD curve, another important quantity, the theoretical tank number, K, can be calculated with:

$$K = \frac{\tau^2}{\sigma^2}. \tag{2.7}$$

This tank number arises from the tank-in-series (TIS) model (MacMullin and Weber (1935)), which describes the continuous reactor as a serial connection of several identically-sized perfectly-mixed reactors. The number of the theoretical tanks can represent the back-mixing effect of solids in the process chamber: for instance, the fluidized bed will be a plug flow reactor when the tank number is infinity, and the fluidized bed will be an ideal CSTR when the tank number is one. Moreover, based on the particle mean residence time and theoretical tank number, the normalized RTD can be expressed with the following equation:

$$E(t) = \frac{1}{\tau}\left(\frac{t}{\tau}\right)^{K-1}\frac{K^K}{(K-1)!}e^{-tK/\tau}. \tag{2.8}$$

2.2.5 The dispersion coefficient and diffusion coefficient

For a fluidized bed system, the dispersion coefficient of particles, D, is a value which can reflect the overall effect that the intensity of random particle motion has in comparison to particle convection. If the dispersion coefficient is high, the dispersion of solids is more prominent, and this leads to a broad spread of the RTD curve. The diffusion coefficient of particles, also named particle diffusivity, which sounds similar to the dispersion coefficient, is a property that describes particle mobility at the microscale. Multiplied with the gradient of mass concentration of particles it results in total particle flow rates.

An early and illustrative distinction has been made between these two properties by Taylor (1953), who derived the dispersion coefficient for a long cylindrical tube with laminar fluid flow in it. In Taylor's work, the diffusion coefficient of the molecules in the fluid is unambiguously known in advance. The dispersion coefficient is obtained by adding a term, which results from apparatus geometry

(tube diameter) and the flow field (laminar), to the molecular diffusivity, and the result indicates that the dispersion coefficient can be much larger than the diffusion coefficient.

In general, the dispersion coefficient does not have to be equal to particle diffusivity. A detailed investigation of these two properties will be conducted in Section 2.4.4.3.

2.2.6 The dispersion model

As suggested by Smolders and Baeyens (2000) and Grasa and Abanades (2002), the dispersion coefficient is attainable by fitting the analytical solution of an empirical model, the dispersion model, to the experimental RTD data. This one-dimensional model can also be used to describe particle convection and dispersion in the longitudinal direction of the horizontal fluidized bed:

$$\frac{\partial E(t)}{\partial t} = D\frac{\partial^2 E(t)}{\partial z^2} - u_b\frac{\partial E(t)}{\partial z}. \tag{2.9}$$

Here, D is the longitudinal effective dispersion coefficient and u_b is bed velocity. Since u_b describes the velocity of particle movement along the main direction of flow (denoted by convection or advection), it is by definition equal to the ratio of bed length L_b to the mean residence time τ of the particles:

$$u_b = \frac{L_b}{\tau}. \tag{2.10}$$

2.2.7 The Bodenstein number

The dimensionless form of the dispersion coefficient is named as the reactor Peclet number, Pe_r, by many researchers, e.g., Smolders and Baeyens (2000), Fogler (2006), Adeosun and Lawal (2009), and Liu et al. (2012). However, in this work this dimensionless dispersion group is called the Bodenstein number, Bo, which is more popularly used in Europe.

The Bodenstein number is defined as the ratio of solid convection to dispersion from the inlet to outlet of the fluidized bed, which can be expressed as:

$$Bo = \frac{u_b L_b}{D}, \tag{2.11}$$

where u_b is the bed velocity, and L_b represents the characteristic length of the process chamber. Like the theoretical tank number, the Bodenstein number

can also represent the degree of solids back-mixing in the fluidized bed:

- $Bo = 0$, represents the fully back-mixed condition, when the corresponding solids flow is mixed flow.
- $Bo \to \infty$, represents the absence of any back-mixing effect; then, the corresponding solids flow is plug flow.

2.3 RTD experiments

2.3.1 Previous work

It is known that an RTD of particles will always exist in a continuously operated fluidized bed, and it can be influenced by several factors, e.g., the geometry of the process chamber, the superficial gas velocity, the properties of processed material and so on. Usually, experiment is the most direct way to investigate the performance of existing equipment. By conducting RTD experiments, several vital characteristics, like the mean and variance of RTD, can be obtained and empirical correlations may also be developed. Therefore, several researchers have experimentally investigated the RTD of particles in horizontal fluidized beds in the past few decades.

Reay (1978) investigated the RTD of copper and sand in a horizontal fluidized bed. In this work, the bed width, the bed length and the outlet weir height of the process chamber could be altered. The results show that the dispersion coefficient tends to increase with increasing gas velocity and it decreases with increasing particle density or particle size. The solids dispersion coefficient of a shallow bed seems to be independent of bed length and is an order of magnitude lower than that of a deeper bed. In the end, a correlation for the dispersion coefficient was derived based on the minimum fluidization velocity and superficial gas velocity by Reay (1978).

In the work of Satija and Zucker (1986), a series of RTD experiments were conducted by using a vibro-fluidized bed. Although the granules in this work were generally fluidized by vibration, nevertheless, the influence of internal baffles was firstly analyzed. It was founded that, when the vibration amplitude is high, the mean residence time increases by decreasing the space between internal baffles. However, the results also indicate that the dispersion coefficient of the particles decreases significantly by increasing the number of internal baffles.

The effect of bed velocity, bed height, superficial gas velocity and gas temperature on the dispersion coefficient was studied by Nilsson and Wimmerstedt (1988). Quartz sand and granulated apatite were the test materials in their research. The results show that the dispersion coefficient increases with increasing bed velocity or bed height. Furthermore, the dispersion coefficient increases linearly with the superficial gas velocity, which can be influenced by the gas temperature. Generally, the results of Reay (1978) were significantly supplemented by Nilsson and Wimmerstedt (1988), who also developed a new correlation for the dispersion coefficient involving the above-mentioned parameters.

Bachmann et al. (2016) also studied systematically the influence of a set of process parameters (for example, length and width of the fluidized bed, superficial gas velocity, outlet weir height, etc.) on the residence time behavior of particles in two horizontal fluidized beds of different sizes. It was stated that decreasing the height of the outlet weir or increasing the length-width ratio of the fluidized bed could increase the Bodenstein number. The Bodenstein number also increases with increasing particle size or feed rate, whereas it decreases by increasing superficial gas velocity. Besides, it has been pointed out that the correlations from Reay (1978) and Nilsson and Wimmerstedt (1988) are of questionable validity for other than the original experimental data. Therefore, a new correlation, which fits well with their own experimental data as well as the data from Reay (1978) and Nilsson and Wimmerstedt (1988), was derived by Bachmann et al. (2016) for predicting the Bodenstein number.

Later, the effect of internal baffles was investigated by Bachmann et al. (2017) as well. They found that for internal baffles in underflow configuration (i.e., internal baffles are installed over the air distributor and particles can only pass through as an underflow) the Bodenstein number increases with increasing the number of internal baffles or decreasing the gap height. In the end, two empirical equations for horizontal fluidized beds with different internal baffle configurations (underflow and overflow) were developed based on the correlation for horizontal fluidized beds without baffles from their previous work (Bachmann et al. (2016)).

In conclusion, the experimental investigation of horizontal fluidized beds from Bachmann et al. (2016, 2017) seems to offer the latest and most comprehensive results, and consequently, their methodology of studying RTD is also applied to this work.

2.3.2 Apparatus

A pilot scale horizontal fluidized bed (Glatt GF/Procell 20), which is often applied for industrial production, was used in the present work. The process chamber is of cuboid shape, with a height of 0.4 m and a rectangular cross section of 1.0 $\times$ 0.2 m^2. The schematic diagram of particle movement within this plant is shown in Fig. 2.1. As can be seen, three internal baffles were installed over the air distributor (underflow configuration) and divided the fluidized bed into four compartments of equal size. These internal baffles are removable, for testing their effect. An outlet weir, the height of which could be varied to control the bed mass, was installed at the end of the apparatus. The process air (evenly distributed by an air distributor with an open area of 19.63%) and particles are moving in cross-flow in the process chamber.

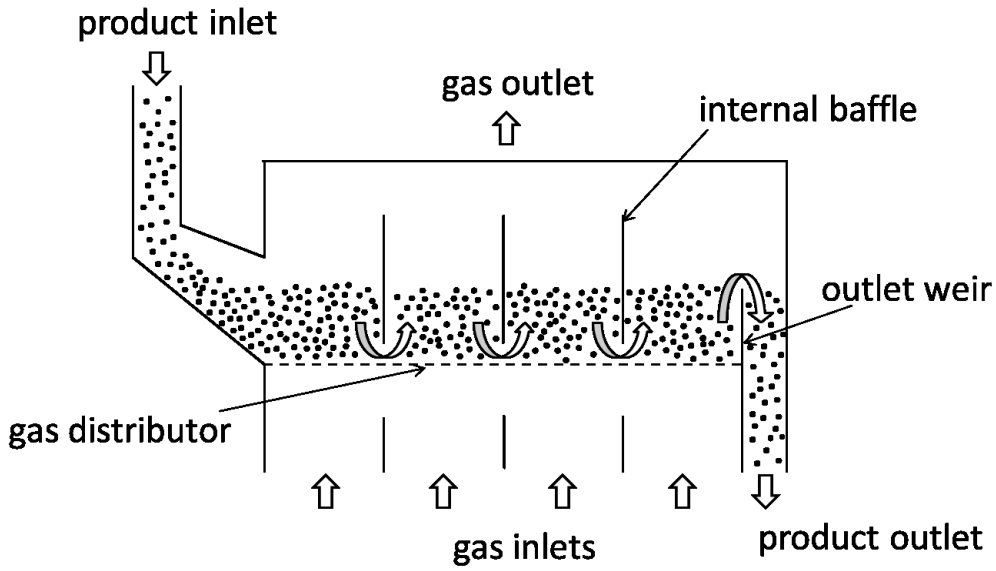

Figure 2.1: Scheme of the experimental plant used in this study.

In short, Glatt GF/Procell 20 is commonly used for granule drying and coating processes, which will be specified later, in Chapter 3 and Chapter 4, respectively.

2.3.3 Material

In this work, aγ-Al_2O_3 particles with a diameter of 1.8 mm (Sasol GmbH), which belong to Geldart classification group D (Geldart (1973)), have been used for RTD measurement. These particles are nearly spherical and mono-sized.

Moreover, they have several desirable properties for RTD study, like smooth surface, hardness, durability, ease of dosing, etc.. The specific physical and hydrodynamic properties of this material are listed in Table 2.1. The material composition is provided by Sasol GmbH. The mean diameter and the sphericity were measured by means of Camsizer (Retsch GmbH, Germany), which in principle evaluates the projections (shadows) of illuminated falling particles. The material density is provided by Sasol GmbH, and the density of the porous particles was taken from Burgschweiger et al. (1999). Accordingly, the porosity of particles can be calculated with: $\psi_p = 1 - (\rho_p/\rho_{mat})$.

Table 2.1: Physical and hydrodynamic characteristics of the experimental material.

Property	Value	Unit
Chemical composition	97.9% γ-Al_2O_3	-
Average diameter	1.80	mm
Sphericity	0.97	-
Material density	3372	kgm^{-3}
Particle density	1040	kgm^{-3}
Particle porosity	69.2	%
Minimum fluidization velocity	0.54	ms^{-1}

2.3.4 RTD experiment series

In total eight RTD experiments were conducted to test the effect of superficial gas velocity, internal baffles, and outlet weir. The corresponding process parameters are listed in Table 2.2.

In each experiment, the γ-Al_2O_3 particles were fed continuously into the process chamber with a fixed mass flow rate of 1 kg/min. When a steady state of particle flow had been established, 0.5 kg of tracer (dyed γ-Al_2O_3 particles) was added to the fluidized bed by means of the aforementioned pulse input method. At the same time, samples were collected every minute at the outlet with a five seconds sampling time. In the end, the number of colored particles in each sample was counted, and thus the mass fraction of tracer in each Sample (C_i) could be calculated.

Consequently, by conducting these pulse stimulus-response experiments, discrete RTD data could be obtained. Accordingly, the mean residence time and variance of the curves can also be calculated with the discretized form of

Table 2.2: Summary of parameters of the RTD experiments.

Exp. No. [−]	Gas velocity [ms^{-1}]	Baffle gap size [mm]	Feed rate of particles [kgmin^{-1}]	Outlet weir height [mm]	Number of internal baffles [−]
1	1.36	-	1	35	0
2	1.36	6	1	35	3
3	1.26	6	1	35	3
4	0.91	6	1	35	3
5	1.70	-	1	95	0
6	1.70	6	1	95	3
7	1.36	6	1	95	3
8	1.11	6	1	95	3

Eqs. 2.3 and 2.4, respectively:

$$\tau \cong \frac{\sum_i t_i C_i \Delta t_i}{\sum_i C_i \Delta t_i}, \tag{2.12}$$

$$\sigma^2 \cong \frac{\sum_i t_i^2 C_i \Delta t_i}{\sum_i C_i \Delta t_i} - \tau^2. \tag{2.13}$$

2.3.5 Experimental results

On the basis of the experimental data, the mean residence time and standard deviation (square root of the variance) were calculated according to Eqs. 2.12 and 2.13, and subsequently, the number of theoretical tanks was obtained with Eq. 2.7. The relevant calculation results are listed in Table 2.3.

Table 2.3: Summary of the post-processed parameters of the RTD experiments.

Exp. No. [−]	Mean residence time [s]	Standard deviation [s]	Number of theoretical tanks [−]
1	182.6	113.5	2.6
2	184.7	92.7	4.0
3	193.3	92.5	4.4
4	268.7	119.5	5.1
5	352.5	306.2	1.3
6	352.7	241.4	2.1
7	427.9	276.9	2.4
8	564.9	350.7	2.6

Some preliminary qualitative analysis of the influence of fluidized bed internal structure and operation conditions can then be carried out. By comparing experiments No. 1 and No. 2, as well as experiments No. 5 and No. 6, the results show that the internal baffles have not much influence on the mean residence time of particles. Nevertheless, the standard deviation decreases and the number of theoretical tanks increases by adding internal baffles. This indicates that the internal baffles can reduce the back-mixing effect in the horizontal fluidized bed, which agrees with the conclusion from Satija and Zucker (1986) and Bachmann et al. (2017). The results from experiments No. 2 and No. 7 show the influence of the outlet weir height when the other parameters are fixed. Both mean residence time and standard deviation increase with increasing the outlet weir height, which is in agreement with results report by Khanali et al. (2012). Accordingly, the theoretical tank number decreases after increasing the outlet weir height, which means the back-mixing effect of the particles is more intense when the outlet weir is higher. The influence of the superficial gas velocity was investigated (by comparing experiments No. 2, No. 3 and No. 4, along with experiments No. 6, No. 7 and No. 8) as well. It can be seen that the average time that particles stay in the process chamber decreases with increasing superficial gas velocity. Nevertheless, the dispersion effect of particles is also higher, while the standard deviation and the theoretical tank number both increase with increasing superficial gas velocity, which agrees with the conclusions from Reay (1978), Nilsson and Wimmerstedt (1988), and Bachmann et al. (2016).

2.3.6 Numerical results

2.3.6.1 TIS model

The TIS model, which has been presented in Section 2.2.4, was validated by the measured RTD data. Figure 2.2 shows that the numerical results from the TIS model are in relatively good agreement with the corresponding experimental data for variant operation parameters. Moreover, it is clear that the simulated curves of fluidized beds with lower outlet weir (35 mm) have a higher consistency.

One thing to note here is that, as presented in Table 2.3, usually the experimentally obtained number of theoretical tanks is a non-integer and it should be rounded to the nearest integer for solving the factorial part in Eq. 2.8, as the

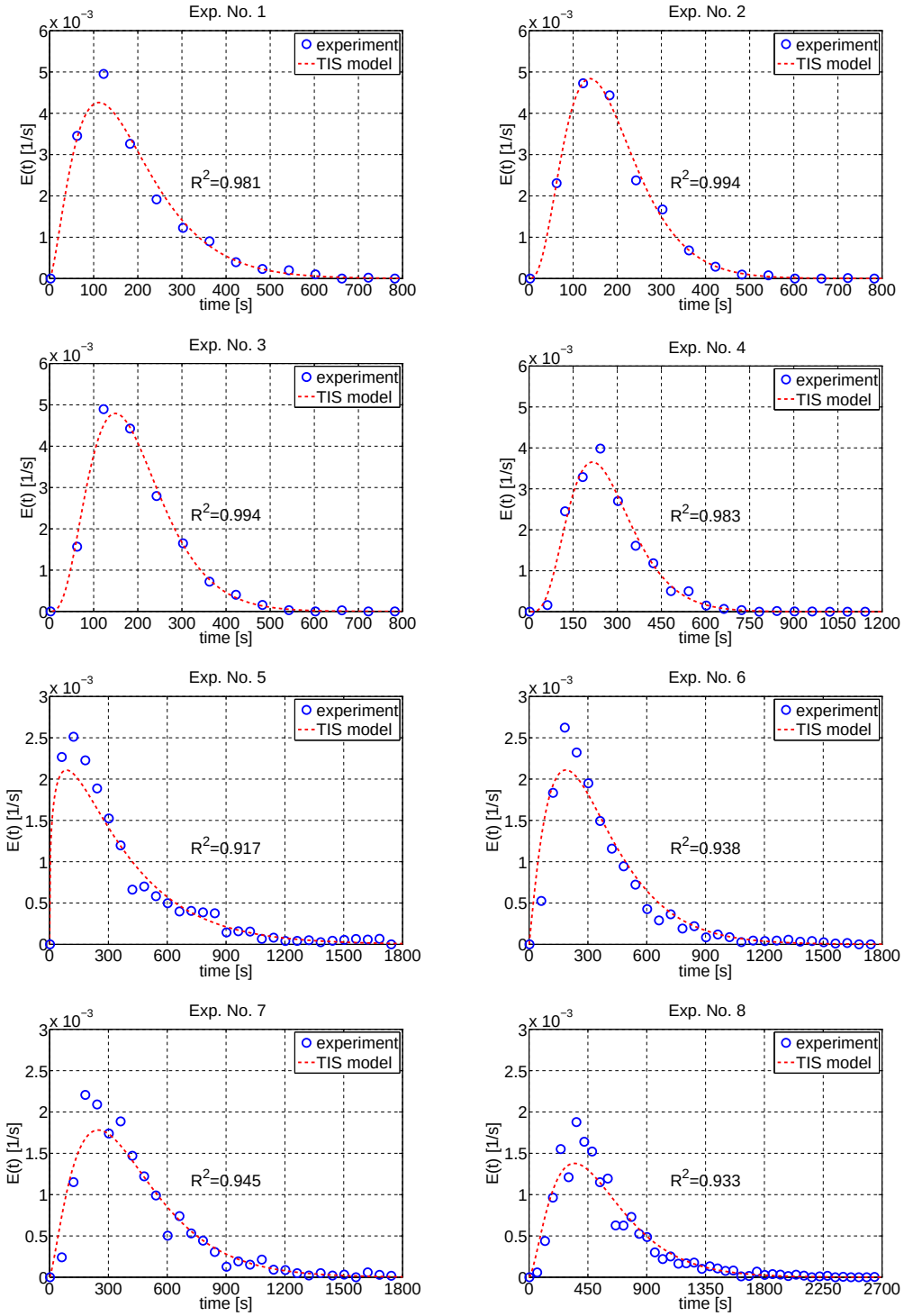

Figure 2.2: Comparison between numerical results from TIS model and the measured RTD data.

factorial only has meaning for non-negative integer numbers. Whereas, in this study, the factorial of the non-integer tank number was solved by the gamma function (see Cody (1976)), which is a smooth function for solving the factorial of positive non-integer numbers. The RTD curves obtained by using integer and non-integer tank numbers (K = 2, 2.5 and 3) at constant mean residence time (τ = 300 s) are shown in Fig. 2.3. It is obvious that when the tank number is 2.5, the corresponding curve lies between the curves calculated from rounded integer numbers. The effect of using non-integer number of theoretical tanks was further tested by comparing the coefficient of determination (R^2) of simulated curves and experimental data, and the calculation results are listed in Table 2.4.

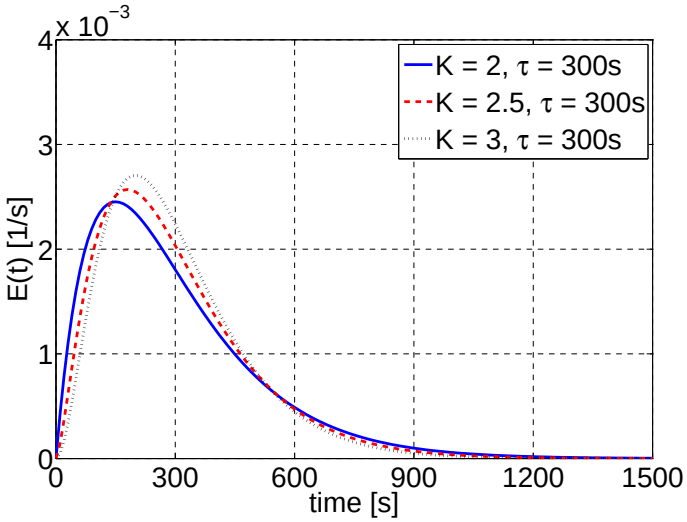

Figure 2.3: RTD curves obtained by using different numbers of theoretical tanks when the mean residence time is constant.

As can be seen, the R^2 values of curves simulated by using rounded integer tank numbers also indicate coarse agreement with the experimental data. However, in some cases, there is a significant disparity between the simulated curve and the measured data. On the other hand, the curves simulated by using the real tank number (non-integer) are always consistent with the measured data (the smallest R^2 value is 0.917), which is essential for RTD modeling research.

In general terms, the number of theoretical tanks is the critical parameter of the TIS model. Normally, one might expect that the number of geometrical tanks (e.g., the internal baffles divide the process chamber into four tanks

Table 2.4: Coefficients of determination calculated for comparing the similarity of RTD curves simulated by the TIS model using different tank numbers with experimental data.

Exp.	Coefficient of determination (R^2)		
No.	Actual tank number	Rounded down tank number	Rounded up tank number
1	0.981	0.965	0.974
2	0.994	0.969	0.994
3	0.994	0.989	0.991
4	0.983	0.983	0.976
5	0.917	0.439	0.871
6	0.938	0.922	0.958
7	0.945	0.908	0.950
8	0.933	0.868	0.946

in our RTD experiments) will equal to the calculated number of theoretical tanks. However, in most cases, these two properties are different and have no direct interrelation. Thus, the number of theoretical tanks cannot be estimated in a straightforward way from the internal structure of a horizontal fluidized bed, which shows that the TIS model is only seemingly simple and convenient. Additionally, the calculated tank numbers also show a certain degree of inaccuracy when the fluidized bed is equipped with a high outlet weir (experiments No. 5 - 8). In this case some inconsistency between the simulated curves and the experimental data can be observed in Fig. 2.2 and Table 2.4.

2.3.6.2 Dispersion model

Theoretically, the dispersion model can depict the particle movement in the axial direction of the horizontal fluidized bed system from a macroscopic perspective, and just as the number of theoretical tanks plays an important role in the TIS model, the dispersion coefficient is the core parameter of the dispersion model.

As aforementioned, one methodology to estimate the dispersion coefficient is to fit the analytical solution of the dispersion model to the experimental data. However, this can only be done when measured data exist. Otherwise, empirical correlations may be used to predict the dispersion coefficient in process simulations (for example, the empirical correlations from Reay (1978) and Nilsson and Wimmerstedt (1988) were respectively applied by Baker et al. (2006) and Wanjari et al. (2006) in their researches).

In this work, the dispersion coefficient has been estimated by means of the empirical correlations from Bachmann et al. (2016, 2017) (the details of the correlations will be specified later in Chapter 4). These correlations predict the Bodenstein number of differently structured horizontal fluidized beds for different operation parameters, from which the dispersion coefficient of each experiment can be obtained with the relationship according to Eq. 2.11.

The calculated empirical dispersion coefficients D are listed in Table 2.5. Then, the obtained mean residence times (Table 2.3) and dispersion coefficient were implemented to the dispersion model (Eq. 2.9), solved by using the solver ode15s in MATLAB software with finite volume method, and the results are plotted against the experimental data in Fig. 2.4.

Table 2.5: Dispersion coefficients, based on the empirical correlations and corrected to better fit the experiments.

Exp. No. [−]	D (empirical) $[m^2 s^{-1}]$	R^2 (vs. Exp.) [−]	D (corrected) $[m^2 s^{-1}]$	R^2 (vs. Exp.) [−]
1	0.00055	0.650	0.00141	0.997
2	0.00051	0.858	0.00080	0.975
3	0.00049	0.953	0.00075	0.995
4	0.00019	0.859	0.00047	0.974
5	0.00171	0.949	-	-
6	0.00103	0.986	-	-
7	0.00059	0.975	-	-
8	0.00034	0.955	-	-

It is evident that the simulated curves for the fluidized bed with 95 mm outlet weir height fit much better to the experimental data than the results for the fluidized bed with 35 mm outlet weir height. In consideration of the error that arises when the empirical correlations are used, the dispersion coefficients of experiments No. 1 - 4 (low outlet weir height) were corrected by trial and error on the basis of the presented experimental results. The simulated curves by using the corrected dispersion coefficients are plotted in Fig. 2.4 as well. As can be seen in the plots and the coefficients of determination R^2 between each corrected curve and the corresponding experimental data listed in Table 2.5, the simulated curves fit much closer to the experimental data after correction. Therefore, the corrected dispersion coefficients of experiments with 35 mm outlet weir height appear to be more precise than the dispersion coefficients

calculated from the empirical correlations. Nevertheless, the correlations from Bachmann et al. (2016, 2017) can well predict the dispersion coefficient when the outlet weir height is high (95 mm) and can also be used to coarsely estimate the dispersion coefficient when the outlet weir height is relatively low (35 mm).

Besides, it is found that the dispersion coefficient decreases by either decreasing gas velocity or adding internal baffles, which also illustrates that the dispersion of particles can be influenced by internal baffles and superficial gas velocity, as discussed in Section 2.3.5.

2.4 Computational fluid dynamics (CFD) simulations

Although experiment is the most direct way to investigate the performance of existing equipment, it becomes hardly feasible from the perspective of plant scale-up as well as plant design. To this purpose, simulations by computation fluid dynamics (CFD) would be highly desirable. Apart from being a powerful tool to study the flow characteristics of fluidized bed systems, CFD simulations can also give a more in-depth look into gas-solid flows and provide more information about the fluidized bed from a microscopic point of view, which is difficult to realize by experiment.

2.4.1 Previous RTD researches by CFD

Regarding continuous operation, one common method for RTD prediction by CFD is the so-called species method, which solves a species transport equation in the course of a numerical tracer experiment. Vedantam et al. (2006), Adeosun and Lawal (2009), Deshmukh et al. (2009), Kolhe et al. (2011), Liu et al. (2012) and Zhang et al. (2015) carried out either 2D or 3D RTD simulations of different materials in various equipment (e.g., Taylor-Couette contactor, T-junction microchannel, annular centrifugal extractor, pulsed sieve plate column, fluid catalytic cracking and cyclone reactor) using the species method. For fluidized bed systems, Khongprom et al. (2012) and Hua et al. (2014) also used the species method for obtaining the RTD in circulating fluidized beds. The obtained RTD curves show good agreement with experimental data, but to this purpose, the diffusion coefficient needs to be set correctly in advance for the tracers in all simulations. Moreover, the equation of species transport was solved only after the flow inside the apparatus had reached a steady state in these studies. In addition, no distinct tracer phase is introduced into the

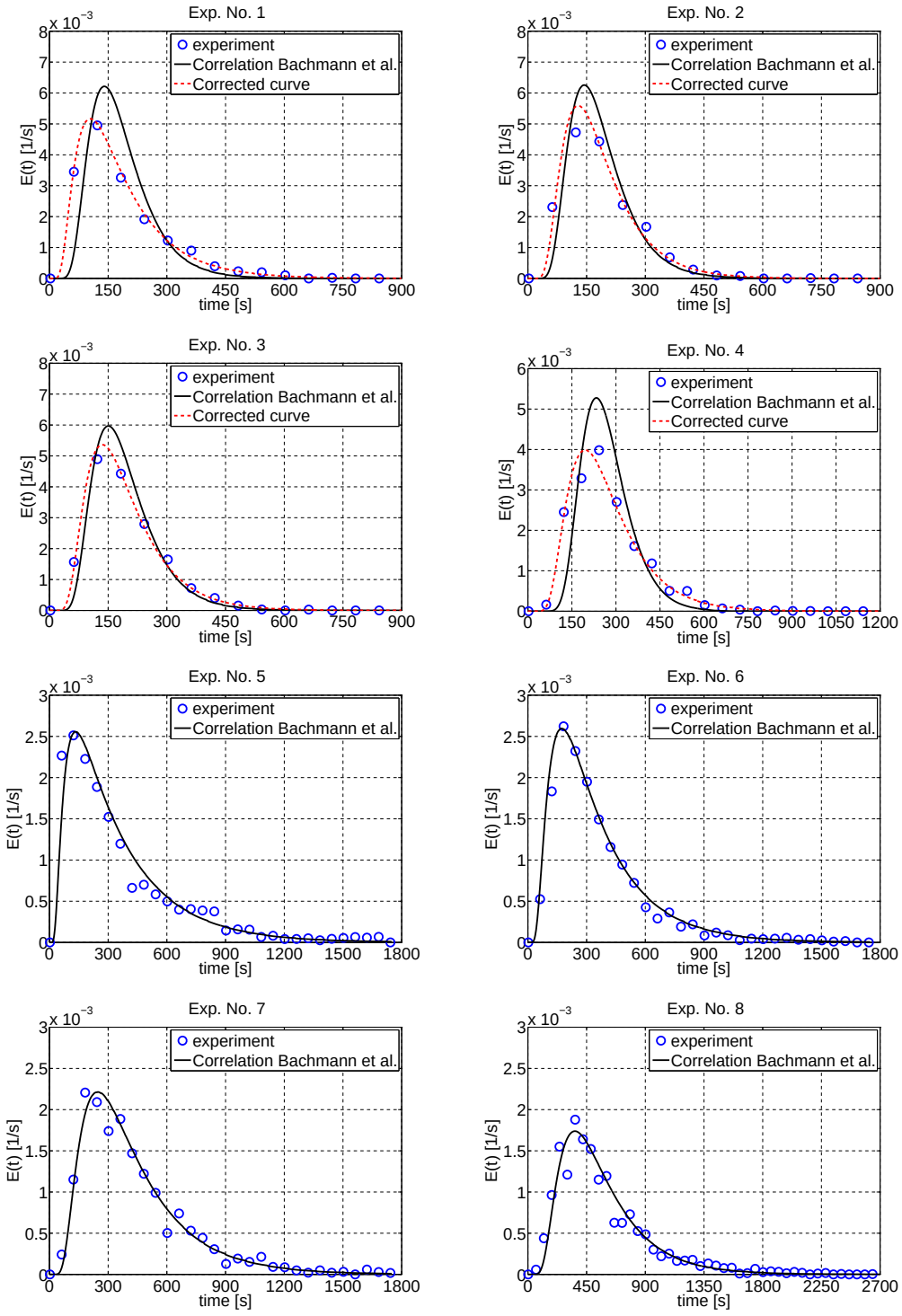

Figure 2.4: RTD results of the dispersion model computed by using empirical dispersion coefficients (Bachmann et al. (2016, 2017)) and corrected dispersion coefficients to better fit the experimental data.

flow by using the species method, and the simulation only has one single solid phase.

Therefore, it is necessary to investigate the feasibility of adding tracer particles into the solid flow in CFD simulations. The Eulerian-Lagrangian model, e.g., CFD-DEM, is the most direct way of doing so. Jiang et al. (2017) treated sprayed droplets as small particles and simulated the droplet deposition on large particles in a Wurster fluidized bed by using a CFD-DEM model. Besides, the particle RTD and particle collision velocities in the spray zone were also discussed. Particle RTDs in a 2D riser and downer were investigated by Zhao et al. (2010). However, the number of simulated particles was small and the simulated process time was very short in both studies. This illustrates that CFD-DEM is a valuable tool for understanding micro-scale processes, but, due to its high computational cost, it is not fit for pilot-scale investigations.

Gera et al. (2004) and Chao et al. (2011, 2012a,b) investigated particle segregation and mixing processes in batch fluidized beds by using the Eulerian-Eulerian multi-solid method. In the multi-solid method, as the name implies, two or more types of solids are described as different Eulerian phases in the simulation, and the collision, as well as friction between solids, are accounted for by the solid-solid drag force. The predicted segregation rate of the solids matched quite well with experimental data, and the computation cost was relatively low. Thus, the multi-solid method appears to be a promising alternative strategy for investigating the RTD of solids in horizontal fluidized beds.

Therefore, this section is focusing on the CFD simulations of particles in a continuously operated horizontal fluidized bed. The use of both the species method and the multi-solid method to obtain the RTD of particles is investigated. Comparison and assessment are possible using the data from the RTD experiments which have been explained and discussed in Section 2.3. Geometric parameters such as the presence or not of internal baffles and the height of outlet weir, which have been varied in experiments, are also accounted for in the simulations.

2.4.2 Mathematical models

2.4.2.1 The Eulerian multiphase model

The Eulerian multiphase model has been well developed and applied to simulate fluidized beds for several years. Here, the gas and all solid phases involved are

each treated as a fluid, which indicates that no real granular phases exist. All these phases are defined as interpenetrating continua, the volume fractions of which must add to unity:

$$\alpha_g + \sum_{j=1}^{N} \alpha_{s,j} = 1, \tag{2.14}$$

where N is the total number of granular phases. It will not exceed two in this study.

2.4.2.2 The governing equations for the gas phase

The $k-\varepsilon$ turbulence model, wherein k represents the turbulence kinetic energy and ε is its dissipation rate, is selected for the gas phase in this study. The transport equations for the turbulence kinetic energy and dissipation rate are:

$$\begin{aligned}\frac{\partial}{\partial t}\left(\alpha_g \rho_g k_g\right) + \left(\vec{v}_g \cdot \nabla\right)\left(\alpha_g \rho_g k_g\right) =& \nabla \cdot \left(\alpha_g \left(\mu_g + \frac{\mu_{tu,g}}{\sigma_{k,g}}\right) \nabla k_g\right) \\ &+ \alpha_g G_{k,g} - \alpha_g \rho_g \varepsilon_g,\end{aligned} \tag{2.15}$$

$$\begin{aligned}\frac{\partial}{\partial t}\left(\alpha_g \rho_g \varepsilon_g\right) + \left(\vec{v}_g \cdot \nabla\right)\left(\alpha_g \rho_g \varepsilon_g\right) =& \nabla \cdot \left(\alpha_g \left(\mu_g + \frac{\mu_{tu,g}}{\sigma_{\varepsilon,g}}\right) \nabla \varepsilon_g\right) \\ &+ \alpha_g \frac{\varepsilon_g}{k_g}\left(C_1 G_{k,g} - C_2 \rho_g \varepsilon_g\right).\end{aligned} \tag{2.16}$$

Here, $G_{k,g}$ represents the production of turbulent kinetic energy, which is modeled by using the Boussinesq approximation, and $\mu_{tu,g}$ is the turbulent viscosity of the gas phase, which is modeled as

$$\mu_{tu,g} = \rho_g C_\mu \frac{k_g^2}{\varepsilon_g}. \tag{2.17}$$

In these equations, the constants are $\sigma_{k,g} = 1, \sigma_{\varepsilon,g} = 1.3, C_1 = 1.44, C_2 = 1.92$ and $C_\mu = 0.09$ (Launder and Spalding (1972)).

The continuity equation, which expresses the conservation of mass in the Eulerian reference frame, is written as:

$$\frac{\partial}{\partial t}\left(\alpha_g \rho_g\right) + \nabla \cdot \left(\alpha_g \rho_g \vec{v}_g\right) = 0. \tag{2.18}$$

The momentum balance for the gas phase reads:

$$\frac{\partial}{\partial t}\left(\alpha_g \rho_g \vec{v}_g\right) + \nabla \cdot \left(\alpha_g \rho_g \vec{v}_g \vec{v}_g\right) = -\alpha_g \nabla p + \nabla \cdot \bar{\bar{\tau}}_g + \alpha_g \rho_g \vec{g} - \sum_{j=1}^{N} \vec{K}_{gs,j}, \quad (2.19)$$

where the gas stress-strain tensor $\bar{\bar{\tau}}_g$ is defined as:

$$\bar{\bar{\tau}}_g = \alpha_g \mu_g \left(\nabla \vec{v}_g + \nabla \vec{v}_g^T\right) - \frac{2}{3}\alpha_g \mu_g \left(\nabla \cdot \vec{v}_g\right) \bar{\bar{I}}, \quad (2.20)$$

while the interaction $\vec{K}_{gs,j}$ between the gas phase and the j^{th} solid phase is:

$$\vec{K}_{gs,j} = \beta_{gs,j}\left(\vec{v}_g - \vec{v}_{s,j}\right). \quad (2.21)$$

In Eq. 2.21, β_{gs} is the gas-solid drag coefficient, and it has a notable effect on the prediction accuracy of the hydrodynamics in fluidized bed systems. The drag model proposed by Gidaspow et al. (1991), which combined the model from Wen and Yu (1966) and the Ergun (1952) equation, were validated to be acceptable for simulating the gas-solid flow in bubbling fluidized bed and spouted fluidized bed by Vejahati et al. (2009) and Du et al. (2016), respectively. Thus, the Gidaspow model (Gidaspow et al. (1991)) is applied in this work, and it is defined as:

$$\beta_{gs} = \begin{cases} 0.75 C_D \frac{\alpha_s \alpha_g \rho_g |\vec{v}_s - \vec{v}_g|}{d_s} \alpha_g^{-2.65} & \alpha_g > 0.8 \\ 150 \frac{\alpha_s (1-\alpha_g)\mu_g}{\alpha_g d_s^2} + 1.75 \frac{\rho_g \alpha_s |\vec{v}_s - \vec{v}_g|}{d_s} & \alpha_g \leq 0.8 \end{cases} \quad (2.22)$$

where C_D is the drag coefficient that can be derived based on the relative Reynolds number Re_{rel} of solids:

$$C_D = \frac{24}{\alpha_g Re_{rel}}\left[1 + 0.15\left(\alpha_g Re_{rel}\right)^{0.687}\right] \quad (2.23)$$

where

$$Re_{rel} = \frac{\rho_g d_s |\vec{v}_s - \vec{v}_g|}{\mu_g}. \quad (2.24)$$

2.4.2.3 The governing equations for the solid phase

Similarly, the continuity equation for the j^{th} solid phase reads:

$$\frac{\partial}{\partial t}\left(\alpha_{s,j} \rho_{s,j}\right) + \nabla \cdot \left(\alpha_{s,j} \rho_{s,j} \vec{v}_{s,j}\right) = 0. \quad (2.25)$$

Besides, the momentum balance for the j^{th} solid phase reads:

$$\frac{\partial}{\partial t}\left(\alpha_{s,j}\rho_{s,j}\vec{v}_{s,j}\right)+\nabla\cdot\left(\alpha_{s,j}\rho_{s,j}\vec{v}_{s,j}\vec{v}_{s,j}\right)=-\alpha_{s,j}\nabla p-\nabla p_{s,j}+\nabla\cdot\bar{\bar{\tau}}_{s,j}+\alpha_{s,j}\rho_{s,j}\vec{g}+\vec{K}_{gs,j}+\sum_{\substack{k=1\\k\neq j}}^{n}\vec{K}_{ss,k}, \tag{2.26}$$

where $p_{s,j}$ is the j^{th} solid pressure, and $\bar{\bar{\tau}}_{s,j}$ is the stress tensor for the j^{th} solid phase. In the last term $\vec{K}_{ss,k}$ is the interaction between solid phases (solid phase k and solid phase j), defined as:

$$\vec{K}_{ss,k}=\beta_{ss,k}\left(\vec{v}_{s,k}-\vec{v}_{s,j}\right). \tag{2.27}$$

It only exists when more than one solid phases are defined in the simulation. The solid-solid drag coefficient $\beta_{ss,k}$ will be discussed in Section 2.4.2.4. The kinetic theory of granular flow, which has been proven in numerous studies that can be used for predicting the effective solid stress in fluidized bed systems (Ding and Gidaspow (1990), Gidaspow (1994), Taghipour et al. (2005), Almohammed et al. (2014), Du et al. (2016)), is applied to close the continuity and momentum balance equations of solids. The stress tensor is given by

$$\bar{\bar{\tau}}_{s,j}=\alpha_{s,j}\mu_{s,j}\left(\nabla\vec{v}_{s,j}+\nabla\vec{v}_{s,j}^{T}\right)-\alpha_{s,j}\left(\lambda_{s,j}-\frac{2}{3}\mu_{s,j}\right)\left(\nabla\cdot\vec{v}_{s,j}\right)\bar{\bar{I}}, \tag{2.28}$$

which comprises the shear and bulk viscosities that occur from particle momentum exchange. Specially, in this work, the shear viscosity is composed of a kinetic part and a collision part,

$$\mu_s=\mu_{s,col}+\mu_{s,kin}. \tag{2.29}$$

To them, the models proposed by Syamlal et al. (1993) are applied:

$$\mu_{s,col}=\frac{4}{5}\alpha_s\rho_s d_s g_{0,ss}\left(1+e_{ss}\right)\left(\frac{\Theta_s}{\pi}\right)^{1/2}, \tag{2.30}$$

$$\mu_{s,kin}=\frac{\alpha_s\rho_s d_s\sqrt{\Theta_s\pi}}{6(3-e_{ss})}\left[1+\frac{2}{5}\left(1+e_{ss}\right)\left(3e_{ss}-1\right)\alpha_s g_{0,ss}\right]. \tag{2.31}$$

Furthermore, the bulk viscosity represents the resistance of the solids to compression and expansion. The expression of the bulk viscosity from Lun et al.

(1984) has the following form:

$$\lambda_s = \frac{4}{3}\alpha_s \rho_s d_s g_{0,ss} \left(1 + e_{ss}\right) \left(\frac{\Theta_s}{\pi}\right)^{1/2}. \tag{2.32}$$

The solid pressure occurs in granular flows with less than the maximal solid volume fraction ($\alpha_{s,max} = 0.6$) and consists of two terms, one kinetic term and the other due to particle collisions. According to Lun et al. (1984)

$$p_s = \alpha_s \rho_s \Theta_s + 2\rho_s (1 + e_{ss}) \alpha_s^2 g_{0,ss} \Theta_s, \tag{2.33}$$

where e_{ss} is the restitution coefficient for particle collisions and $g_{0,ss}$ is the radial distribution function. For single solid phase simulation, the radial distribution function is expressed as (Ogawa et al. (1980)):

$$g_{0,ss} = \left[1 - \left(\frac{\alpha_s}{\alpha_{s,max}}\right)^{1/3}\right]^{-1}. \tag{2.34}$$

If multiple solid phases are existing in the simulation (e.g., solid phase j and solid phase k with diameters d_j and d_k, respectively), $g_{0,ss}$ can be extended to

$$g_{0,jk} = \frac{d_{s,j} g_{0,jj} + d_{s,k} g_{0,kk}}{d_{s,j} + d_{s,k}}. \tag{2.35}$$

In Eq. 2.30 to 2.33, the granular temperature Θ_s is introduced as the Maxwellian velocity distribution used for the solids. The granular temperature of the solid phase is proportional to the kinetic energy of random particle movement. The transport equation for the j^{th} solid phase granular temperature is:

$$\begin{aligned} \frac{3}{2}\left[\frac{\partial}{\partial t}\left(\alpha_{s,j}\rho_{s,j}\Theta_{s,j}\right) + \nabla \cdot \left(\alpha_{s,j}\rho_{s,j}\vec{v}_{s,j}\Theta_{s,j}\right)\right] &= \left(-p_{s,j}\bar{\bar{I}} + \bar{\bar{\tau}}_{s,j}\right) : \nabla \vec{v}_{s,j} \\ &\quad - \gamma_{\Theta_{s,j}} - 3\beta_{gs,j}\Theta_{s,j} \\ &\quad - \sum_{\substack{k=1 \\ k \neq j}}^{n} 3\beta_{ss,k}\Theta_{s,j} \end{aligned} \tag{2.36}$$

where the right-hand side terms express the generation of energy by the solid stress tensor, the collisional dissipation of energy, and the energy transfer from the j^{th} solid phase to the gas phase and the k^{th} solid phase, respectively.

2.4.2.4 The RTD simulations

Species method

As mentioned in Section 2.4.1, the solids RTD is predicted by solving a species transport equation when the species method is implemented. With the tracer species denoted by t and the main particle phase denoted by s, this transport equation reads:

$$\frac{\partial}{\partial t}\left(\alpha_s \rho_s C_{t,s}\right) + \nabla \cdot \left(\alpha_s \rho_s \vec{v}_s C_{t,s}\right) = -\nabla \cdot \alpha_s \vec{J}_{t,s}. \tag{2.37}$$

In Eq. 2.37, $C_{t,s}$ is the mass fraction of tracer in the solid phase and $\vec{J}_{t,s}$ is the diffusion flux of tracer that arises from respective gradients. The latter can in turbulent flow be expressed as:

$$\vec{J}_{t,s} = -\left(\rho_s \tilde{D}_t + \frac{\mu_{tu,g}}{Sc_{tu}}\right) \nabla C_{t,s} \tag{2.38}$$

where $\tilde{D}_t$ is the diffusion coefficient of tracer in the fluidized bed, $\mu_{tu,g}$ is the turbulent viscosity as defined in Eq. 2.17, and the turbulent Schmidt number Sc_{tu} is assumed to be constant at 0.7.

Multi-solid method

Two separate solid phases, the solid phase s and the tracer phase t, are defined by using the multi-solid method in this study. The interphase exchange between solid and tracer is represented by the model from Syamlal (1987), which has been applied by many researchers (Gelderbloom et al. (2004), Gera et al. (2004), Du et al. (2016)) for simulating solid mixing and segregation in various fluidized beds. Thus, the tracer-solid interaction coefficient is:

$$\beta_{ts} = \frac{3(1+e_{ts}) g_{0,ts} \alpha_t \rho_t \alpha_s \rho_s (d_t + d_s)^2}{4(\rho_t d_t^3 + \rho_s d_s^3)} \tag{2.39}$$

where, e_{ts} is the coefficient of restitution between tracer and solid (assumed to be with 0.9 equal to the coefficient of restitution between solids e_{ss}, according to the discussion made by Benyahia et al. (2007)); and $g_{0,ts}$ is the radial distribution coefficient, which can be obtained by using Eq. 2.35.

2.4.3 Pre-simulation

The main simulations in this study are going to investigate the RTD of particles in a pilot scale horizontal fluidized bed. Due to the size of the process chamber and long process time, a relatively high computational cost is expected. Therefore, a smaller test horizontal fluidized bed (250 mm (L) × 200 mm (W) × 200 mm ($\tilde{H}$)) with a 35 mm outlet weir was used in some preliminary feasibility studies.

2.4.3.1 Simulation conditions

A schematic drawing of the process chamber of the test horizontal fluidized bed is given in Fig. 2.5. Velocity-inlet was selected as the boundary condition for both the particles and the gas. The gas is uniformly distributed at the gas inlet (bottom of the process chamber), and the superficial gas velocity was set to a constant value of 1.36 m/s in all pre-simulations. At the particle inlet, 1 kg/min of solid flow was constantly fed in. Solid volume fraction was set to 0.6 at the inlet. Outflow boundary conditions were selected for the two exits of the process chamber. For all walls, the no-slip condition was applied for both the gas and solid phases in this study. Besides, in order to achieve the steady state faster, some particles were patched without initial velocity in the process chamber before the simulation started. All simulations were carried out by using the commercial software ANSYS FLUENT 16.1. Important simulation settings are listed in Table 2.6.

2.4.3.2 Grid independence study

To choose a reasonable grid for the main simulations, three different grids (10500 cells, 21000 cells, and 42000 cells) were tested in the preliminary studies. The total volume of particles in the process chamber and the cumulative mass fraction of tracer at the particle outlet were used for judging the influence of grid size. The tracer was introduced into the simulation after a quasi steady state had been established in the fluidized bed (i.e., the time-averaged solid mass flow rate at the outlet and the mass flow rate at the inlet had equalized). At the same time, the mass fraction of tracer was started to be monitored at the outlet. It should be noted that, as introduced in Section 2.4.1, the tracer in the species method was implemented by solving an extra conservation equation (Eq. 2.37) for the tracer species, and on the other hand the tracer in

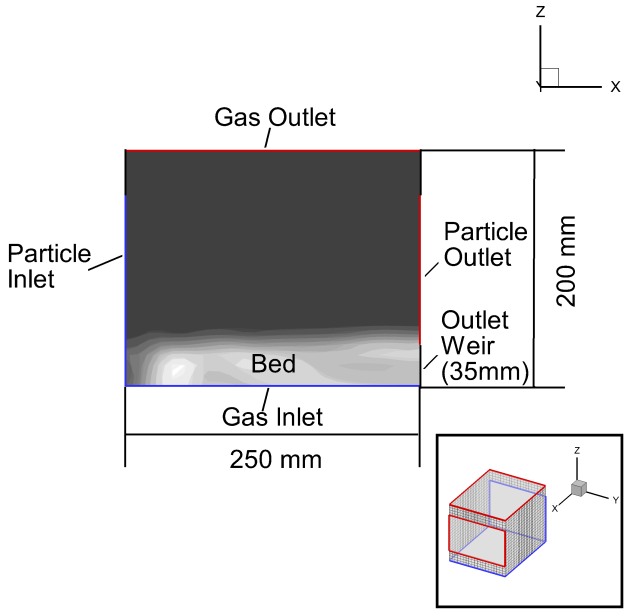

Figure 2.5: Schematic diagram of the test horizontal fluidized bed for preliminary simulations.

Table 2.6: Parameters and models used for all CFD simulations.

Parameter	**Value**	**Unit**
Gas density	1.2	kg/m^3
Gas viscosity	1.8×10^{-5}	kg/ms
Particle density	1040	kg/m^3
Particle diameter	1.8	mm
Tracer density	1040	kg/m^3
Tracer diameter	1.8	mm
Particle mass flow rate	0.0167	kg/s
Maximum solids volume fraction	0.6	-
Time step size	0.001	s
Model		
Tubulence model	k-epsilon, standard, dispersed	
Gas-particle drag coefficient	Gidaspow (Gidaspow et al. (1991))	
Particle-particle drag coefficient	Syamlal-O'Brien-symmetric (Syamlal (1987))	
Granular viscosity	Syamlal-O'Brien (Syamlal et al. (1993))	
Granular bulk viscosity	Lun (Lun et al. (1984))	
Granular temperature	Algebraic (Lun et al. (1984))	
Gradient discretization	Green-Gauss, cell based	

the multi-solid method was added by introducing a secondary solid phase into the Eulerian-Eulerian system. The simulation ended when more than 99% of the tracer had left the process chamber.

Table 2.7: Time-averaged parameters calculated with different grids.

	Species method		**Multi-solid method**	
Grid partition	Bed volume	Mean residence time	Bed volume	Mean residence time
[-]	[m^3]	[s]	[m^3]	[s]
1 (10500 cells)	0.000695	38.85	0.000715	39.10
2 (21000 cells)	0.000711	41.80	0.000722	41.17
3 (42000 cells)	0.000657	36.62	0.000716	41.20

Time-averaged values of particle volume in the bed, calculated by both, the species method and the multi-solid method are listed in Table 2.7, along with mean residence times of particles obtained from the outlet RTD. There is no consistent trend in either bed volume or mean residence time with the number of cells, whereas the variation of both quantities is relatively small. Therefore, grid resolution appears to not significantly influence the simulation result within the investigated range. However, there is a great difference between different resolutions in computational effort. Thus, the coarsest test grid No. 1 was applied to the pilot scale horizontal fluidized bed, details of which will be specified in Section 2.4.4.

2.4.4 Main simulation

2.4.4.1 Mesh and settings

Based on the results from the grid independence study, a computational domain was built for the process chamber (a cuboid with a height of 0.2 m and a rectangular cross section of 1.0 $\times$ 0.2 m^2) of the horizontal fluidized bed. The meshes of the process chambers installed with the two different outlet weirs, with and without internal baffles, are shown in Fig. 2.6. There are 101 nodes in x-direction and 21 nodes in y-direction, respectively, which are all equally distributed. In z-direction, with consideration of the existence of the internal baffles in some simulations and the variation of the outlet weir height, the node distribution (in total 22 nodes) becomes non-uniform. For instance, as

shown in Fig. 2.6, the first row of nodes over the air distributor in z-direction is fixed at 6 mm, because the internal baffles were installed with a gap of 6 mm over the air distributor in the experiment. Likewise, the boundary conditions from Section 2.4.3.1 and the settings in Table 2.6 stay unchanged for all main simulations.

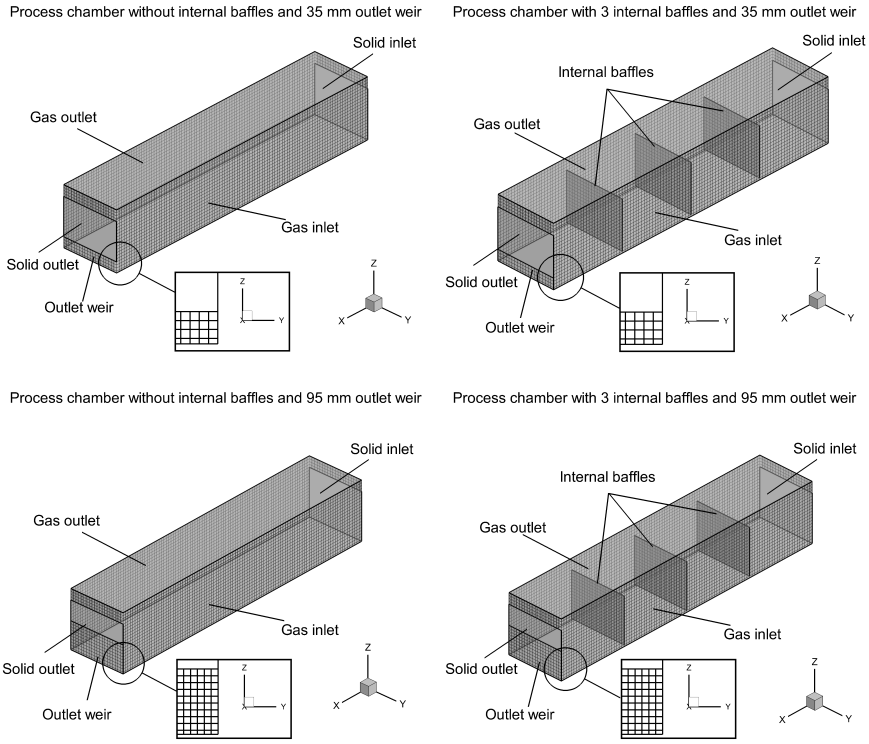

Figure 2.6: Meshes of unbaffled and baffled 3D process chambers with 35 mm and 95 mm outlet weirs.

2.4.4.2 Validation of bed mass and mean residence time

As expressed in the dispersion model (Eq. 2.9) and the definition of the Bodenstein number (Eq. 2.11), the bed velocity is one crucial variable in the numerical simulation, and it is directly related to the mean residence time of particles (Eq. 2.10). However, the mean residence time, which has been used to solve the dispersion model in Section 2.3.6.2, was obtained from the RTD data. This means that we still need to find a solution to estimate the mean residence time without conducting any experiment.

By definition, apart from tracer RTD, the mean residence time of particles in a fluidized bed operated continuously at steady state can also be determined

from the ratio of total bed mass to particle mass flow rate:

$$\tau = \frac{M_b}{\dot{M}_p}, \tag{2.40}$$

and, moreover, the bed mass can also be measured using CFD tool, and it is much faster than the transient RTD simulation. Therefore, two series of (in total eight) CFD simulations with just one solid phase were conducted for the unbaffled horizontal fluidized bed with two different outlet weir heights (35 mm and 95 mm) and used to calculate steady-state bed mass under different superficial gas velocities. Accordingly, the bed mass was also measured in the corresponding experiments carried out as in the CFD for validation.

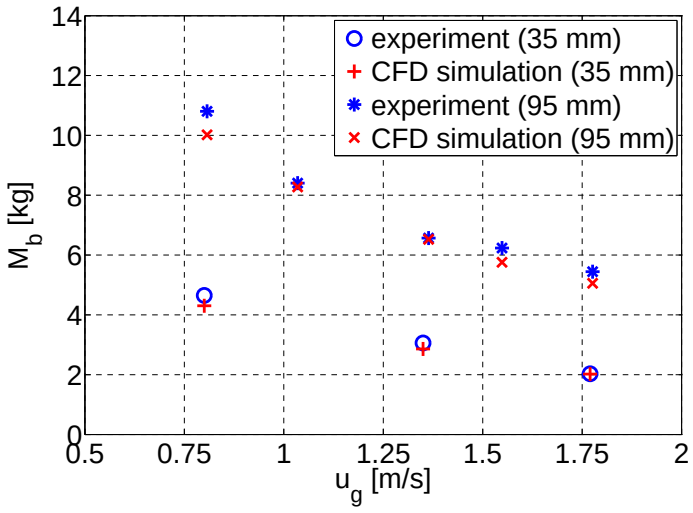

Figure 2.7: Comparison of the measured and simulated total mass of particles in the process chamber under different superficial gas velocities.

The results are plotted in Fig. 2.7. The bed mass decreases with increasing superficial gas velocity, and the CFD results can reliably reproduce this trend. However, the simulated bed mass is smaller than the measured bed mass for all cases, and this leads to a shorter mean residence time of particles in CFD simulations when compared with the experimental data, as depicted in Table 2.8. In general, though, the differences in bed mass and mean residence time between CFD simulations and experiments are relatively low and have been considered to be acceptable in this study. Besides, the simulation domain is four times bigger than the one used for the grid-independence study, which also illustrates that CFD simulation still can well predict particle fluidization

behavior after the geometrical scaling up.

Table 2.8: Total bed mass and mean particle residence time for different superficial gas velocities from experiments and CFD simulations.

u_g	M_b		τ	
$[m/s]$	$[kg]$		$[s]$	
35 mm	Exp.	Sim.	Exp.	Sim.
0.80	4.65	4.30	278.4	257.5
1.35	3.06	2.86	183.2	171.3
1.70	2.03	2.02	121.6	120.9
95 mm	Exp.	Sim.	Exp.	Sim.
0.81	10.81	10.02	647.3	600.0
1.04	8.40	8.28	502.9	495.8
1.36	6.57	6.53	393.4	391.0
1.55	6.23	5.76	373.0	344.9
1.78	5.44	5.06	325.7	302.9

2.4.4.3 RTD simulations: species method

RTD simulations with the species method were conducted, and firstly, the reliability of using the species method to predict the RTD was verified. Four experiments (No. 1, No. 2, No. 5 and No. 6) were selected as references for the CFD simulations, which means that the setting of the corresponding RTD simulations is utterly consistent with the experiments. In addition, because we don't have any other indication about the value of the diffusion coefficient of the tracer and we cannot assume scale separation in the fluidized bed (the geometrical configuration of it is expected to directly (e.g., baffles) and indirectly (e.g., bubbles) influence the mobility of particles), the diffusion coefficient of the tracer, which is the key input variable of the species method, was set according to the dispersion coefficient of particles obtained from the experiment (Table 2.5).

Results of transient simulations are plotted against experimental data in Fig. 2.8. As can be seen, simulated curves fit relatively well to the experimental data, whereby the simulated curves of fluidized beds without internal baffles (simulations No. 1 and No. 3) have a higher consistency. Later, the mean residence time was calculated based on the simulated RTD curves, and the dispersion coefficient was obtained by fitting the dispersion model to the simulated RTD curve. By comparing Table 2.3 and Table 2.9, it can be seen

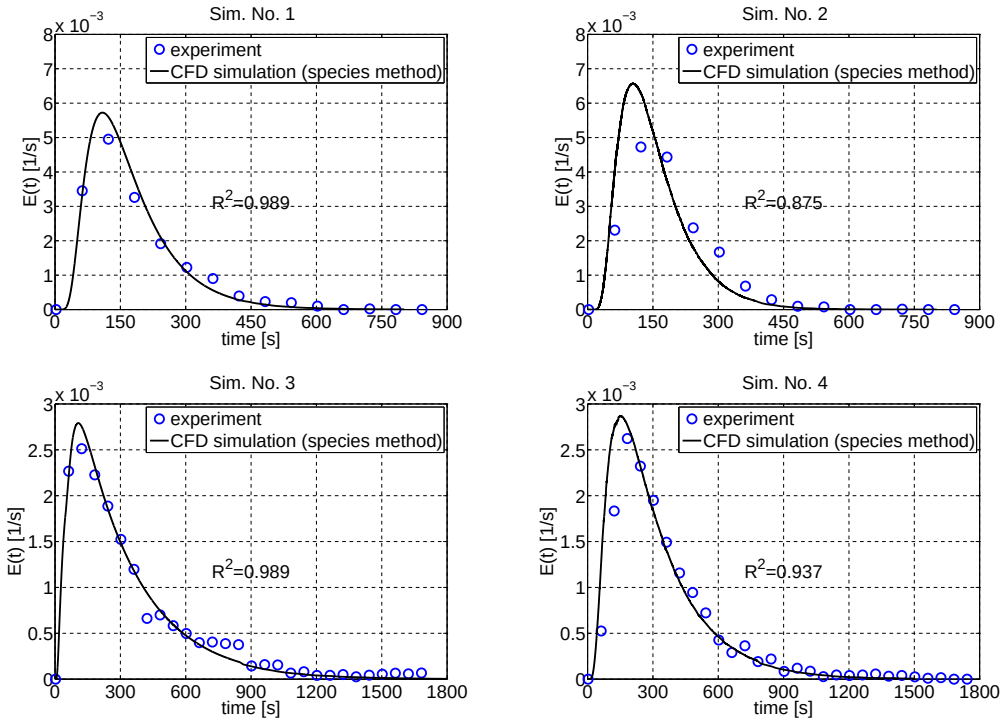

Figure 2.8: Comparison of CFD simulation results (species method) with RTD experimental data.

that all simulated mean residence times are smaller (on average by 9.6%) than the experimental results. Nevertheless, as discussed Section 2.4.4.2, a slightly lower mean residence time does not show significant influence on the RTD curves. Besides, the mean residence time only slightly changes and the dispersion coefficient decreases after adding internal baffles when the outlet weir height stays constant, which all show good coincidence with the experiment results. Nonetheless, the dispersion coefficient obtained from simulated RTD curves is never equal to the input diffusivity of tracer (compare Table 2.9 with Table 2.5, corrected D for experiments No. 1 and 2, empirical D for experiments No. 5 and 6). Such equality cannot be expected, because dispersion coefficients are by definition macroscopic, whereas tracer diffusivity is supposed to capture particle mobility at the microscale. However, from another perspective, actually, the microscopic property (tracer diffusivity) and the macroscopic property (dispersion coefficient) are close by, though not identical.

Indeed, the best way of predicting the RTD behavior by using the species method seems to consist in setting those two quantities equal to each other, which would though mean that the dispersion in any specific fluidized bed

Table 2.9: Summary of RTD properties from CFD simulations using the species method.

Sim. No. [−]	τ [s]	Relative change (Exp. τ based) [%]	D (simulated) [m^2s^{-1}]	Relative change (Input D based) [%]	R^2 (vs. Exp.) [−]
1	171.6	−6.0	0.00101	−27.9	0.989
2	165.3	−10.5	0.00087	8.8	0.875
3	307.6	−12.7	0.00231	35.1	0.989
4	320.3	−9.2	0.00118	14.5	0.937

needs to be known before its influence on RTD behavior can be calculated. This would be a tautology, but it is relaxed by the results gained along the fluidized bed, as the species method can be used to record particle RTD at an arbitrary distance from the inlet of the apparatus.

As indicated in Fig. 2.1, three internal baffles, equally dividing the process chamber into four compartments, were installed over the air distributor and particles can only pass through the opening gap as an underflow. The corresponding particle RTDs at these gaps were also recorded in simulations No. 2 and No. 4, as presented in Fig. 2.9(a) and Fig. 2.9(b). Accordingly, the particle dispersion coefficients from the corresponding RTD curves, the mean residence time of particles from the inlet to the recording point, and the bed mass of particles in each compartment as shown in Table 2.10 are calculated.

Table 2.10: Values calculated from the residence time distributions at different longitudinal positions from CFD simulations.

Position [−]	D (from RTD) [m^2s^{-1}]	τ (from RTD) [s]	M_b (in each chamber) [kg]
Sim. No. 2			
Gap 1 (0.25 m)	0.00138	53.1	0.89
Gap 2 (0.5 m)	0.00118	98.1	0.75
Gap 3 (0.75 m)	0.00113	137.8	0.66
Outlet (1 m)	0.00087	165.3	0.46
Sim. No. 4			
Gap 1 (0.25 m)	0.00273	112.1	1.87
Gap 2 (0.5 m)	0.00172	222.2	1.84
Gap 3 (0.75 m)	0.00137	287.8	1.09
Outlet (1 m)	0.00118	320.3	0.54

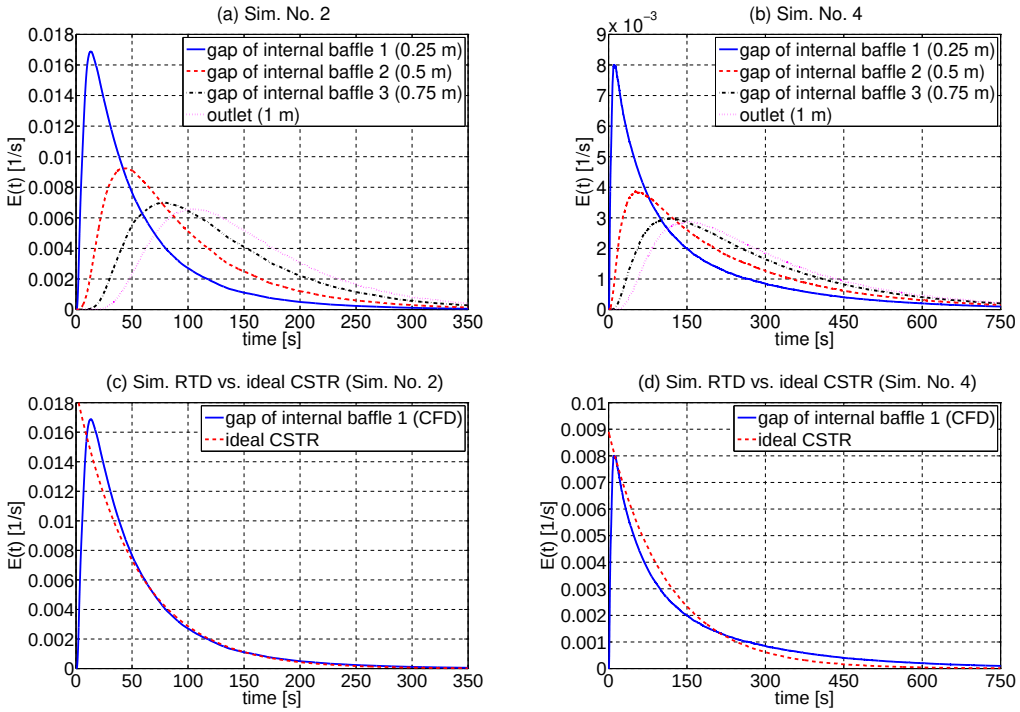

Figure 2.9: Particle RTD curves monitored at the positions of the three internal baffles and at the outlet of the fluidized bed by means of the species method for (a) simulation No. 2 (35 mm outlet weir), (b) simulation No. 4 (95 mm outlet weir), and a comparison of the RTD curve monitored at the outlet gap of the first chamber with the corresponding RTD curve of an ideal CSTR ((c) and (d)).

As can be seen, for both cases, a mass gradient appears in the process chamber, that is, the total mass of particles in each compartment decreases with increasing compartment number. This mass gradient directly leads to the movement of particles from the inlet to outlet in the horizontal fluidized bed. Moreover, the first compartment always has the highest level of dispersion, and it is close to one perfect CSTR, as plotted in Fig. 2.9(c) and Fig. 2.9(d). However, the particle movement along the horizontal fluidized bed cannot be expected to be fully and accurately predicted; for instance, a significant difference of bed mass between second and third compartment was observed in the simulation No. 4.

The influence of the input value of the diffusivity of tracer was further investigated by conducting three additional CFD simulations with tracer diffusivity of 0.1 m^2/s, 0.01 m^2/s and 0.001 m^2/s, respectively. The geometry of process chamber and all other parameters used corresponded to those of simulation No.

1. The simulated RTD curves are depicted in Fig. 2.10 and differ, as expected, significantly. Only the simulation result using the smallest diffusivity of tracer (D = 0.001 m^2/s), which is close to the input value (D = 0.00141 m^2/s) of simulation No. 1, is in good accordance with the experimental data. Thus, for the species method, a relatively accurate diffusivity of tracer is necessary in order to reliably predict the dispersion of particles in the pilot scale horizontal fluidized bed.

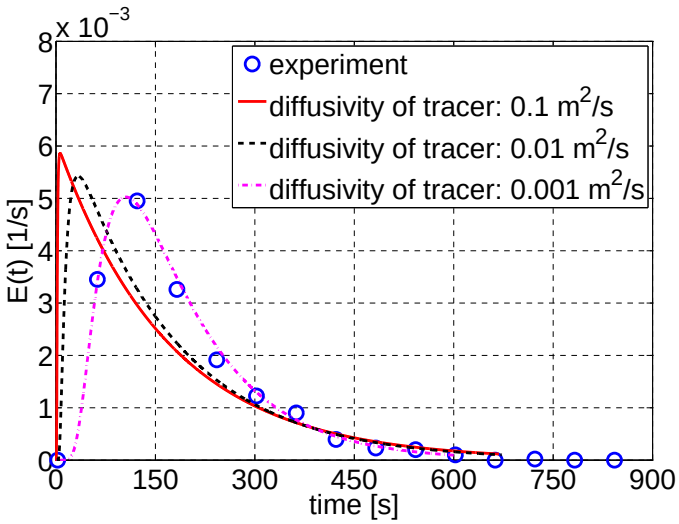

Figure 2.10: Particle RTD curves by using different diffusivities of tracer for fluidized bed without internal baffles and 35 mm outlet weir (otherwise corresponding to simulation No. 1).

2.4.4.4 RTD simulations: multi-solid method

The species method has been confirmed to be very dependent on the diffusivity of particles and not to be applied if this is unknown. Thus, the multi-solid method which can estimate the RTD without previous knowledge of the diffusivity of particles was also investigated.

As described in Section 2.4.2.4, the tracer was defined as an independent solid phase in the multi-solid method, and the simulated RTD curves are plotted against experimental data in Fig. 2.11. Overall, the simulated RTD curves provide an acceptable good fit to the experimental data (the smallest coefficient of determination R^2 is 0.919). As presented in Table 2.11, in comparison to the species method, the mean residence times calculated from the corresponding RTD curves by using the multi-solid method are closer to

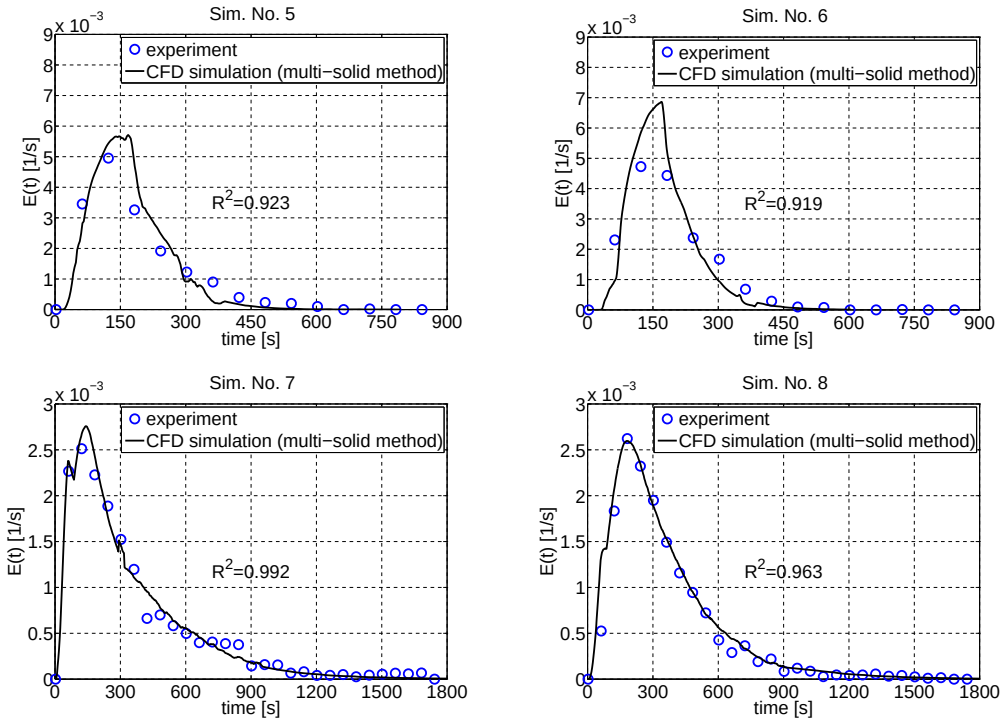

Figure 2.11: Comparison between CFD simulation results (multi-solid method) and RTD experimental data.

the experimental values (the average absolute error is 4.7%). Moreover, as can be seen, none of the simulated RTD curves is smooth, which may be closer to reality. One interpretation of this phenomenon is that the tracer can only leave the fluidized bed as an overflow and the outflow is always fluctuating at the outlet. The obtained dispersion coefficients also seem to competently represent the dispersion of particles in horizontal fluidized beds with different geometries and operation parameters. The influence of the internal baffles is credibly predicted, in accordance with the experimental data and the simulation results of the species method.

2.4.4.5 Simulation acceleration

Transient vs. steady state (species method)

All the aforementioned CFD simulations were performed on a 64-bit personal computer (4-core 4.0 GHz Intel(R) Core(TM) i7-6700K with 32G of RAM). As the particle flow was always fluctuating at the outlet, the simulations were carried out in transient mode, which means all the governing equations (for

Table 2.11: RTD properties calculated from CFD simulations conducted by the multi-solid method.

Sim. No. [−]	τ [s]	Relative change (Exp. τ based) [%]	D (from RTD) [$m^2 s^{-1}$]	R^2 (vs. Exp.) [−]
5	171.9	−5.9	0.00081	0.923
6	173.1	−6.2	0.00049	0.919
7	329.3	−6.6	0.00232	0.992
8	353.1	0.1	0.00108	0.963

flow, volume fraction and turbulence) were solved and updated in each iteration. This leads to long wall-clock times for simulating a pilot scale process by using the CFD tools, as depicted in Table 2.12

Table 2.12: A comparison of the transient approach with the steady state approach by using species method.

Time information	Unit	Transient	Steady state
process time step size	[s]	0.001	0.01
average real time per time step	[s]	2.208	0.063
average real time per process time	[−]	2208	6.3

As we have seen, in the species method the RTD is measured by solving the species transport equation, and this would not influence the gas-solid flow behavior in the process chamber. Thus, an alternative computation method, denoted by steady state approach, was also carried out for acceleration of the simulation, using again the species method.

The fluidized bed is assumed to have reached a steady state when the time-averaged particle mass flow equals the feed rate. The gas-solid flow field is then memorized and stays unchanged, which means that the flow equations, volume equations, and turbulence equations are not solved anymore afterward. Then the tracer is added, and only the species equation is solved. As shown in Fig. 2.12, the obtained RTD curves show some deviations from the simulation results using the transient approach, in which the flow field is always changing for each time step and may be expected to be closer to reality. However, trends are similar, and the RTD curves from the two approaches do not differ dramatically. On the other hand, as presented in Table 2.12, the process time step size can be decreased significantly, because only the diffusion equation is solved and the average real time per time step also decreases radically by using

the steady state approach. Thus, the species method combined with the steady state approach can be regarded as a coarse but practicable way to investigate particle RTD in the horizontal fluidized bed or similar devices.

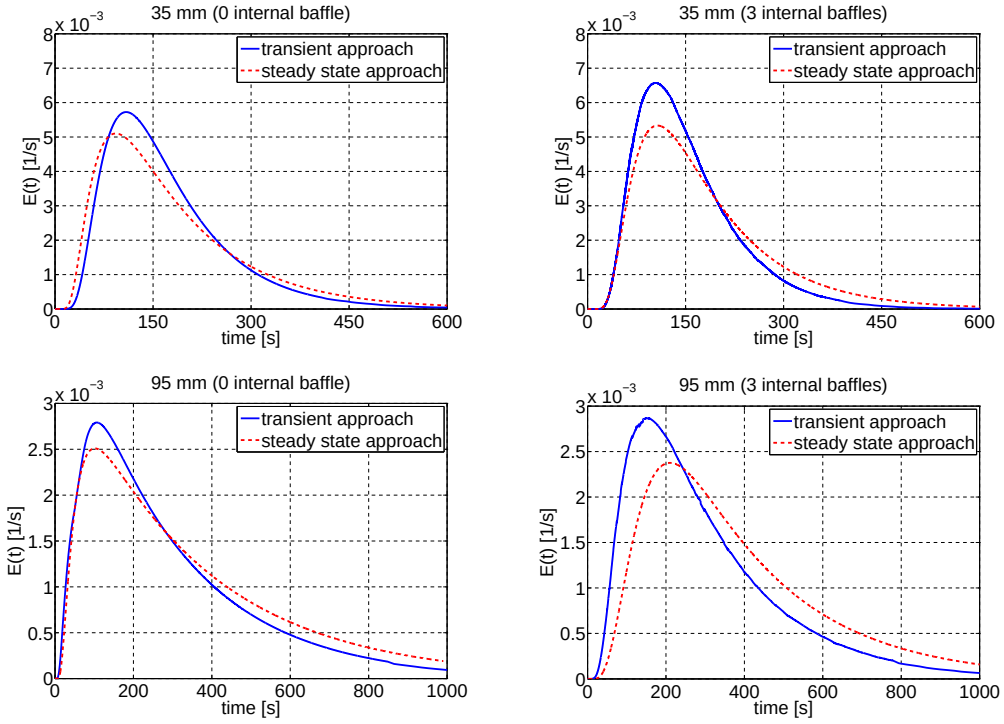

Figure 2.12: CFD simulation (species method) results by using either the transient or the steady state computational approach.

2D versus 3D

Another strategy often used to accelerate CFD simulations is to simplify the three-dimensional (3D) geometry into a two-dimensional (2D) simulation domain. Many researchers, for instance, Cooper and Coronella (2005), Sun and Battaglia (2006), Chang et al. (2011), Herzog et al. (2012), etc., have successfully used 2D simulations to investigate the mixing or segregation behavior of solids in a batch fluidized bed.

Likewise, a 2D computational domain of the earlier mentioned test horizontal fluidized bed was established, and RTD simulations using the species method and the multi-solid method were conducted in both the 2D and the 3D domains. The simulation results are presented in Fig. 2.13. It is evident that no matter whether the species method or the multi-solid method is applied, a large difference between RTD curves from 2D and 3D simulations can be observed.

In general, the particles stay longer in the apparatus when the 2D domain is used. The reason is most probably that many properties are simplified in the 2D simulation, e.g., the strain and stress in the third direction are simulated based on certain assumptions. Thus, in summary, the 2D computational domain is not compatible with the RTD simulation for the horizontal fluidized bed.

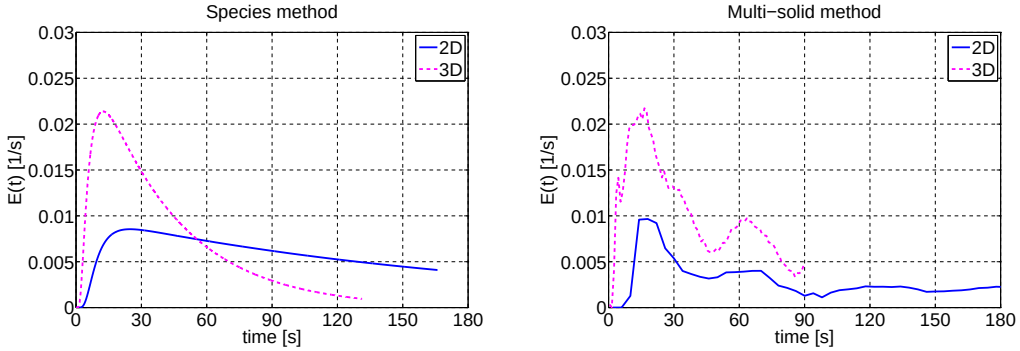

Figure 2.13: A comparison of the simulated RTD curves using 2D and 3D computational domains.

2.5 Conclusion

The particle RTD of a pilot-scale horizontal fluidized bed was systematically investigated in this chapter. Several important theoretical terms and concepts regarding the RTD were illustrated in details.

The RTD was investigated by means of experiments, and the influence of process parameters (superficial gas velocity) and geometrical features (baffles and outlet weir) were discussed. Moreover, the experiment results were also used as the benchmark for later validating the accuracy of different numerical modeling results. Two alternative mathematical models, the TIS model and the dispersion model, were proved to be reasonable for predicting particle RTD in the horizontal fluidized bed. Besides, the number of theoretical tanks and the dispersion coefficient, the critical parameters of the respective model, were further discussed.

The species method and the multi-solid method, which can be applied for RTD measurement in CFD simulations, were introduced and studied. The CFD simulation results show that both methods were able to predict particle RTD in transient mode correctly. In the species method, the diffusivity of the particles is the key variable, and this method is only applicable when one

macroscopically identified in-range dispersion coefficient, which was obtained from the experimental data as well as from empirical correlations in this work, is attainable for evaluating the particle diffusivity.

Besides, as presented at the end of this chapter, different approaches were discussed for accelerating the RTD simulation of the pilot scale equipment. The steady state computational approach can be applied when the species method is used and the obtained RTDs still can represent the real process, whereas the 2D simulation appears to be inapplicable for both methods. Although the multi-solid method can only be solved in transient mode with a relatively high computational cost, the particle RTD information can be directly obtained without knowing the diffusivity of the tracer with the help of this method, which shows its broad application prospects for apparatus design and development.

Chapter 3

Particle Drying in Horizontal Fluidized Bed

This chapter has been partly taken from: Chen, K., Bachmann, P., Bück, A., Jacob, M., and Tsotsas, E. (2017). Experimental study and modeling of particle drying in a continuously-operated horizontal fluidized bed. Particuology, 34:134–146.

3.1 Overview

One of the most common industrial processes that can be conducted in a horizontal fluidized bed is drying. The horizontal fluidized bed is different from traditional drying equipment (e.g., drying oven, tray dryer), because this type of apparatus cannot only be applied as a continuous dryer, but also has a broader application in particle wet formulation processes (like agglomeration, granulation, and coating). In such applications, the drying process plays an important role on the final product quality.

Commonly, a relative intense hydrodynamic interaction between gas and solid flows exists in the horizontal fluidized bed, and this results in strong mixing and intense heat and mass transfer between the two phases. In this chapter, the particle drying process in a horizontal fluidized bed is systematically investigated. Section 3.2 firstly describes various horizontal fluidized bed dryer models. Then, the specifics of the reference drying and RTD experiments, and some important characteristic properties obtained by post-processing experimental data are described in Section 3.3. In Section 3.4, simulation results from different models are compared and validated with the experimental data. Novelties of the models, which have been developed based on the mixing flow assumptions, are also

provided by comparing with reference data. Moreover, two sets of parametric studies are conducted.

Research presented in this chapter has been conducted jointly with Philipp Bachmann. The present author focused on modeling, whereas Bachmann contributed experimental methods and results. The latter will thus be discussed in more details in his PhD thesis, which is under preparation.

3.2 Model development

3.2.1 Modeling of particle movement

To simulate a horizontal fluidized bed dryer, a focal point is the description of the movement of particles. As introduced in Section 2.2.1, based on the phenomenon of gas-solid mixture flow in the continuous fluidized bed, the flow pattern of particles can generally be classified into two types: non-mixing flow (plug flow) and mixing flow (mixed flow or back-mixing flow). Accordingly, these solid flow patterns can be implemented respectively into simulations with different assumptions which are specified in the following subsections.

3.2.1.1 Non-mixing flow: plug flow (PF) model

Horizontal fluidized beds are considered as plug flow fluidized beds by many researchers (Wanjari et al. (2006), Bizmark et al. (2010), Khanali et al. (2012)) in literature, because one of the ideal flow patterns of particles is plug flow. Hence, although the model based on the assumption of plug flow (in the following named as "plug flow (PF) model") is an ideal model, it can certainly provide some information about the behavior of solids drying in a horizontal fluidized bed.

In the plug flow model, the dispersion effect is neglected during the movement of particles, that is, all the solids which enter the fluidized bed at the same moment are assumed to leave the apparatus after the same residence time τ. For a fluidized bed with total bed mass $M_{b,tot}$ under steady state, the solid mass flow rate at the outlet $\dot{M}_{p,out}$ can be written as

$$\dot{M}_{p,out} = \frac{M_{b,tot}}{\tau}, \tag{3.1}$$

which relates directly to the average moisture content ($\bar{X}_{p,out}$) and enthalpy

($\bar{H}_{p,out}$) of the particles at the outlet, while the heat and mass balances of the whole fluidized bed are:

$$\frac{dM_{b,tot}}{dt} = \dot{M}_{p,in} - \dot{M}_{p,out}, \tag{3.2}$$

$$\frac{d(M_{b,tot}\bar{X}_p)}{dt} = \dot{M}_{p,in}\bar{X}_{p,in} - \dot{M}_{p,out}\bar{X}_{p,out} - \dot{M}_{pg}, \tag{3.3}$$

$$\frac{d\bar{H}_p}{dt} = \dot{M}_{p,in}\bar{h}_{p,in} - \dot{M}_{p,out}\bar{h}_{p,out} - \dot{H}_{pg} - \dot{Q}_{pW} + \dot{Q}_{gp}. \tag{3.4}$$

Here, all particles are treated as having identical moisture content at the inlet $\bar{X}_{p,in}$ and the specific enthalpy of particles h_p is defined as:

$$h_p = \frac{H_p}{M_p} = \vartheta_p(c_p + X_p c_w), \tag{3.5}$$

which can also be used to calculate particle temperature.

Besides, as depicted in Fig. 3.1, for a random selected internal control volume l, because the solid mass flow rate is assumed to be constant, the corresponding mean residence time τ_l will be proportional to the size of the control volume (the bed mass $M_{b,l}$). Consequently, Eq. 3.1 can be extended as:

$$\dot{M}_{p,out} = \frac{M_{b,tot}}{\tau} = \frac{M_{b,l}}{\tau_l}, \tag{3.6}$$

so the plug flow horizontal fluidized bed can be simulated as a connection of several small plug flow control volumes, which makes it possible to obtain the drying information along the horizontal direction of the apparatus.

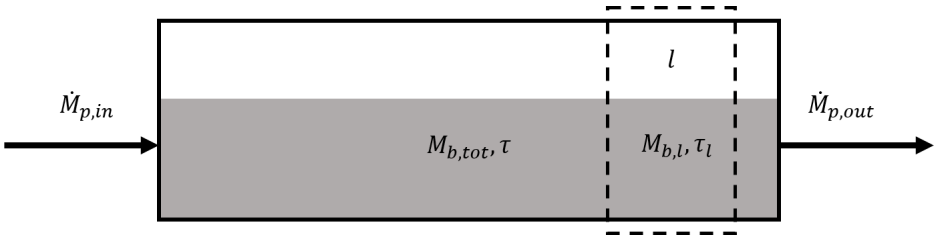

Figure 3.1: Scheme of the mass balance of particles in the plug flow model.

3.2.1.2 Mixing flow: mixed flow model and back-mixing flow model

Obviously, the plug flow model neglects the particle mixing effect, which can directly result in an RTD of solids in the apparatus, and in non-uniform residence time of solids that plays a big role in the drying processes in industry. As mentioned in the general assumptions (Section 3.2.2.1), particles are perfectly mixed in vertical direction, so that dispersive transport of particles is only considered in horizontal direction of the fluidized bed. Consequently, the characterization of particle transport can be achieved via the RTD of particles, which would be implemented into simulation through the mixed flow model and the back-mixing flow model in this work, respectively.

For the mixed flow model, on the one side, as summarized by Daud and Ramli (2008), the horizontal fluidized bed can be described by the connection of a series of equally sized mixed flow fluidized beds (CSTRs), which are briefly presented in Fig. 3.2(a). On the other side, for the back-mixing flow model, the transportation of particles in the horizontal fluidized bed can be simulated from a macroscopic perspective. As plotted in Fig. 3.2(b), the entire device is assumed to be one "black box", and the back-mixing effect of particles from the inlet to the outlet can be represented by the RTD directly.

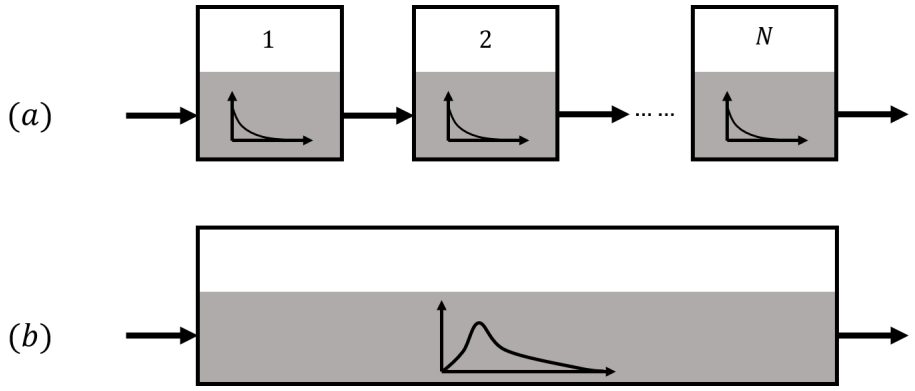

Figure 3.2: Schematic of simulation models of mixing flow horizontal fluidized bed: (a) Mixed flow model: a connection of N mixed flow fluidized beds of equal size; (b) Back-mixing flow model: the "black box" model simulates the fluidized bed via the RTD distribution directly.

In general, no matter whether the mixed flow model or the back-mixing flow model is used, the key factor of modeling the mixing flow fluidized bed is that of a proper implementation of the RTD of particles into the drying model.

One-dimensional population balance drying (1D-PBD) model

The residence time behavior of the wet particles can be modeled using a one-dimensional population balance drying (1D-PBD) model in the simulation. In this model, the density function of the residence time distribution, which is the normalized residence time distribution, can be expressed as (Burgschweiger and Tsotsas (2002)):

$$n(\tau,t)=\frac{1}{M_{b,tot}(t)}\frac{\partial M_p(\tau,t)}{\partial\tau}, \tag{3.7}$$

where the total bed mass at each moment is calculated by

$$M_{b,tot}(t)=\int_0^\infty M_p(\tau,t)n(\tau,t)\mathrm{d}\tau. \tag{3.8}$$

Furthermore, based on Eq. 3.7, three population balance equations for the particles are derived:

$$\frac{\partial(M_p n)}{\partial t}+\frac{\partial(M_p n)}{\partial\tau}\frac{\partial\tau}{\partial t}=-\dot{M}_{p,out}n+\dot{M}_{p,in}n, \tag{3.9}$$

$$\frac{\partial(M_p n\bar{X}_p)}{\partial t}+\frac{\partial(M_p n\bar{X}_p)}{\partial\tau}\frac{\partial\tau}{\partial t}=-\dot{M}_{p,out}n\bar{X}_{p,out}+\dot{M}_{p,in}n\bar{X}_{p,in}-\frac{\partial\dot{M}_{pg}}{\partial\tau}, \tag{3.10}$$

$$\begin{aligned}\frac{\partial(M_p n\bar{h}_p)}{\partial t}+\frac{\partial(M_p n\bar{h}_p)}{\partial\tau}\frac{\partial\tau}{\partial t}=&-\dot{M}_{p,out}\bar{h}_{p,out}n+\dot{M}_{p,in}\bar{h}_{p,in}n\\&+\frac{\partial(-\dot{H}_{pg}-\dot{Q}_{pW}+\dot{Q}_{gp})}{\partial\tau}.\end{aligned} \tag{3.11}$$

As can be seen, like in the PF model, the mean moisture content of particles is applied for all populations at the inlet in the 1D-PBD model. Moreover, based on the differences in particle residence time, not only the mean moisture content but also a particle moisture content distribution can be obtained at the outlet. This distribution is one of the most important criteria for judging the performance of a horizontal fluidized bed dryer.

Two-dimensional population balance drying (2D-PBD) model

However, a distribution of particle moisture content often occurs at the inlet, as observed in the experiments. In this study, the effect of variable particle moisture content is described by adding a second dimension to the population balance model. Therefore, the corresponding density function of the two-dimensional population balance drying (2D-PBD) model is given by:

$$\tilde{n}(\tau, X, t) = \frac{1}{M_{b,tot}(t)} \frac{\partial^2 M_p(\tau, X, t)}{\partial \tau \partial X}. \tag{3.12}$$

Here, M_p is the dry-based mass of all particles having the same residence time τ and moisture content X. The total bed mass $M_{b,tot}$ at every time point t is calculated as

$$M_{b,tot}(t) = \int_0^\infty \int_0^\infty M_p(\tau, X, t)\tilde{n}(\tau, X, t)\mathrm{d}\tau\mathrm{d}X. \tag{3.13}$$

The individual properties of a specified particle class (e.g., particle mass $M_{p,i,m}$, moisture content $X_{p,i,m}$, and specific enthalpy $h_{p,i,m}$) will differ from the properties of other particle classes in the population. Based on this, three population balance equations can be derived:

$$\frac{\partial(M_p\tilde{n})}{\partial t} + \frac{\partial(M_p\tilde{n})}{\partial \tau}\frac{\partial \tau}{\partial t} + \frac{\partial(M_p\tilde{n})}{\partial X}\frac{\partial X}{\partial t} = -\dot{M}_{p,out}\tilde{n} + \dot{M}_{p,in}\tilde{n}, \tag{3.14}$$

$$\begin{aligned}\frac{\partial(M_p\tilde{n}X_p)}{\partial t} + \frac{\partial(M_p\tilde{n}X_p)}{\partial \tau}\frac{\partial \tau}{\partial t} + \frac{\partial(M_p\tilde{n}X_p)}{\partial X}\frac{\partial X}{\partial t} =& -\dot{M}_{p,out}\tilde{n}X_{p,out} + \dot{M}_{p,in}\tilde{n}X_{p,in} \\ & - \frac{\partial^2 \dot{M}_{pg}}{\partial \tau \partial X},\end{aligned} \tag{3.15}$$

$$\begin{aligned}\frac{\partial(M_p\tilde{n}h_p)}{\partial t} + \frac{\partial(M_p\tilde{n}h_p)}{\partial \tau}\frac{\partial \tau}{\partial t} + \frac{\partial(M_p\tilde{n}h_p)}{\partial X}\frac{\partial X}{\partial t} =& -\dot{H}_{p,out}\tilde{n} + \dot{H}_{p,in}\tilde{n} \\ & + \frac{\partial^2(-\dot{H}_{pg} - \dot{Q}_{pW} + \dot{Q}_{gp})}{\partial \tau \partial X}.\end{aligned} \tag{3.16}$$

3.2.2 Particle drying model

Aside from the modeling of particle movement, the particle drying mechanism should also be specified. In literature, various drying kinetic approaches for

fluidized beds can be found, e.g., Wang et al. (2007), Bertin et al. (2011), and Khanali et al. (2013). Here, the comprehensive particle drying model developed by Burgschweiger et al. (1999), the accuracy of which has been validated by experimental results, was applied in this work.

3.2.2.1 General assumptions

The major assumptions of the particle drying model are summarized as following:

(a) The gas flow is formally regarded as plug flow, though gas back-mixing is indirectly accounted for by the use of the gas-to-particle heat and mass transfer coefficients proposed by Groenewold and Tsotsas (1997).

(b) The solids are perfectly mixed in the vertical direction. One single particle can be thus used to represent the other particles under the same conditions (e.g., identical residence time, same physical properties, etc.).

Also, another assumption compatible with the drying model is used, which is:

(c) Bubble and suspension phase are not distinguished, which means they are merged into one general gas phase.

3.2.2.2 Drying kinetics

Figure 3.3 briefly illustrates the mass and heat transfer between solid phase, gas phase, and wall in the fluidized bed. All kinetic relations for the various mass and heat flow terms need to be specified.

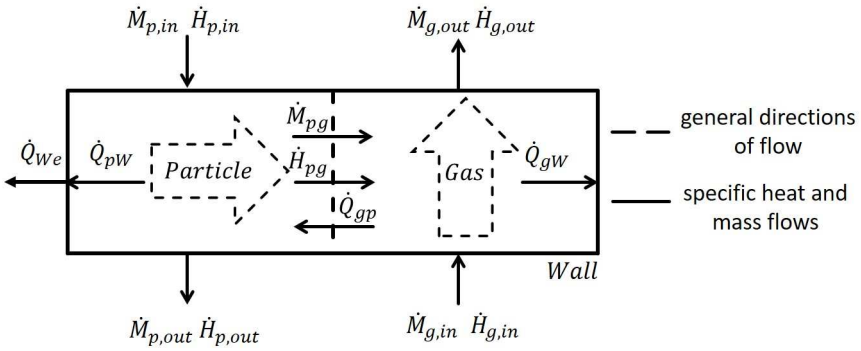

Figure 3.3: Scheme of heat and mass transfer in the horizontal fluidized bed.

The hot gas continuously provides heat to the particle surface, and the heat flow rate can be expressed as:

$$\dot{Q}_{gp} = \tilde{\alpha}_{gp} A_p (\vartheta_g - \vartheta_p). \tag{3.17}$$

In Eq. 3.17, $\tilde{\alpha}_{gp}$ is the heat transfer coefficient calculated according to Groenewold and Tsotsas (1999) (the corresponding equations are presented in Appendix A), inherently accounting for gas back-mixing , and A_p is the total particle surface area. The continuous heat flow results in evaporation of the water contained in particle, and the enthalpy flow rate of the vaporized component is:

$$\dot{H}_{pg} = \dot{M}_{pg} \left(c_{\mathrm{v}} \vartheta_g + \Delta h_{\mathrm{v}} (0^o C) \right), \tag{3.18}$$

where $\dot{M}_{pg}$ is the water evaporation rate. According to Burgschweiger et al. (1999), the mass transfer between particle and gas is calculated from the following equation:

$$\dot{M}_{pg} = \tilde{\beta}_{pg} \rho_g A_p (Y_{sat} - Y_g) \dot{\nu}. \tag{3.19}$$

Here, $\tilde{\beta}_{pg}$ is the mass transfer coefficient analogous to α_{gp} (for details see Appendix A), $\dot{\nu}$ is the normalized single particle drying rate, and Y_{sat} is the adiabatic saturation moisture content of the gas. As introduced in Section 1.2.4, the drying kinetics of a specific material can be represented by the normalized drying rate $\dot{\nu}$. In the second drying period, the normalized drying rate $\dot{\nu}$ becomes a function of another essential drying term, the normalized particle moisture content η, which is defined as:

$$\eta = \frac{X_p - X_{p,eq}}{X_{p,cr} - X_{p,eq}}, \tag{3.20}$$

where, X_p is particle moisture content, $X_{p,cr}$ is critical particle moisture content, and $X_{p,eq}$ is equilibrium particle moisture content. For sufficient large particles, the normalized drying curve can be measured by putting a single particle either on a micro-balance or in a drying channel and recording its weight change during the drying process. Burgschweiger et al. (1999) as well as Groenewold and Tsotsas (2001) investigated in this way and carried out the correlation between normalized particle moisture content η and the normalized drying rate $\dot{\nu}$ for alumina particles of different sizes. Figure 3.4 shows the characteristic drying curves of two relatively large alumina particles. As can be seen, the function $\dot{\nu}(\eta)$ depends not only on the type of material but also on the size of the material. Besides, the adiabatic saturation moisture content of the gas Y_{sat}

can be calculated with:

$$Y_{sat} = 0.622 \frac{p_{sat}}{p - p_{sat}}. \tag{3.21}$$

The water vapor pressure at adiabatic saturation p_{sat} depends on the temperature of the saturated gas ϑ_{sat} (Appendix B), which can be iteratively calculated by solving the following equation:

$$\vartheta_{g,in} - \vartheta_{g,sat} = \frac{\Delta h_v\,(0^oC) + (c_v + c_w)\,\vartheta_{g,sat}}{c_g + Y_{in} c_v} \left(Y_{sat} - Y_{in}\right). \tag{3.22}$$

Here, $\vartheta_{g,in}$ and Y_{in} respectively represent the temperature and moisture content of the inlet gas.

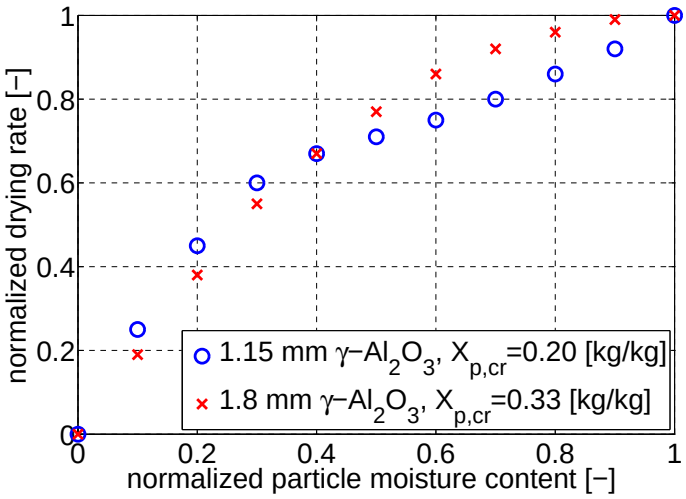

Figure 3.4: Normalized drying curves for large γ-Al_2O_3 particles (Groenewold and Tsotsas (2001)) in the second drying period.

3.2.2.3 Balance equations of gas phase

Based on the assumptions for the gas phase, the gas phase is discretized in the vertical direction of air flow. Figure 3.5 shows the mass and heat balance for one control volume in the gas phase.

Accordingly, the balance equations of the gas phase are:

$$\frac{\partial M_{w,g}}{\partial t} + \frac{\partial \dot{M}_{w,g}}{\partial \xi} = \frac{\partial \dot{M}_{pg}}{\partial \xi}, \tag{3.23}$$

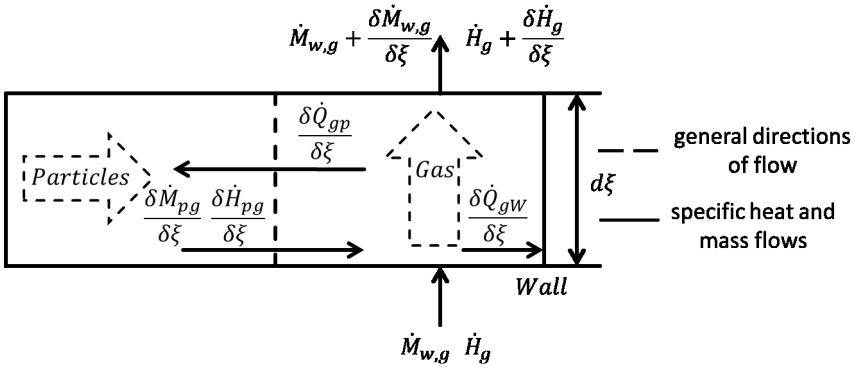

Figure 3.5: Scheme of heat and mass transfer in a control volume of the gas phase.

$$\frac{\partial H_g}{\partial t} + \frac{\partial \dot{H}_g}{\partial \xi} = \frac{\partial \dot{H}_{pg}}{\partial \xi} - \frac{\partial \dot{Q}_{gp}}{\partial \xi} - \frac{\partial \dot{Q}_{gW}}{\partial \xi}, \tag{3.24}$$

where ξ, namely the dimensionless spatial coordinate, is the ratio of spatial coordinate $\tilde{z}$ to the fluidized bed height $\tilde{H}_b$:

$$\xi = \frac{\tilde{z}}{\tilde{H}_b}. \tag{3.25}$$

Besides, the temperature of gas ϑ_g can be obtained based on the gas enthalpy H_g:

$$H_g = M_g \left(c_g \vartheta_g + Y_g \left(c_v \vartheta_g + \Delta h_v \right) \right). \tag{3.26}$$

where the absolute gas humidity Y_g is defined as:

$$Y_g = \frac{M_{w,g}}{M_g}, \tag{3.27}$$

and the total mass of dry gas M_g in the fluidized bed is

$$M_g = \psi_b \rho_g A_{app,c} \tilde{H}_b. \tag{3.28}$$

3.2.2.4 Balance equations of wall

In this study, only the heat balance of the wall is considered, since the material of the wall is water non-absorbent. The wall is assumed to have everywhere the same temperature, and thus the following energy balance is obtained:

$$\tilde{C}_W \frac{d\vartheta_W}{dt} = \dot{Q}_{pW} + \dot{Q}_{gW} - \dot{Q}_{We}. \tag{3.29}$$

In Eq. 3.29, the heat transfer kinetics that can affect the wall are expressed with the following formulas:

$$\dot{Q}_{pW} = \alpha_{pW} A_W (\vartheta_p - \vartheta_W), \tag{3.30}$$

$$\dot{Q}_{gW} = \alpha_{gW} A_W (\vartheta_g - \vartheta_W), \tag{3.31}$$

$$\dot{Q}_{We} = \alpha_{We} A_W (\vartheta_W - \vartheta_e). \tag{3.32}$$

The correlations for each heat transfer coefficient (α_{pW}, α_{gW} and α_{We}) are specified by Martin (2010), Baskakov et al. (1973) and Churchill and Chu (1975), respectively.

3.2.2.5 Hydrodynamic parameters of fluidized bed

Several important hydrodynamic parameters of the fluidized bed (e.g., the aforementioned fluidized bed height $\tilde{H}_b$) appear in the model and need to be further specified.

The fluidized bed height $\tilde{H}_b$ can be calculated from:

$$\tilde{H}_b = \frac{M_{b,tot}}{\rho_p A_{app,c} (1 - \psi_b)}, \tag{3.33}$$

where $M_{b,tot}$ is total holdup of the bed, ψ_b is the porosity due to bed expansion, and $A_{app,c}$ is the cross-sectional area of the apparatus. The bed porosity ψ_b is calculated following Martin (2010),

$$\psi_b = \begin{cases} \psi_{mf} & Re \leq Re_{mf}, \\ (\dfrac{Re}{Re_{elu}})^m & Re_{mf} < Re < Re_{elu}, \\ 1 & Re \geq Re_{elu}. \end{cases} \tag{3.34}$$

The Reynolds number is defined as

$$Re = \frac{u_g d_p}{\nu_g}, \tag{3.35}$$

with the superficial gas velocity

$$u_g = \frac{\dot{M}_g}{\rho_g A_{app,c}} \tag{3.36}$$

and the exponent

$$m = \frac{ln\psi_{mf}}{ln(Re_{mf}/Re_{elu})}. \tag{3.37}$$

The Reynolds number at minimum fluidization velocity can be obtained according to Martin (2010):

$$Re_{mf} = 42.9(1-\psi_{mf})\left(\sqrt{1+\frac{\psi_{mf}^3}{(1-\psi_{mf})^2}\frac{Ar}{3214}}-1\right). \tag{3.38}$$

The Archimedes number is defined as

$$Ar = \frac{g d_p^3(\rho_{p,wet}-\rho_g)}{{\nu_g}^2\rho_g}, \tag{3.39}$$

where the density of the wet particle $\rho_{p,wet}$ is defined as:

$$\rho_{p,wet} = \rho_p(1+X_p). \tag{3.40}$$

Moreover, the Reynolds number at elutriation point Re_{elu} is calculated as proposed by Reh (1977):

$$Re_{elu} = \sqrt{\frac{4Ar}{3}}. \tag{3.41}$$

3.3 Experiments

Our group has conducted both drying and RTD experiments with wet particles (more details of these experiments will be presented in the PhD thesis of Bachmann (in preparation)), and this experimental data have been further analyzed, discussed, and selected as the benchmarks for validating the models in the present work. Here, the key information regarding the experiment settings, experimental procedures, as well as some important results from the post-processing of the experimental data are briefly introduced.

3.3.1 Experimental apparatus and material

The same horizontal fluidized bed, the Glatt GF/Procell 20, which has been used for the RTD experiments in Chapter 2, was again applied for this experiment series. Likewise, the 1.8 mm mono-sized γ-Al_2O_3 particles (Sasol GmbH, properties see Table 2.1) were also selected as experimental material. These particles have some further properties besides the characteristics mentioned in Section 2.3.3, which are desirable for drying research, e.g., porous structure and high temperature tolerance.

3.3.2 Experimental series

In total six experiments were conducted by Bachmann. During the experiments, the continuously flowing wet γ-Al_2O_3 particles were dried by the hot process gas in the apparatus. For all experiments, the dry-based mass flow rate of the particles was fixed at 1 kg/min and the superficial gas velocity was set to a constant value of 1.95 m/s (appr. 3.5 times the minimum fluidization velocity). Samples of particles were taken from the inlet and outlet of the apparatus for measuring the moisture content distribution (MCD). Moreover, the RTD data of the wet particles were also obtained through the pulse stimulus-response technique, as specified in Section 2.3.4. The specific varied process parameters are listed in Table 3.1.

Table 3.1: Summary of variable parameters of the drying and RTD experiments of wet particles.

Exp. [−]	Gas inlet temperature [°C]	Baffle gap size [mm]	Outlet weir height [mm]	Number of internal baffles [−]
A	90	-	175	0
B	90	-	95	0
C	90	-	35	0
D	90	6	35	3
E	90	6	95	3
F	75	6	95	3

3.3.3 Moisture content distribution

The same method used to measure the MCD of particles in the work of Peglow et al. (2011, 2008b), who are the first and to our knowledge until now only

authors to have presented respective results, was applied by Bachmann as well. This method is based on a combination of coulometry and nuclear magnetic resonance (NMR). The coulometry can measure single particle moisture content very accurately but slowly, and is therefore used for calibration of the NMR. The NMR is much faster than coulometry, and thus appropriate for serial investigations. In this study, the wet γ-Al_2O_3 sample particles were put into NMR glass test tubes individually, and the NMR frequency decay signal of each particle was measured for 30 seconds. Then, the separately determined calibration curve which is shown in Fig. 3.6 was used for transforming the NMR signal into moisture content for every investigated single particle. The instruments used were Bruker Avance 300 MHz NMR spectrometer for NMR and WDS 400 (Sartorius) for coulometry. For more details about these two measurement methods, see Peglow et al. (2011, 2008b).

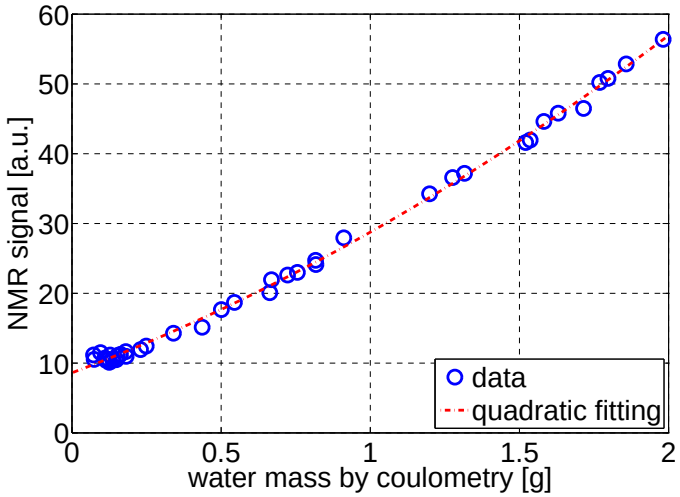

Figure 3.6: Calibration of NMR signal by coulometry.

3.3.4 Experimental results

3.3.4.1 Drying experiments

Figure 3.7 plots the particle MCDs, which were obtained from the samples analyzed by NMR. As can be seen, the MCDs of wet feed particles were not identical, although they were taken from the same container. Besides, the obtained samples at the outlet are dried but with different spread degree of the MCDs.

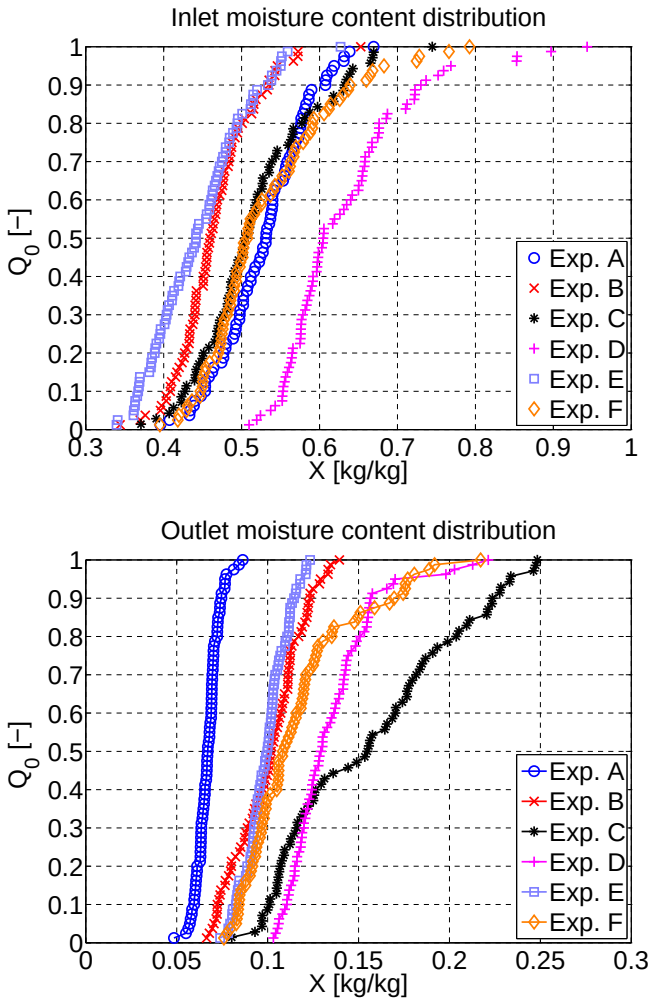

Figure 3.7: Measured particle moisture content distributions of all experiments at the inlet and outlet, respectively.

To further understand the MCD of particles, two characteristics properties, the mean moisture content ($\bar{X}_p$) and the standard deviation (σ) of the MCD, were calculated in this work. The mean moisture content is defined as the ratio of total water content in particles to the total dry-based particle mass:

$$\bar{X}_p = \frac{\Sigma X_{p,m} M_{p,m}}{\Sigma M_{p,m}}. \tag{3.42}$$

The standard deviation of the moisture content distribution is calculated as:

$$\sigma = \sqrt{\frac{\Sigma (X_{p,m} - \bar{X}_p)^2}{N_p}}, \tag{3.43}$$

where N_p is the total number of the particles in each sample.

Table 3.2: Summary of the post-processed parameters of the samples from the drying experiments.

Exp. [−]	$\bar{X}_p$ (inlet) [kg/kg]	σ (inlet) [kg/kg]	$\bar{X}_p$ (outlet) [kg/kg]	σ (outlet) [kg/kg]
A	0.529	0.057	0.067	0.0064
B	0.466	0.051	0.101	0.019
C	0.518	0.076	0.156	0.047
D	0.634	0.084	0.135	0.024
E	0.446	0.061	0.099	0.012
F	0.590	0.072	0.117	0.031

The results are listed in Table 3.2. In every case, the mean moisture content of particles at the outlet is much smaller than the corresponding value at the inlet, which illustrates that the wet particles were significantly dried when passing through the apparatus. Moreover, for all MCDs of the feed particles at the inlet, the standard deviations are significant. These become relatively small at the outlet, due to the fact that the drying rate will decrease with decreasing moisture content of the particle in the second drying period.

3.3.4.2 Residence time experiments

Three important RTD properties, the mean residence time, the standard deviation (square root of the variance of RTD), and the number of theoretical tanks, which have been introduced in Section 2.2, were retrieved from the corresponding RTD data. For each experiment, these RTD-related properties were calculated according to Eq. 2.12, Eq. 2.13, and Eq. 2.7, respectively. The corresponding RTD curves can be found in Fig. 3.8 and the relevant calculation results are listed in Table 3.3.

Hence, based on Table 3.2 and Table 3.3, the influence of fluidized bed internal structure (Table 3.1) on the drying process can be qualitatively analyzed and discussed. From experiments A, B, and C, it can be seen that the particles stay longer in the fluidized bed with increasing the outlet weir height, which could partly explain why the product is much drier when the outlet weir is high. The results from experiments B and E, as well as C and D, show the influence of internal baffles when the outlet weir height is fixed. The number

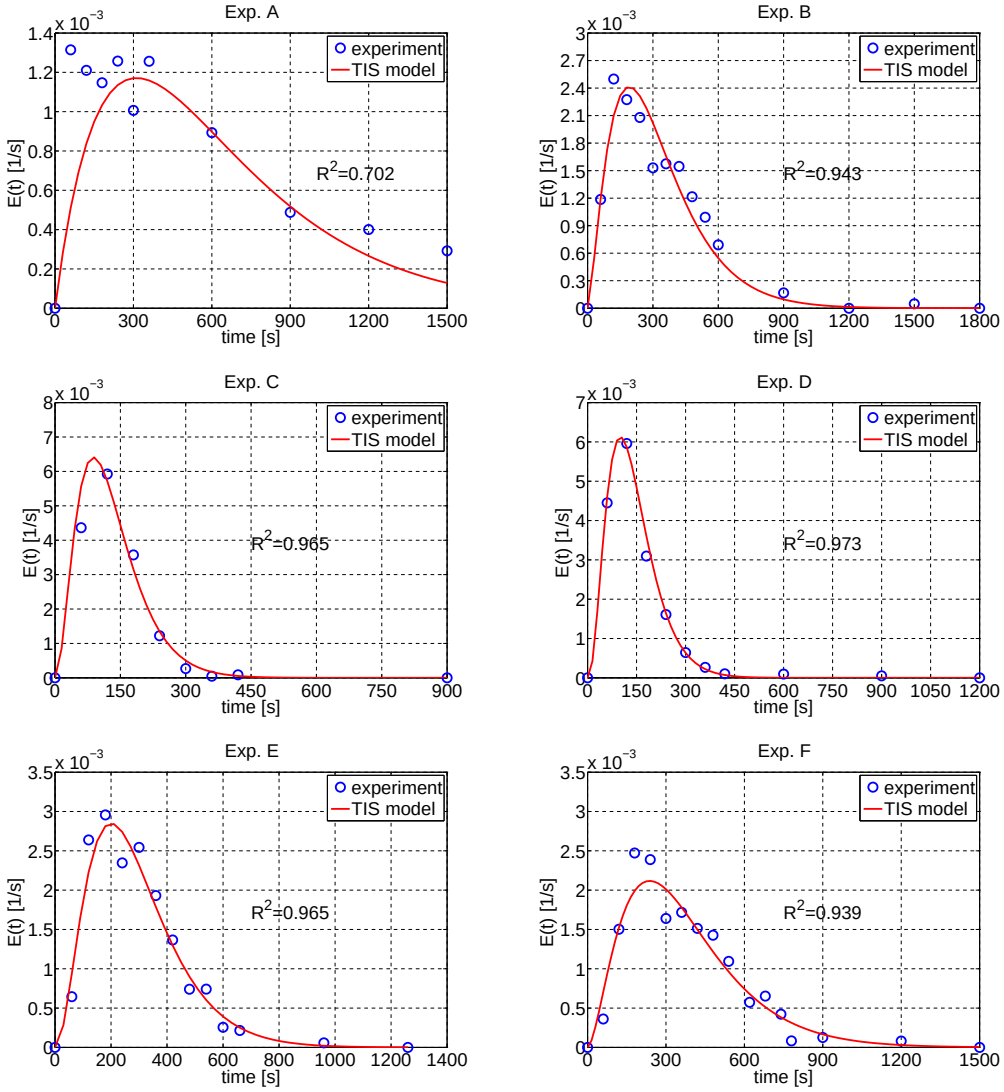

Figure 3.8: Comparison between numerical results from the dispersion model and RTD data from the drying experiments.

Table 3.3: Calculated results based on the RTD data, which were obtained during the drying experiments.

Exp. [−]	mean residence time [s]	standard deviation [s]	number of theoretical tanks [−]	R^2 (vs. Exp.) [−]
A	627.6	445.3	1.98	0.702
B	319.2	202.3	2.49	0.949
C	128.9	72.5	3.16	0.965
D	140.0	74.5	3.54	0.973
E	291.1	162.6	3.20	0.965
F	373.6	225.3	2.75	0.939

of theoretical tanks increases by adding internal baffles, which means that the existence of internal baffles can reduce the dispersion of wet particles in the horizontal fluidized bed. This is in agreement with the results for the dry particles that have been discussed in Section 2.3.5. Accordingly, both mean moisture content and the standard deviation of MCD of the particles at the outlet are smaller after installing internal baffles. Experiments E and F show the effect of processing gas temperature. The results indicate that the number of theoretical tanks increases with increasing the gas temperature. Consequently, the particles would have a higher mean moisture content and broader spread of the MCD at the outlet when the drying capacity of the gas is low.

3.4 Results and discussion

In this section, the results from different horizontal fluidized bed drying models are presented and discussed. Besides, two series of parameter study are also carried out based on the plug flow model and the 2D population balance model. Here, all the governing equations presented in Section 3.2 are implemented by using MATLAB software (Mathworks Inc.) and the integration of all relevant equations was performed through the solver ODE15s.

3.4.1 The plug flow (PF) model

3.4.1.1 Model validation

The plug flow (PF) model is firstly tested. To this purpose, the particle mean moisture content ($\bar{X}_{p,in}$) at the inlet as well as the mean residence time (τ) of particles from the experiments were used in each simulation. The other simulation parameters were also set according to the operating conditions of the experiments. Figure 3.9 shows the simulated particle mean moisture content at the outlet in comparison with the experimental data, and the corresponding values can be found in Table 3.5.

As can be seen from the diagram, four values of the simulated particle mean moisture content (simulations A, B, C, and E) are lower than the measured data, which shows good consistency in terms of the highest conversion rate of the plug flow reactor, as introduced by Levenspiel (1999) as well as Fogler (2006). However, the results from simulations D and F are reversed. In order to figure

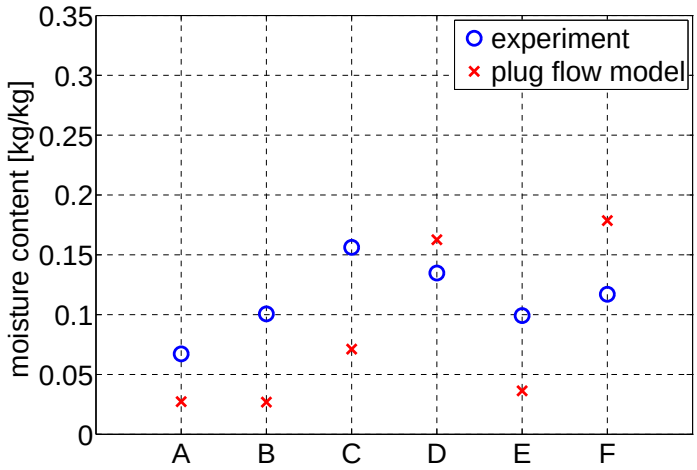

Figure 3.9: Comparison of particle mean moisture content to the simulated by plug flow model with the measured data.

out possible influences, which might cause a relatively high simulated mean moisture content, the measured moisture content distributions at the inlet are further analyzed, as plotted in Fig. 3.10. Through the Box-Whisker-Plot, it is obvious that the inlet samples of experiments D and F have more outliers (single particles with a high moisture content) than the other experiments, which leads to a relatively high mean moisture content at the inlet and might directly cause a higher mean moisture content at the outlet in simulations. In addition, the linkage of the operating conditions to the drying effect of the particles in these two simulations should also be considered. The horizontal fluidized bed was installed with a 35 mm outlet weir in experiment D, which causes a relatively short mean residence time of the particles in the simulation. On the other hand, the particles were dried with the lowest process gas temperature (75 ^oC) in the simulation F, and consequently, the products are the moistest among all simulations. Hence, on the basis of the above facts and considerations, the results from experiments D and F will not be used for model validation in the following sections.

3.4.1.2 Parametric study

Although the simulated particle moisture contents from the plug flow model are lower than the experimental results, the PF model can nevertheless be used

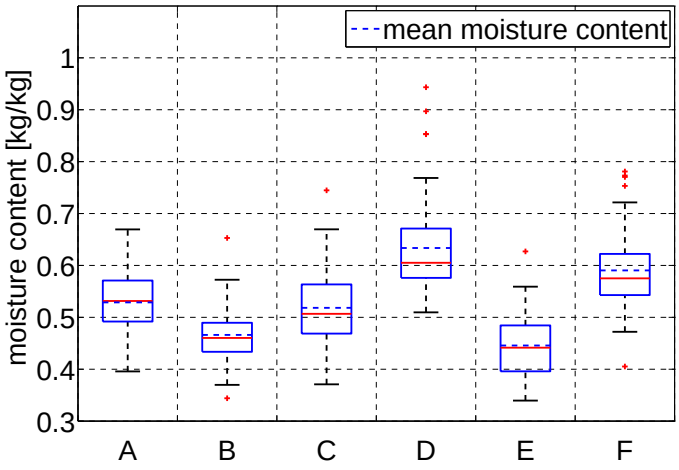

Figure 3.10: Box-Plots of the particle moisture content distribution at the inlet
.

to qualitatively describe the particle drying process from inlet to outlet of a horizontal fluidized bed. Hence, some parametric studies were carried out based on this characteristic. Three process parameters often influence the drying process of particles in a horizontal fluidized bed: process gas temperature (T_g), dry based particle feed rate ($\dot{M}_p$) and superficial gas velocity (u_g). Here, experiment E was selected as the benchmark (BM) for all tests, which means that all parameters corresponded to the process parameters of this experiment in the simulations, except of the tested parameters. The results from three different series of simulations are plotted in Fig. 3.11.

Figure 3.11(a) shows the simulated axial particle moisture content profiles under different process gas temperatures. The particle moisture content decreases linearly along the length of the fluidized bed when the gas temperature is relatively low (60 ^oC). The profiles become nonlinear after increasing the gas temperatures to 90 ^oC and 120 ^oC, respectively. This is due to the fact that temperature increment can increase the drying potential of the process gas, and thus the particles much faster come into the second drying period when moving from the inlet to the outlet.

The influence of particle feed rate is plotted in Fig. 3.11(b). A linear axial profile of particle moisture content can be observed when the solids mass flow rate is high. Such profiles are gradually becoming nonlinear by increasing the feed rate, while the mean residence time is constant for these three simulations

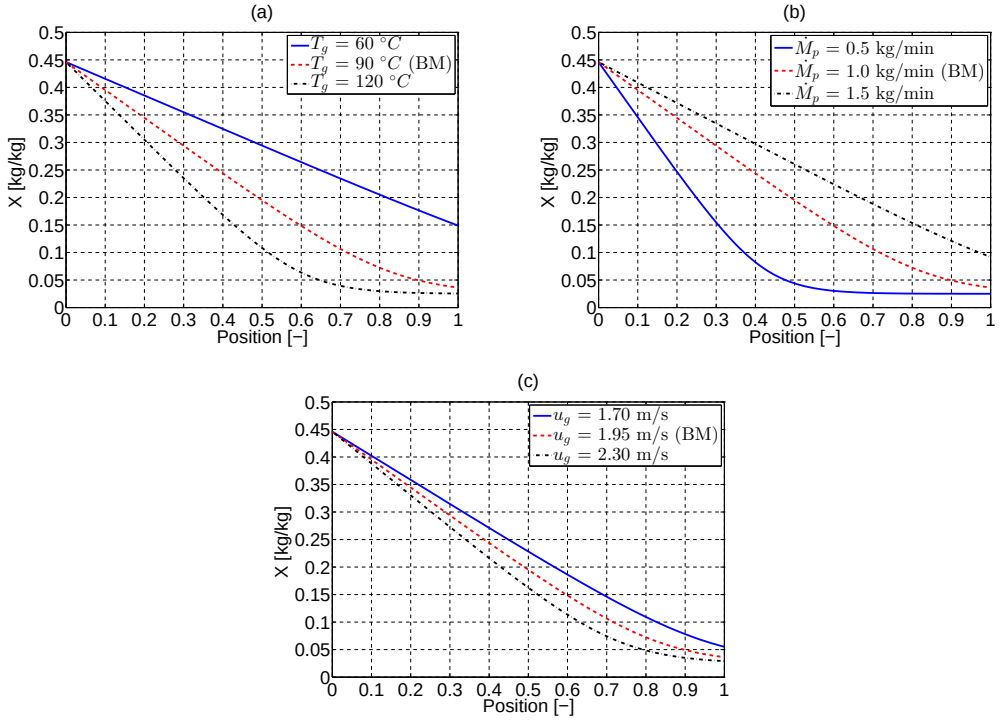

Figure 3.11: Parametric study of the role of three operating parameters, (a) temperature of process gas, (b) particle feed rate, and (c) superficial gas velocity on solid moisture content profile from the inlet (position = 0) to outlet (position = 1).

and a higher feed rate would mean that more particles need to be dried in the bed according to Eq. 3.1.

The last series of simulations are focusing on how the changing of superficial gas velocity would influence the axial profile of particle moisture content. As expected and shown in Fig. 3.11(c), the drying rate increases with increasing the superficial gas velocity.

In general, the particles at the outlet become much drier with increasing process gas temperature, superficial gas velocity, or decreasing solid feed rate. However, it should also be noted that the effect of varying these process parameters on the final product properties is nonlinear as well. For instance, the obtained particle mean moisture contents at the outlet are very close to each other when the process gas temperature is 90 ^oC and 120 ^oC. This means that a parametric optimization of some process parameters can be conducted through the plug flow model.

3.4.2 The mixed flow model

After the discussion of the plug flow model, here we move on to the mixed flow model. For a mixed flow model, in general, the most common and foremost problem is to estimate the number of mixed flow fluidized beds accurately, and hence different approaches have been proposed by different researchers. Baker et al. (2006) divided the horizontal fluidized bed into several isothermal "drying cells" and each "cell" was described as a series of well-mixed fluidized beds. The number of well-mixed fluidized beds was calculated using the formula for the dispersion coefficient from Nilsson and Wimmerstedt (1988). Likewise, Wanjari et al. (2006) derived the number of CSTRs by using the formula for the dispersion coefficient developed by Reay (1978). Nonetheless, as discussed in Chapter 2, these two empirical correlations are of questionable validity for other than their experimental results. It is also common to define the number of well-mixed fluidized beds based on the geometry of the apparatus, e.g., Bertin et al. (2011) presented a model with six CSTRs for their horizontal fluidized bed, which was divided into six processing chambers by five underflow baffles. However, the number of theoretical tanks may differ greatly from the geometric stage number. Bizmark et al. (2010) calculated the number of CSTRs based on an equivalent Damköhler number (Fogler (2006)), defined as the ratio of drying rate to the convective rate of moist product at the inlet of the dryer. However, this method was only validated for a paddy dryer.

In the present study, unlike the methods mentioned above in literature, the calculated number of theoretical tanks based on the TIS model was directly applied. Here, as has been discussed in Section 2.3.6.1, the non-integer tank number is likewise used as well. For instance, when the tank number equals to 2.5, the horizontal fluidized bed would be simulated as three well-mixed fluidized beds, and the total volume of these three tanks would equal to the volume of the whole process chamber of the apparatus. These three tanks are connected in series in the simulation, and the first two tanks would have identical size and operation parameters. Nevertheless, the volume of the third tank would only be half of the first two tanks. Accordingly, several essential process parameters, e.g., particle mean residence time, is also only half in the third tank when compared with the other two tanks. Therefore, this model is also named as tank-in-series mixed flow (TISMF) model in this work.

Figure 3.12(a) plots the simulation results of the TISMF model, together with

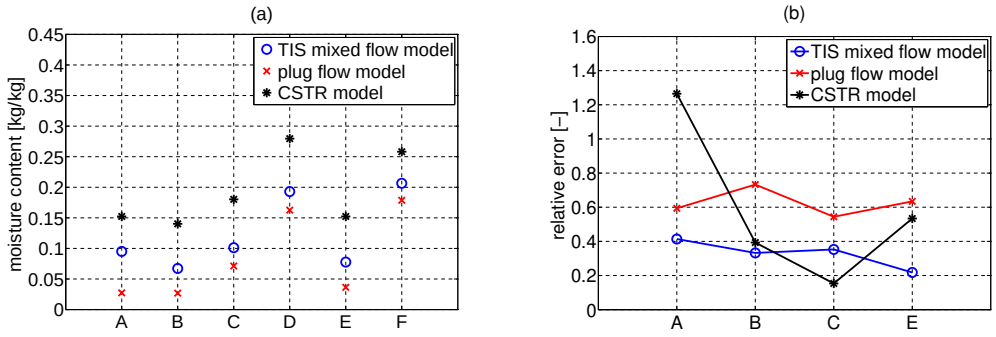

Figure 3.12: A comparison of simulation results from three different horizontal fluidized bed drying models: (a) mean moisture content of particles at the outlet; (b) relative error of the mean moisture content based on the experimental data.

the results from the PF model and the CSTR model (i.e., the TISMF model when the tank number is unity). All simulated mean moisture contents are listed in Table 3.5 as well. As discussed above, the results from the PF model still can represent the lower limit (the driest case) of all drying simulations. On the contrary, the upper limit (the moistest case) of simulated particle mean moisture contents is always obtained from the CSTR model, which also is in line with the theories from Levenspiel (1999) and Fogler (2006). Consequently, all simulation results of the TISMF model locate within the limits, which looks quite reasonable. Moreover, based on the experimental data, the relative error of each simulation result is calculated with:

$$\delta = \frac{|\bar{X}_{p,sim} - \bar{X}_{p,exp}|}{\bar{X}_{p,exp}}, \tag{3.44}$$

and the results are plotted in Fig. 3.12(b) and summarized in Table 3.6. As can be observed, the results from the TISMF model are the most stable and have the lowest average relative error ($\bar{\delta} = 0.382$), when compared with the other two models (PF model ($\bar{\delta} = 0.584$) and CSTR model ($\bar{\delta} = 0.721$)). In general, the presented TISMF model seems to be much more precise than the PF model and the CSTR model in terms of mean moisture content.

3.4.3 The back-mixing flow model

The PF model, CSTR model, and TISMF model are more likely to focus on particle mean moisture content. Nevertheless, the variance of the MCD is also

a critical feature of the dried product. Hence, the simulation results from two back-mixing flow models, which combine the single particle drying model with population balances, are going to be discussed in the following sections.

3.4.3.1 One-dimensional population balance drying (1D-PBD) model

The RTD of particles is implemented as the only dimension in the 1D-PBM model. Here, the experimental RTD curves were reproduced by the TIS model. However, the continuous coordinate of residence time must be divided into finite classes, and the quality of the produced RTD curve is highly dependent on the number of classes (J). Figure 3.13 presents the effect of class number on producing the corresponding RTD curve from experiment A in the modeling, with detailed arithmetic data listed and compared in Table 3.4. On this basis, 50 classes of residence time seem to be a reasonable compromise between accuracy and computational effort. Since Exp. A has the longest mean residence time, 50 classes have also been selected for all the other simulations in this study.

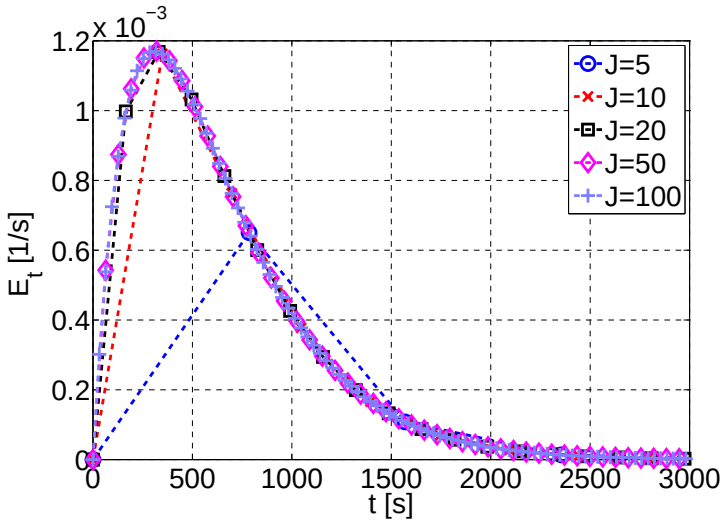

Figure 3.13: RTD curve of Exp. A discretized in different numbers of classes.

Simulation results are plotted together with measured data in Fig. 3.14. As can be seen from Table 3.5 and Table 3.6, the simulated mean moisture contents are in general quite close to the measured data with an average relative error of 0.2, which is even smaller than the corresponding value of TISMF model. However, the obtained mean moisture content from simulation A shows a relatively big difference compared with the experimental results.

Table 3.4: Influence of the number of classes on the simulated RTD curve.

class number J -	mean residence time s	relative error %
5	560.2	39.39
10	621.8	9.95
20	625.5	2.42
50	625.7	0.42
100	625.7	0.14

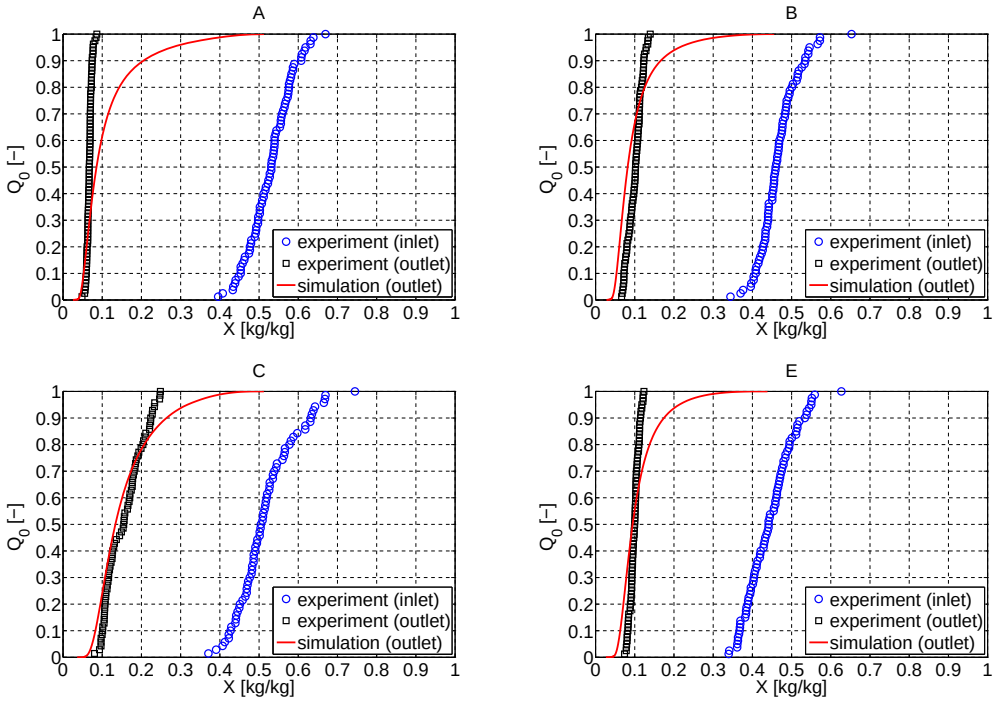

Figure 3.14: Particle moisture content distributions at the outlet, simulated by the 1D population balance model and compared with the measured data.

One explanation might be that the RTD curve used in simulation A is relatively inaccurate, as presented in Table 3.3. Besides, it is also evident that the spread of particle MCDs from the 1D-PBD model simulation is much larger than the spread of experimental data. 1D population balance results published by Peglow et al. (2011) indicate the same kind of misfit. It is due to the fact that all particles are assumed to have the same moisture content at the inlet in the 1D model. The outlet particle moisture content is distributed, but its distribution is assumed to depend only on the density function of the RTD (some particles leave the apparatus quickly, whereas some others stay longer).

3.4.3.2 Two-dimensional population balance drying (2D-PBD) model

As the 1D-PBD model has apparent limitations, 2D simulations were conducted as well. In the 2D model, a second dimension based on the moisture content of the particles was implemented. The solids are divided into several classes according to the moisture content distribution and residence time distribution through discretization. Accordingly, the particles with identical moisture content and residence time are regarded as belonging to one class. For one specified class, the single particle moisture content $X_{p,i,m}$ can be represented by the average moisture content of this class $\bar{X}_{p,i,m}$, which is defined as the ratio of liquid mass on particles $M_{w,i,m}$ to total particle dry mass $M_{p,i,m}$,

$$X_{p,i,m} = \bar{X}_{p,i,m} = \frac{M_{w,i,m}}{M_{p,i,m}}. \tag{3.45}$$

For all 2D simulations, both the obtained residence time distribution and the relevant inlet particle moisture content distribution from the experiment were used. The inlet, as well as the simulated outlet particle MCD, are compared to corresponding experimental data in Fig. 3.15. The calculated mean moisture contents and standard deviations can be found in Table 3.5. By definition, the inlet MCDs are the same as in the measured data. The mean moisture contents at the outlet are the same or quite close to the results from the 1D model, which agreed well with the experimental data. Moreover, in contrast with the 1D model, the most significant improvement attained by the 2D simulation is that the standard deviations of the predicted outlet MCDs are much closer to the experimental ones. It can thus be said that the presented 2D model seems to be much more precise than the 1D model in terms of moisture distribution

spread.

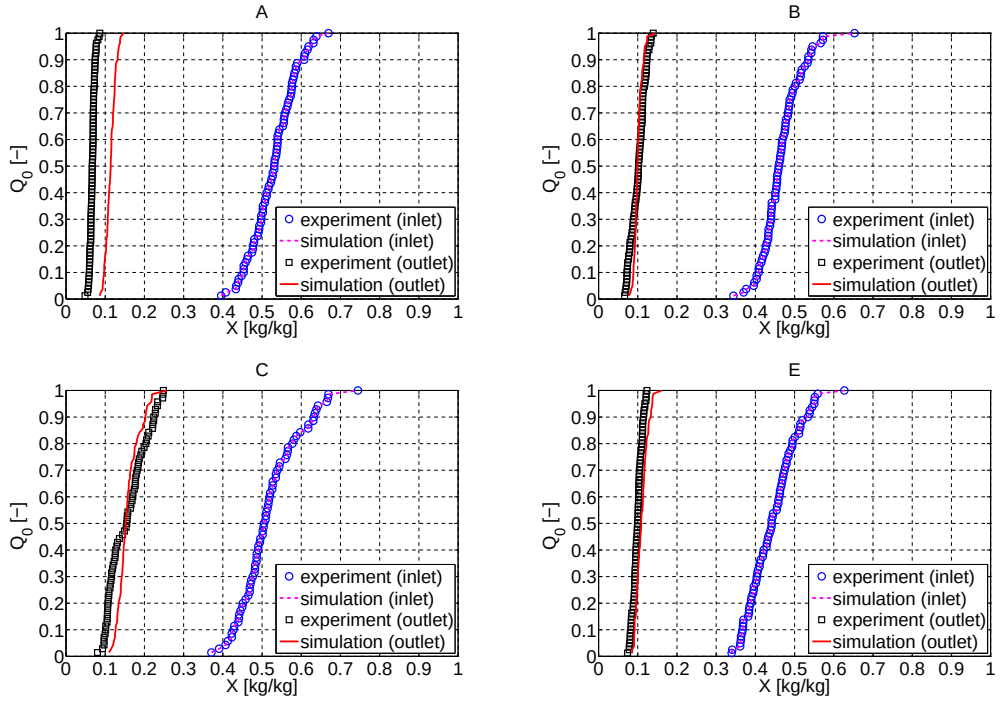

Figure 3.15: Comparison of particle moisture content distributions simulated by the 2D model with measured data.

Table 3.5: Summary of the simulation results about particle moisture content at the outlet from different models.

Sim.	PF	CSTR	TISMF	1D-PBD		2D-PBD	
	$\bar{X}_p$	$\bar{X}_p$	$\bar{X}_p$	$\bar{X}_p$	σ	$\bar{X}_p$	σ
[–]	[kg/kg]	[kg/kg]	[kg/kg]	[kg/kg]	[kg/kg]	[kg/kg]	[kg/kg]
A	0.0273	0.152	0.0950	0.113	0.0788	0.113	0.0126
B	0.0269	0.140	0.0672	0.100	0.0572	0.100	0.0108
C	0.0712	0.180	0.101	0.157	0.0773	0.157	0.0286
D	0.163	0.280	0.193	0.224	0.109	0.224	0.0465
E	0.0363	0.152	0.0776	0.110	0.0520	0.110	0.0150
F	0.179	0.258	0.207	0.226	0.112	0.226	0.0392

3.4.3.3 Parametric study

After model validation, some parametric studies with back-mixing were conducted based on the 2D model. The three process parameters, process gas temperature (T_g), dry based particle feed rate ($\dot{M}_p$) and superficial gas velocity

Table 3.6: Summary of the relative error of the simulated mean outlet moisture content of particles based on the experimental data from different models.

	Relative error $\delta[-]$ (on the basis of experimental data)				
Model	PF	CSTR	TISMF	1D-PBD	2D-PBD
A	0.594	1.265	0.414	0.682	0.682
B	0.733	0.393	0.332	0.006	0.006
C	0.544	0.154	0.353	0.005	0.005
E	0.634	0.534	0.218	0.108	0.108
$\bar{\delta}$	0.626	0.586	0.329	0.200	0.200

(u_g), which have been applied in the parametric study of the plug flow model, were likewise chosen as the parameters to be tested here. Besides, the results of simulation E were again selected as the benchmark (BM). The outlet particle moisture content distributions from three different sets of simulations are presented in Fig. 3.16 and discussed in the following.

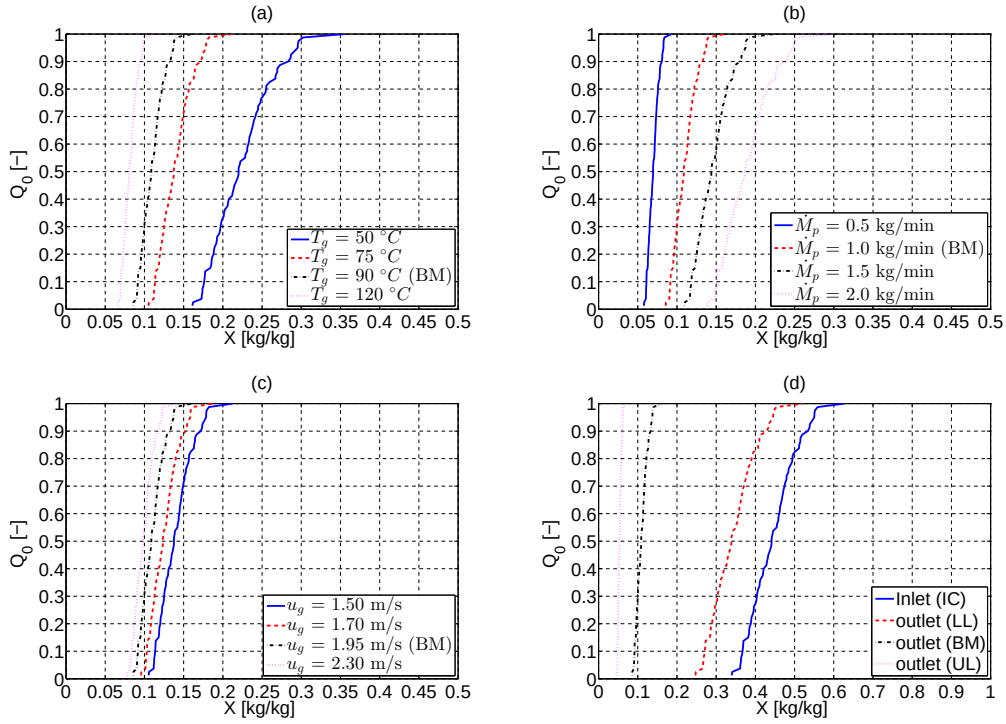

Figure 3.16: The influence of three process parameters (a) temperature of process gas; (b) particle feed rate; (c) superficial gas velocity on outlet particle moisture content distribution and (d) extreme cases of the parametric study.

The influence of changing process gas temperature is shown in Fig. 3.16(a), whereas Table 3.7 lists the calculated saturated gas humidity (drying capacity), particle mean moisture content and the standard deviation of the MCD. Particles are relatively wet and have the broadest spread of the MCD at the outlet when the process gas temperature is 50 ^oC. Particles become much drier, and the spread of the distribution shrinks with increasing gas temperature because the drying capacity of the gas is enhanced. Nevertheless, the influence of gas temperature on the mean value and the standard deviation of outlet particle moisture content is not linear. This could be attributed to two reasons: the drying capacity of the gas does not increase linearly with increasing gas temperature, and particle drying also depends on drying kinetics, especially in the second drying period.

Table 3.7: The influence of the process gas temperature on particle drying.

gas temperature ^{o}C	saturated gas humidity kg/kg	mean moisture content kg/kg	standard deviation kg/kg
50	0.0163	0.225	0.0392
75	0.0238	0.140	0.0213
90 (BM)	0.0284	0.110	0.0150
120	0.0381	0.0817	0.00929

Figure 3.16(b) and Table 3.8 illustrate the influence of particle mass flow rate on the outlet MCD. As can be seen, the simulation with 2.0 kg/min feed rate has the highest mean moisture content and standard deviation, which is due to the fact that this simulation has the highest number of particles in the bed (as the mean residence time is constant for this set of simulations), whereas the drying capacity of the process gas is unchanged. Vice-versa, drier outlet particles and with narrow MCD are obtained by decreasing the feed rate.

Table 3.8: The influence of the particle feed rate on particle drying.

dry feed rate kg/min	mean moisture content kg/kg	standard deviation kg/kg
0.5	0.0702	0.00714
1.0 (BM)	0.110	0.0150
1.5	0.147	0.0227
2.0	0.190	0.0322

Simulation results with different superficial gas velocities are shown in Fig. 3.16(c) and Table 3.9. It is evident that, when the superficial gas velocity is the largest, the corresponding particles are also the driest and the most uniform in their residual moisture. Because the water in the particles is then fastest taken away by the process gas (especially in the first drying period). Vice versa, the mean and the spread of the MCD both raise with decreasing gas velocity. However, the change in superficial gas velocity does not show significant influence on the outlet MCD when compared to the other two tested parameters.

Table 3.9: The influence of the gas flow rate on particle drying.

superficial gas velocity m/s	mean moisture content kg/kg	standard deviation kg/kg
1.50	0.140	0.0214
1.70	0.126	0.0182
1.95(BM)	0.110	0.0150
2.30	0.0994	0.0128

Based on the above, simulations with highest (upper limit) and lowest (lower limit) drying performance, which represent the limiting cases of the parametric study in this work, have been carried out. The respective simulation parameters are listed in Table 3.10 and the results are plotted in Fig. 3.16(d). It can be observed that the conditions of the upper limit have the highest superficial gas velocity, the hottest process gas and the smallest particle feed rate, which results in the driest outlet particles among all simulations in the parametric study. On the contrary, the lower limit conditions lead to particles with the highest mean outlet moisture content as well as the broadest spread of MCD. In general, these two limits indicate the scope of all possible simulation results from the present parameter study.

Table 3.10: Upper and lower limits of the conducted parametric study.

	superficial gas velocity m/s	gas temperature ^{o}C	dry feed rate kg/min
Lower limit (LL)	1.50	50	2.0
Benchmark (BM)	1.95	90	1.0
Upper limit (UL)	2.30	120	0.5

3.5 Conclusion

In this chapter, the drying process of monodispersed γ-Al_2O_3 particles has been studied thoroughly without considering any comminution effect. Several sets of results from particle drying and residence time distribution experiments have been selected as reference data for modeling. Following this experimental data, the effects of operation parameters (height of outlet weir, internal baffles, and process gas temperature) on the RTD and MCD have been qualitatively discussed. Some results are comparable with the conclusions gained with dry particles in Chapter 2 and they are in acceptable agreement. In general, it can be concluded that the influences of internal baffles and outlet weir on the particle RTD are similar for both dry and wet particles.

Based on the definition in literature of different possible flow patterns (ideal and nonideal) in continuous reactors, different assumptions were made for modeling particle movement in a horizontal fluidized bed dryer. Accordingly, on the basis of the principle of single particle drying kinetics, in total five models have been implemented and investigated. From the perspective of mean outlet moisture content of the particles, the PF model and the CSTR model can estimate the upper (driest case) and lower (wettest case) limit values of each drying test. The outlet mean moisture contents from the TISMF model, as well as those from both population balance drying models, agree well with the measured data. Additionally, the change in particle mean moisture content along the axis of the apparatus from inlet to outlet can be qualitatively analyzed by the PF model.

The spread of MCD has also been simulated by considering the distribution of residence time in the real process in the 1D-PBD model. However, the simulation results always show too wide variance of particle MCD at the outlet. We have pointed out that this error is due to the fact that the 1D model does not consider the experimentally observed distribution of particle moisture content in the feed material. Hence, the MCD was implemented as a second dimension of the population balance to the 1D model. The simulation results indicated that the 2D model can much more accurately describe the spread of the residual particle moisture distribution than the 1D model.

After validating the accuracy of the developed models, some parametric studies were conducted based on the plug flow model as well as the 2D-PBD model. The corresponding results show that the particles become much drier

and the MCD becomes narrower by increasing the gas temperature, decreasing the particle feed rate or increasing the superficial gas velocity. However, the effect of changing superficial gas velocity seems to be not so strong as the influences of varying gas temperature or particle feed rate.

Chapter 4

Particle Coating in Horizontal Fluidized Bed

Part of the content of this chapter will be published in a co-authorship paper: Bachmann, P., Chen, K., Bück, A., and Tsotsas, E., Prediction of the particle size and layer thickness distributions in a continuous horizontal fluidized bed coating process.

4.1 Introduction

4.1.1 A review of fluidized bed coating

In addition to the drying purpose of the product, fluidized bed systems are also frequently used for particle enlargement processes, e.g., spray layering (coating/granulation) processes of particle growth. As introduced in Chapter 1, the layering growth process of particulate solids can be operated in batch or continuous mode. Teunou and Poncelet (2002) provided an overview of the state of the art regarding fluidized bed coating technology from the angle of using different apparatus under different operation conditions.

Lots of fundamental and experimental research on batch fluidized bed coaters/granulators can be found in literature. Many researchers (e.g., Jones (1988), Dewettinck and Huyghebaert (1999), as well as Srivastava and Mishra (2010)) classified the batch coating processes into three types according to the configuration of spray nozzles: top-spray, side-spray, and bottom-spray. The top-spray technique is commonly seen in the studies of traditional fluidized bed layering processes (Maa et al. (1996), Hede et al. (2008), Palamanit et al. (2016)). According to Jones (1988), the top-spray process has been successfully applied to the coating of materials with a smallest size of 100 μm. He also

pointed out that the traveling time of a droplet before it can arrive at the particle surface is hard to control in the top-spray coating process since the spray direction is countercurrent to the flow of process gas. Arnaud et al. (1998) experimentally found that the products from the top-spray process usually have irregular shapes and are quite porous, which are two important properties from the standpoint of the quality of the coated product. Nevertheless, Dewettinck and Huyghebaert (1998) experimentally proved that the coating efficiency in top-spray fluidized bed could be improved by appropriately selecting the process parameters. Remarkably, a variety of methods have been developed and applied to analyse the morphology of the coating layer, for example, scanning electron microscopy (Wesdyk et al. (1990)), fluorescence microscopy (Andersson et al. (2000)), confocal laser scanning microscopy (Laksmana et al. (2009)), optical coherence tomography (Koller et al. (2011)), X-ray micro-computed tomography (Sondej et al. (2015)) and so on. Furthermore, in order to intensify the gas-solid mixing, which can favor layering instead of agglomeration during wet particle formulation (Tsotsas et al. (2008)), some unconventional fluidized beds that implement the other two spray technologies have also been developed. The side-spray (also named tangential-spray) configuration often exists in rotary fluidized bed granulators. As investigated by Vuppala et al. (1997)) and Kristensen and Hansen (2006), such combination is an alternative for coating, especially for materials with poor flowability. However, an obvious shortcoming of the fluidized bed rotary granulator is that the scale-up of this technology is difficult to realize (Wong et al. (2013)). Generally, the bottom-spray technology is most commonly adopted in the Wurster fluidized bed coater. This technique was firstly designed for batch-wise operation in the 1960s, as stated by Teunou and Poncelet (2002). In comparison with the top-spray fluidized bed, the bottom-spray system can improve the coating efficiency since the contact between droplets and particles is enhanced. However, the particles are also much wetter and, therefore, more likely to agglomerate, especially when the materials are fine. This problem was solved by the Wurster fluidized bed, which optimizes the drying process by an intensification of particle circulation in the process chamber. A detailed description of the Wurster fluidized bed has been carried out by Christensen and Bertelsen (1997).

The continuous particle layering process was also experimentally investigated by some research groups in the last decade. On the one side, single-stage continuous fluidized bed coaters/granulators were developed by upgrading the

batch fluidized beds (either conventional fluidized bed or Wurster fluidized bed), for instance, see the contributions from Hampel et al. (2013), Schmidt et al. (2015a,b), Hoffmann et al. (2015) and Rieck et al. (2015). On the other side, Bertin et al. (2013) conducted reference granulation experiments for producing urea by using a horizontal fluidized bed.

Generally, no matter whether in batch or continuous fluidized beds, another important and common research focus is the numerical modeling of the particle layering process, because numerical simulation can usually provide approximate solutions of complex problems in a relatively short time, which is entirely meaningful for process control, optimization, and design. Many researchers (e.g., Wnukowski and Setterwall (1989), Dewettinck and Huyghebaert (1998), Heinrich et al. (2002), Vreman et al. (2009), Bück et al. (2015, 2011), Hampel et al. (2013), Hoffmann et al. (2015) and Müller et al. (2019)) have successfully applied the population balance approach, which can follow specific properties of particles (e.g., particle size distribution (PSD)) in the model, to simulate and study the layering process of particles in either batch or single-stage continuous fluidized beds. For these apparatuses, the RTD of particles is not considered as a factor which would influence the quality of the final product. Besides, only few works are available on the modeling of the layering process of particles in a horizontal fluidized bed. Bertin et al. (2013, 2011, 2007) carried out a series of numerical studies based on the population balance model by considering the horizontal fluidized bed as a connection of several process chambers according to the geometry of the apparatus. However, the influence of RTD on the particle growth process is not considered in these works.

4.1.2 Overview

As discussed in Chapter 3, the drying process in a horizontal fluidized bed is influenced by the RTD of particles. Similarly, it can be expected that the RTD will also influence the performance of a horizontal fluidized bed coater. In this chapter, the development of two coating models using the population balance approach is presented. The simulation results are then validated by comparing with reference data from coating experiments. In the end, the influences of some operation parameters on the properties of coated products are further discussed by means of numerical experiments.

Again, experiments have been conducted by Philipp Bachmann and will be

discussed in more detail in his PhD thesis (in preparation), whereas the present author focused on modeling.

4.2 Model development

4.2.1 General hypothesis

In this work, a pure particle coating process is assumed, and the back-mixing theory, which has been successfully used in Chapter 3 for describing particle movement in the horizontal fluidized bed, is applied. Furthermore, several hypotheses are consistent with those of the drying model. In general, the following assumptions are met in advance for establishing both 1D and 2D population balance models.

- The particles are all spherical, and thus their size can be characterized by particle diameter d_p.
- The coating process occurs in the fluidized bed at steady state.
- The core particles are perfectly mixed in vertical direction in the fluidized bed.
- The particles are always dry during the whole coating process, that is, the drying process of the core particle is not considered.
- Only particle coating process happens in the process chamber, which means that the other possible particle size changing processes, e.g., agglomeration, attrition, breakage as well as elutriation, are neglected.
- All solution of sodium benzoate sprayed in the fluidized bed reaches successfully the surface of particles and contributes to the coating of particles, i.e., the drying of solute before it can reach the particles and the formation of nuclei due to overspray is neglected.
- The solution is uniformly sprayed onto the particle surface so that the growth of the coating layer is homogeneous.

4.2.2 One-dimensional population balance coating (1D-PBC) model

For a coating process by means of horizontal fluidized bed, the outlet PSD is expected to be broader when compared with the inlet PSD, which will also be validated on the basis of the experimental results in Section 4.3.3. On the basis of the discussion in last chapter, it can be assumed that the RTD of particles in the horizontal fluidized bed is one of the leading causes of this increase in the spread of PSD. Hence, based on the back-mixing theory, in the 1D model the particle residence time τ is selected as the only property coordinate, and the particles are assumed to be monosized at the inlet.

The population balance equation in terms of mass balance of particles can be expressed as:

$$\frac{\partial(M_p n)}{\partial t} + \frac{\partial(M_p n)}{\partial \tau}\frac{\partial \tau}{\partial t} = \dot{M}_{sol,s} n - \dot{M}_{p,out} n + \dot{M}_{p,in} n. \tag{4.1}$$

As can be seen, Eq. 4.1 looks similar to Eq. 3.9 and only one more term $\dot{M}_{sol,s} n$ is added. Here, $\dot{M}_{sol,s}$ represents the mass spray rate of solids in the solution, which can be calculated with

$$\dot{M}_{sol,s} = \dot{M}_{sol} x; \tag{4.2}$$

n is the particle number density function based on residence time, which can be expressed with Eq. 3.7.

However, unlike drying experiment, the tracer would be coated, and therefore the RTD of particles cannot be directly obtained through RTD measurement during the coating process. Consequently, the RTD of particles is established by combining the dispersion model (Eq. 2.9) with empirical correlations. According to Eq. 2.10 and Eq. 2.11, the dispersion coefficient D can be derived based on the Bodenstein number Bo and mean residence time τ.

For the fluidized bed without any internal baffle, the Bodenstein number Bo_{nb} is calculated from the correlations given by Bachmann et al. (2016),

$$Bo_{nb} = \left(\frac{L_b^2}{W_b \tilde{H}_{weir}}\right)^{\psi_b} \left(\frac{d_p}{d_{bu}\psi_b}\right) \left(\frac{\dot{M}_p}{\dot{M}_g - \dot{M}_{g,mf}}\right)^{0.5} \left(\frac{d_{bu,max}}{d_{bu,in}}\right)^{0.15} \left(\frac{u_{elu}}{u_{mf}}\right)^{0.75}. \tag{4.3}$$

As can be seen, the Bodenstein number depends on many factors and every term needs to be specified.

The geometrical parameters (the length L_b, width W_b, and outlet weir height $\tilde{H}_{weir}$ of the fluidized bed) and some operation parameters (the mass flow rates of particles $\dot{M}_p$ and gas $\dot{M}_g$) can be attained from the experimental setup. The minimum fluidization gas velocity u_{mf} (and the mass flow rate of gas with minimum fluidization velocity $\dot{M}_{g,mf}$), the gas velocity at elutriation point u_{elu} as well as the porosity of the bed ψ_b can be calculated using Eqs. 3.35 to 3.41 in Section 3.2.2.

Based on Mori and Wen (1975), the diameter of bubbles d_{bu} is calculated using:

$$\frac{d_{bu,max} - d_{bu}}{d_{bu,max} - d_{bu,in}} = \exp\left(-0.3\frac{\tilde{H}_{weir}}{W_b}\right), \tag{4.4}$$

where the diameter of inflow bubbles $d_{bu,in}$, which are formed immediately after the gas has passed through the porous gas distributor, is defined as:

$$d_{bu,in} = 0.00376\left(u_g - u_{mf}\right)^2, \tag{4.5}$$

while the maximum bubble diameter $d_{bu,max}$ from coalescence is:

$$d_{bu,max} = 0.652\left(A_{app,c}\left(u_g - u_{mf}\right)\right)^{0.4}; \tag{4.6}$$

(Standard SI is applied in Eqs. 4.4 to 4.6, i.e., u_g and u_{mf} in m/s, d_{bu}, $d_{bu,max}$ and $d_{bu,in}$ in m, $A_{app,c}$ in m^2).

Bachmann et al. (2017) also investigated the Bodenstein number of fluidized beds with different internal baffle configurations. For the underflow configuration, the Bodenstein number Bo_{uf} is:

$$Bo_{uf} = 0.00506 Bo_{nb} N_{baffle}\left(\frac{\tilde{H}_{weir}}{\tilde{H}_{gap}}\right)^{\psi_b} Re_{mf}^{0.75}, \tag{4.7}$$

and for the overflow configuration, the Bodenstein number Bo_{of} is:

$$Bo_{of} = 0.0117 Bo_{nb} N_{baffle}\frac{\tilde{H}_{weir}}{d_p}. \tag{4.8}$$

Same as the Bodenstein number Bo, the mean residence time τ also needs to be derived, and usually it is closely related to the bed mass M_b (Eq. 2.40). A more general approach for estimating bed mass M_b is given by Bachmann

et al. (2017),

$$M_b = (1 - \psi_{ab})\rho_p A_{app,c} \tilde{H}_{weir}, \tag{4.9}$$

where a new term, the apparent bed porosity ψ_{ab} is developed. It is calculated as follows:

$$\psi_{ab} = 1 - \left(1 - \frac{2.7a}{1 + 1.7a}\right)(1 - \psi_{mf}), \tag{4.10}$$

with the dimensionless ratio

$$a = \frac{u_g - u_{mf}}{u_{elu} - u_{mf}}. \tag{4.11}$$

In the next step, the particle growth model needs to be specified, and the approach from Mörl et al. (2007) is applied here. In their work, the increase of the mass of a single particle M_p in an infinitesimal time interval $\mathrm{d}t$ is directly related to the surface area of the particle A_p, which can be expressed as:

$$\frac{\mathrm{d}M_p}{\mathrm{d}t} = \frac{A_p}{A_b}\dot{M}_{sol,s}. \tag{4.12}$$

Here, A_b is the total surface area of all particles in the bed and A_p can be calculated with

$$A_p = \pi d_p^2. \tag{4.13}$$

Moreover, the change of particle volume $\tilde{V}_p$ can be defined in terms of particle diameter d_p

$$\frac{\mathrm{d}\tilde{V}_p}{\mathrm{d}d_p} = \frac{\pi}{2} d_p^2, \tag{4.14}$$

and the density of the shell ρ_{sh} considering the porosity of the coating layer ψ_{sh} can also be derived

$$\rho_{sh} = \frac{\mathrm{d}M_p}{\mathrm{d}\tilde{V}_p} = \rho_{sol,s}(1 - \psi_{sh}). \tag{4.15}$$

Rieck et al. (2015) estimated the dependency of the shell porosity ψ_{sh} on the drying potential $\tilde{\eta}$ for γ-Al_2O_3 particles coated with sodium benzoate with the linear correlation

$$\psi_{sh} = -0.33\tilde{\eta} + 0.45. \tag{4.16}$$

The drying potential $\tilde{\eta}$ depends on the moisture content of the process gas

$$\tilde{\eta} = \frac{Y_{sat} - Y_{out}}{Y_{sat} - Y_{in}}, \tag{4.17}$$

where the adiabatic saturation moisture content Y_{sat} depends on the inlet gas temperature $T_{g,in}$ and inlet moisture content of gas Y_{in}. Besides, for a pure coating process, the gas is assumed to take up all liquid in the spray, and thus the outlet moisture content Y_{out} of the gas is calculated with

$$Y_{out} = \frac{\dot{M}_{sol}\,(1-x)}{\dot{M}_g}. \tag{4.18}$$

In summary, the growth rate of a single particle can be expressed by combining Eqs. 4.12, 4.14 and 4.15, which leads to

$$\frac{\mathrm{d}d_p}{\mathrm{d}t} = \frac{2\dot{M}_{sol,s}}{\rho_{sol,s}(1-\psi_{sh})A_b}. \tag{4.19}$$

It can also be written as

$$\mathrm{d}d_p = \frac{2\dot{M}_{sol,s}}{\rho_{sol,s}(1-\psi_{sh})A_b}\mathrm{d}t, \tag{4.20}$$

which means that the change in particle size is time-dependent, or, in steady state continuous operation, dependent on residence time. Besides, the changing of surface area of particle A_b with residence time can be assumed to be constant since the increase of particle size is relatively small in comparison with the size of the core particle in a coating process. Consequently, for a single particle with initial particle size $d_{p,i,0}$ and residence time τ_i the particle size at the outlet can be calculated by integrating Eq. 4.20 to obtain

$$d_{p,i} = \frac{2\dot{M}_{sol,s}}{\rho_{sol,s}(1-\psi_{sh})A_b}\tau_i + d_{p,i,0}. \tag{4.21}$$

However, the PSD of the coated particles is also strongly depending on the number density of particles at the outlet, which can be obtained by solving Eq. 4.1.

4.2.3 Two-dimensional population balance coating (2D-PBC) model

As it will be presented in Fig. 4.2 and Table 4.2, a distribution of the deviation between particle sizes already exists from the inlet for all experiments. Hence, next to the residence time, the particle size is implemented directly as the second dimension based on the 1D-PBC model. Accordingly, the density function $\hat{n}$ regarding particle size and residence time can be expressed as

$$\hat{n}(\tau, X, t) = \frac{1}{M_b(t)} \frac{\partial^2 M_p(\tau, d_p, t)}{\partial \tau \partial d_p}, \tag{4.22}$$

where M_p represents the mass of all particles having identical residence time τ and diameter d_p. Besides, M_b is the total mass of particles in the fluidized bed at each time point, which is defined as:

$$M_b(t) = \int_0^\infty \int_0^\infty M_p(\tau, d_p, t)\hat{n}(\tau, d_p, t)\mathrm{d}\tau\mathrm{d}d_p. \tag{4.23}$$

Accordingly, the population balance equation based on particle mass balance can be derived as

$$\frac{\partial(M_p\hat{n})}{\partial t} + \frac{\partial(M_p\hat{n})}{\partial \tau}\frac{\partial \tau}{\partial t} + \frac{\partial(M_p\hat{n})}{\partial d_p}\frac{\partial d_p}{\partial t} = \dot{M}_{sol,s}\hat{n} - \dot{M}_{p,out}\hat{n} + \dot{M}_{p,in}\hat{n}. \tag{4.24}$$

The population balance equation can only be solved after discretization, and the particles will be distributed into different classes. Since two properties are considered in the model over the population, each class would differentiate itself in particle size and residence time. Moreover, one single particle can be used to represent all the other particles in the same class, and thus the single particle growth model that depends on residence time and initial particle size can be applied to the 2D-PBC model as well.

4.3 Reference work

With respect to the particle growth process by means of continuous fluidized bed, Bachmann et al. (in preparation) have conducted and evaluated several continuous granule coating experiments by using the horizontal fluidized bed. More details regarding the experiments will be included in the upcoming PhD thesis of Bachmann. These experimental results are used for testing the performance of the developed coating models in the present work. Hence, some

brief information on this reference work as well as some general discussion on the basis of the post-processed data are introduced in this section.

4.3.1 Experimental plant

In the work of Bachmann et al. (in preparation), the same pilot scale horizontal fluidized bed (Glatt GF/Procell 20) which has also been utilized for all other reference experimental works mentioned in Chapters 2 and 3 was applied for performing the coating experiments. Four external mix two-fluid nozzles with liquid orifices of 2.3 mm were installed in the apparatus for spraying of the coating solution. In order to better describe the position of spray nozzles, Fig. 4.1 shows the scheme of the modified underflow horizontal fluidized bed with spray nozzles. As can be seen, the process chamber was divided into four equal-sized compartments by three internal baffles, and the nozzles were installed at the center of the air distributor of every compartment in order to realize a bottom-spray coating process.

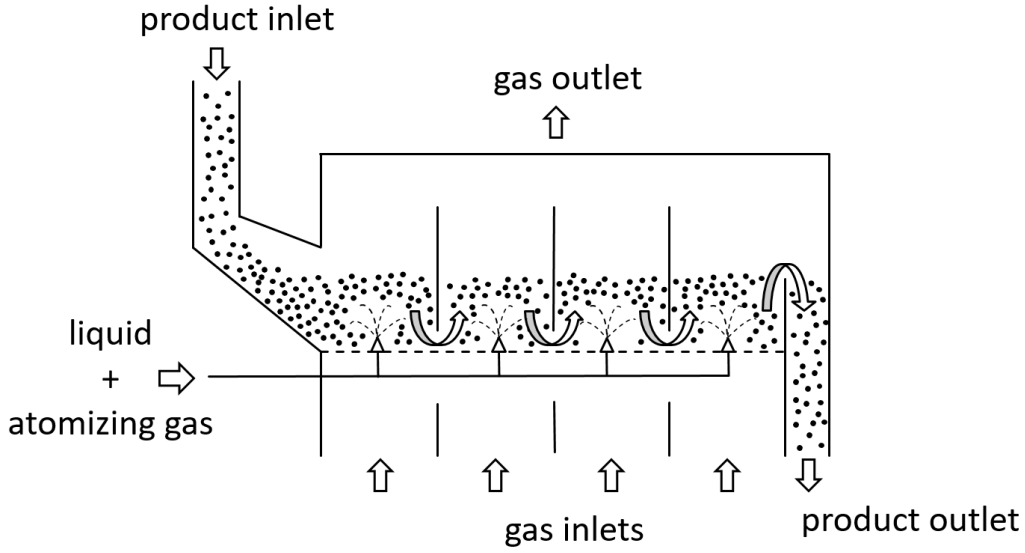

Figure 4.1: Scheme of the underflow horizontal fluidized bed installed with four two-fluid spray nozzles (experiment No. 3 in the work of Bachmann et al. (in preparation)).

4.3.2 Experimental series

A series of four coating experiments were conducted by Bachmann. The 1.8 mm γ-Al_2O_3 particles (Sasol GmbH, properties see Table 2.1), which have

been also applied in the RTD and drying experiments before, were used here as the core particles and 30 m% solution of sodium benzoate was selected as the coating material. The specific operation parameters are listed in Table. 4.1. As can be seen, several operation parameters stayed unchanged for all experiments, for instance, the process gas temperature T_g, the superficial gas velocity u_g, the mass flow rate of particles $\dot{M}_p$ and the spraying mass flow rate of solution $\dot{M}_{sol}$. On the other hand, the height of outlet weir $\tilde{H}_{weir}$, the existence (no internal baffle ($N_{baffle} = 0$)) as well as the way of installation of internal baffles (underflow (Exp. No. 3, $\tilde{H}_{gap} = 6\ mm$) and overflow (Exp. No. 4, $\tilde{H}_{gap} = 0\ mm$)) were selected as variable parameters, because these parameters can directly influence the transportation (RTD) of particles.

Table 4.1: Summary of all essential operation parameters of the coating experiments conducted by Bachmann.

Exp. No. [−]	T_g [°C]	u_g [ms^{-1}]	$\dot{M}_p$ [kgmin^{-1}]	$\dot{M}_{sol}$ [kgmin^{-1}]	$\tilde{H}_{weir}$ [mm]	N_{baffle} [−]	$\tilde{H}_{gap}$ [mm]
1	85	1.95	1	0.5	95	0	-
2	85	1.95	1	0.5	175	0	-
3	85	1.95	1	0.5	175	3	6
4	85	1.95	1	0.5	175	3	0

At the onset of every experiment, the particles were continuously fed into the fluidized bed with a constant mass flow rate. When a steady state had been established in the fluidized bed (particle inflow rate equals to outflow rate), spraying started. The solution of sodium benzoate was dosed into the plant by nozzles using one peristaltic pump (Petro Gas Ausrüstungen Berlin GmbH, model: G2504.4-KVF/215) and the atomizing gas was directly supplied from the local compressed air network. When five times the mean residence time had elapsed after the fluidized bed had reached the steady state, a sample was collected at the outlet and then the experiment was terminated.

Later, Bachmann analyzed the samples offline with two different methods for obtaining the particle size distributions (PSDs). One hundred particles were firstly manually picked out from each sample, and the mean diameter of each particle was measured utilizing an optical microscope. As the sodium benzoate can easily dissolve in water, these one hundred particles were soaked in pure water for 24 hours and afterward dried in the oven (105 °C, 20 $mbar$) for another 24 hours. The washed particles were again observed under the

microscope, and accordingly, the PSDs of the core particles were obtained. The PSD of the rest of the coated particles in each sample was subsequently determined by using a camera-optical particle size analyze system (Camsizer, Retsch GmbH, Germany). Then the particles were washed and dried in the same way as before, and the corresponding PSD of the washed particles was measured as well.

4.3.3 Experimental data

Figure 4.2 displays the measured inlet (washed) and outlet (coated) PSDs of all coating experiments. Based on these distributions, several characteristic features of the PSD can be obtained. The median diameter $d_{p,median}$ can be directly read from the corresponding normalized cumulative curve of PSD ($Q_0(d_p)$). Besides, the mean diameter $d_{p,mean}$ and standard deviation σ can also be calculated based on the method of moments:

$$d_{p,mean} = \int d_p \mathrm{d}Q_0\left(d_p\right), \tag{4.25}$$

$$\sigma = \left(\int \left(d_p - d_{p,mean}\right)^2 \mathrm{d}Q_0\left(d_p\right)\right)^{1/2}. \tag{4.26}$$

The attained median diameters, mean diameters, and standard deviations of the inlet and outlet PSDs are summarized in Table 4.2. As can be seen, for all experiments, the median diameter, mean diameter, as well as standard size deviation of the final product, are higher than the corresponding values of the feed particles, and this can explain the general trend in Fig. 4.2, which is that, regardless of the PSD measurement method, all distributions of coated particles (the dotted lines) shift to the right and are broader in comparison with the distributions of the core particles (the solid lines). It should also be noted that the standard deviation of the PSD from the Camsizer is much higher than the corresponding value from the microscope, which is probably due to the fact that all particles analyzed by the microscope were manually selected under pseudo-random conditions. Additionally, although the physical properties in Table 2.1 indicate that the average diameter of γ-Al_2O_3 particles is 1.8 mm, there is still some difference between the measured mean particle diameters of the samples and the nominal value, which should also be considered in the simulations. All in all, to summarize these reference coating experiments, it can be concluded that sodium benzoate has been successfully coated on the γ-Al_2O_3

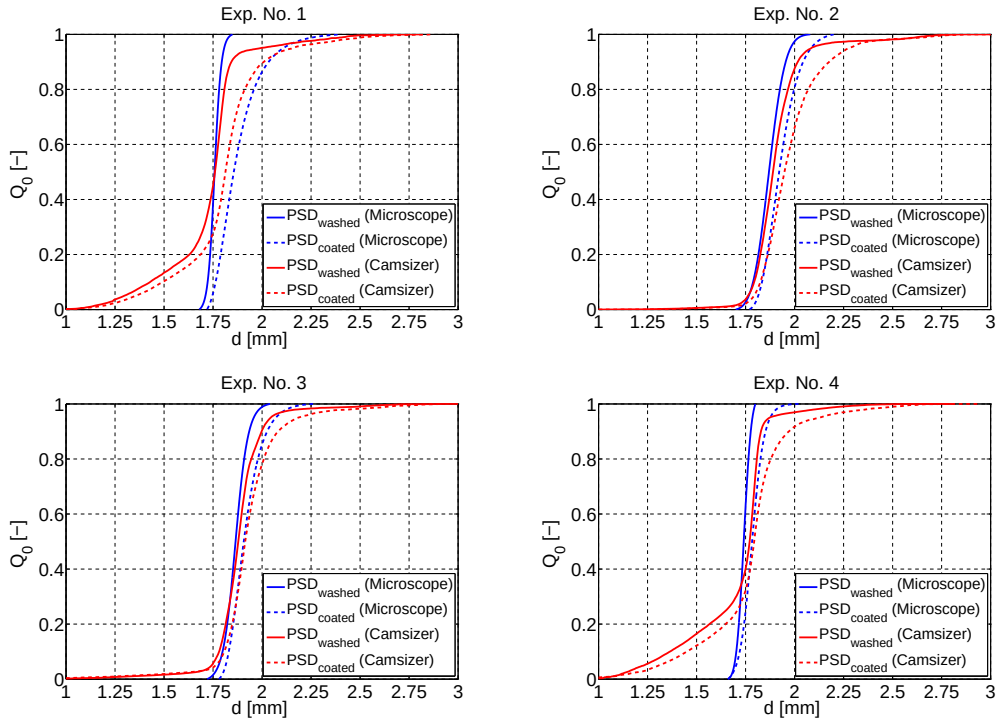

Figure 4.2: Depiction of normalized cumulative particle size distributions from the experiments, obtained by means of two different measurement methods.

particles in each test, and the data can be used for the further validation of models.

4.4 Simulation, results, and discussion

4.4.1 Pre-simulation

As discussed above, for both 1D- and 2D-PBC models, the simulation results are directly influenced by the RTD of particles, which can be determined by the Bodenstein number Bo and mean residence time τ. Regarding the Bodenstein number Bo, it has been proved that it can be well estimated by using the correlations from Bachmann et al. (2016, 2017) when the outlet weir is high (see Section 2.3.6), and the lowest outlet weir height is with 95 mm high enough in all coating experiments. Hence, only the correlations of bed mass (Eqs. 4.9 to 4.11) were tested here based on RTD data from RTD experiments (Section 2.3) and drying experiments (Section 3.3). For all drying experiments, the average density of wet particles between inlet and outlet was used in Eq. 4.9:

Table 4.2: A summary of the median diameter, mean diameter and standard deviation of the inlet PSDs (washed) and the outlet PSDs (coated) based on the experimental data.

	Microscope					
	washed			coated		
Exp. No.	$d_{p,median}$ [mm]	$d_{p,mean}$ [mm]	σ [mm]	$d_{p,median}$ [mm]	$d_{p,mean}$ [mm]	σ [mm]
1	1.76	1.76	0.028	1.86	1.88	0.114
2	1.86	1.87	0.064	1.92	1.93	0.081
3	1.86	1.87	0.054	1.91	1.92	0.079
4	1.74	1.74	0.028	1.78	1.79	0.052
	Camsizer					
	washed			coated		
Exp. No.	$d_{p,median}$ [mm]	$d_{p,mean}$ [mm]	σ [mm]	$d_{p,median}$ [mm]	$d_{p,mean}$ [mm]	σ [mm]
1	1.760	1.720	0.211	1.814	1.798	0.233
2	1.891	1.907	0.147	1.947	1.978	0.169
3	1.878	1.882	0.145	1.911	1.931	0.183
4	1.771	1.697	0.212	1.793	1.765	0.239

$$\rho_{p,wet} = \rho_p \left(1 + \frac{\bar{X}_{p,in} + \bar{X}_{p,out}}{2}\right). \tag{4.27}$$

The calculated values of bed mass are respectively plotted against the experimental data in Fig. 4.3. As can be seen, no matter whether the particles are wet or dry in the fluidized bed, all the calculated bed masses agree with the experimental values satisfactorily. Hence, based on the results of validating Bodenstein number Bo and bed mass M_b, it may be concluded that the way of predicting the RTD of particles in the coating process is feasible.

4.4.2 Model validation

Two series of simulations were carried out to compare the developed particle coating models with the experimental data. The measured data from the microscope and the Camsizer are used as initial conditions respectively. Therefore, each series consists of eight simulations (four 1D simulations and four 2D simulations). The mean diameter of washed particles was selected as the initial value in the 1D simulation. On the other hand, for the 2D-PBC model, the normalized cumulative particle size distribution of the washed particles was firstly

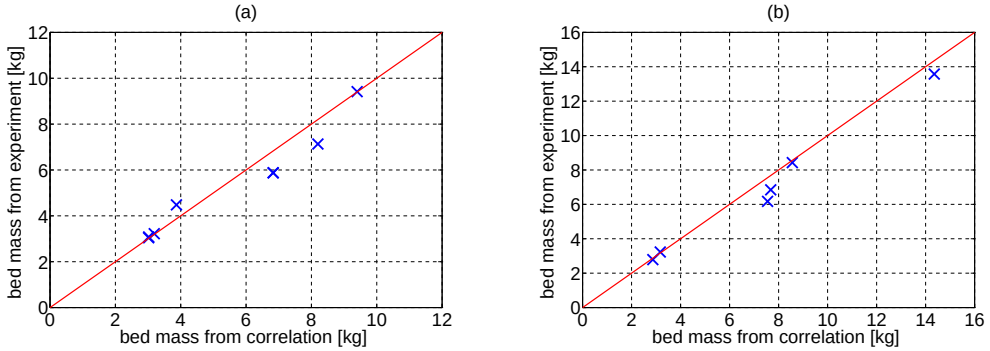

Figure 4.3: Comparison of calculated bed masses with (a) the bed masses of dry particles (RTD experiments) and (b) the bed masses of wet particles (drying experiments).

approximated using a linear interpolation method and thereafter converted into particle number density distribution in the simulation. Furthermore, as discussed in Section 3.4.3, the coordinate of particle residence time distribution was also discretized into finite classes in both 1D and 2D simulations. Other simulation parameters were set according to Table 4.1. Both models were solved by means of the ode15s solver in MATLAB software (Mathworks Inc.), using for solving the population balance equations.

The simulated normalized cumulative PSDs from both simulation series are plotted with the experimental data in Fig. 4.4 and Fig. 4.5, respectively. As can be seen, no matter whether the 1D or the 2D model is used, all the simulation results can reflect a distribution of coated particles at the outlet. Table 4.3 presents the calculated median diameter, mean diameter as well as the standard deviation of the corresponding simulated PSDs. It is evident that the simulated mean diameters from the 1D model are mostly the same as those from the 2D model. Besides, the median diameters of particles from both models are quite close to each other when the spread of the PSD is relatively small. However, when the initial particle size has a relatively broad distribution (e.g., for simulations Ser. 2 No. 1 and Ser. 2 No. 4), the simulated median diameter of particles will differ from the 1D to the 2D model. The effect of the spread of initial PSD can be figured out by comparing the obtained standard deviations from different models in each series. In most instances, the spread of simulated PSD from the 2D model is larger than the spread of the corresponding distribution from the 1D model. However this trend does not remain fixed; for instance, the results of simulation Ser.1 No. 1 indicate

that the standard deviation of the PSD from the 2D model can also be smaller than the corresponding value from the 1D model, and this will be further discussed in the parameter study later on. In general, the difference between the standard deviations from 1D and 2D models is not that obvious when the PSD at the inlet is narrow (e.g., PSDs from the microscope). Whereas, this difference becomes much more significant when the initial PSD becomes wider (e.g., PSDs from the Camsizer).

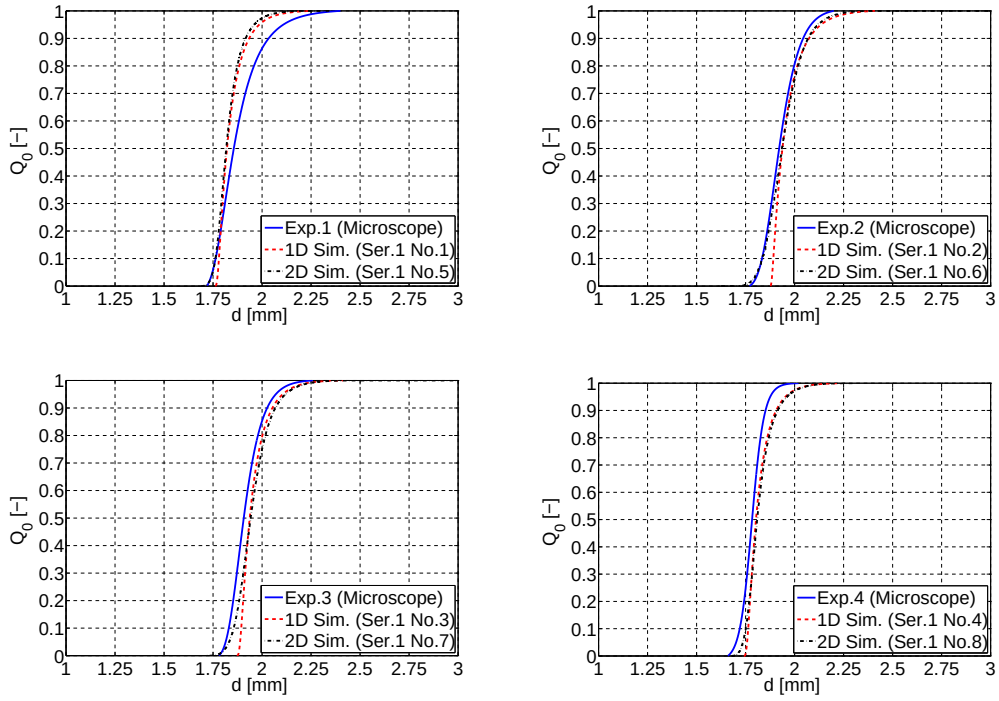

Figure 4.4: Comparison of particle size distributions simulated by 1D- and 2D-PBC model with experimental data from the microscope.

From the above, it can be concluded that both 1D- and 2D-PBC models can well predict the PSD at the outlet when the feed particles have a relatively small variance in particle size. However, when the input PSD is broad, the 2D-PBC model will be better able to estimate and assess the PSD at the outlet.

4.4.3 Parametric study

Six series of parameter studies have been carried out on the basis of the developed coating models. An overall summary of the major operating parameters of all series is presented in Table 4.4. As can be seen, the effect of varying several parameters (internal baffles (Ser. 1), outlet weir (Ser. 2), bed length/width

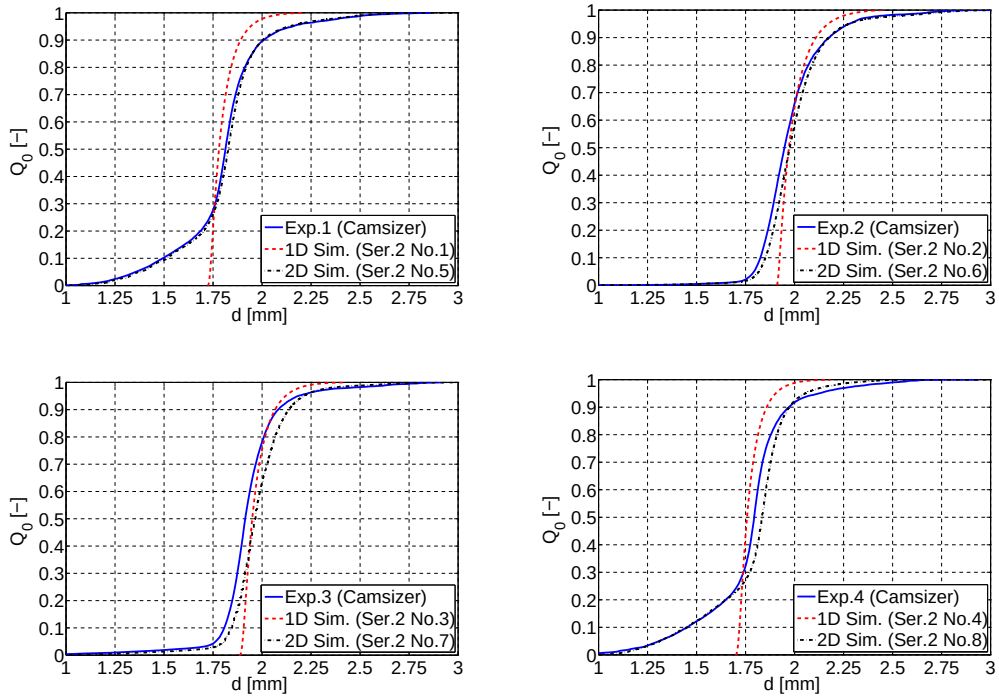

Figure 4.5: Comparison of particle size distributions simulated by 1D- and 2D-PBC model with experimental data from the Camsizer.

Table 4.3: A summary of the median diameter, mean diameter and standard deviation of the particle size distribution at the outlet from different models.

	Microscope						
	1D				2D		
Ser. 1 No.	$d_{p,median}$ [mm]	$d_{p,mean}$ [mm]	σ [mm]	Ser. 1 No.	$d_{p,median}$ [mm]	$d_{p,mean}$ [mm]	σ [mm]
1	1.82	1.84	0.070	5	1.82	1.83	0.067
2	1.94	1.96	0.082	6	1.94	1.95	0.095
3	1.94	1.96	0.073	7	1.94	1.95	0.089
4	1.80	1.82	0.065	8	1.81	1.82	0.071
	Camsizer						
	1D				2D		
Ser. 2 No.	$d_{p,median}$ [mm]	$d_{p,mean}$ [mm]	σ [mm]	Ser. 2 No.	$d_{p,median}$ [mm]	$d_{p,mean}$ [mm]	σ [mm]
1	1.780	1.802	0.069	5	1.827	1.807	0.222
2	1.971	1.997	0.084	6	1.976	2.002	0.172
3	1.950	1.972	0.073	7	1.965	1.977	0.163
4	1.756	1.776	0.063	8	1.834	1.783	0.219

Table 4.4: Summary of all important operating parameters of all series of the parametric study.

ID [−]	T_g [°C]	u_g [ms^{-1}]	$\dot{M}_p$ [kgmin^{-1}]	L_b/W_b [−]	$\tilde{H}_{weir}$ [mm]	N_{baffle} [−]	$\tilde{H}_{gap}$ [mm]
Benchmarks							
BM1(Exp. 1)	85	1.95	1.0	5	95	0	-
BM2(Exp. 2)	85	1.95	1.0	5	175	0	-
Ser. 1: Effect of internal baffles							
PS1	85	1.95	1.0	5	95	3	0
PS2	85	1.95	1.0	5	95	6	0
PS3	85	1.95	1.0	5	95	3	6
PS4	85	1.95	1.0	5	95	6	6
PS5	85	1.95	1.0	5	175	3	0
PS6	85	1.95	1.0	5	175	6	0
PS7	85	1.95	1.0	5	175	9	0
PS8	85	1.95	1.0	5	175	3	6
PS9	85	1.95	1.0	5	175	6	6
PS10	85	1.95	1.0	5	175	9	6
Ser. 2: Effect of outlet weir height							
PS11	85	1.95	1.0	5	215	0	-
PS12	85	1.95	1.0	5	135	0	-
PS13	85	1.95	1.0	5	95	0	-
Ser. 3: Effect of bed length/width ratio							
PS14	85	1.95	1.0	7	175	0	-
PS15	85	1.95	1.0	6	175	0	-
PS16	85	1.95	1.0	4	175	0	-
Ser. 4: Effect of gas temperature							
PS17	125	1.95	1.0	5	175	0	-
PS18	105	1.95	1.0	5	175	0	-
PS19	65	1.95	1.0	5	175	0	-
Ser. 5: Effect of superficial gas velocity							
PS20	85	2.15	1.0	5	175	0	-
PS21	85	1.75	1.0	5	175	0	-
PS22	85	1.55	1.0	5	175	0	-
Ser. 6: Effect of solid mass flow rate							
PS23	85	1.95	0.5	5	175	0	-
PS24	85	1.95	0.75	5	175	0	-
PS25	85	1.95	1.25	5	175	0	-
PS26	85	1.95	1.5	5	175	0	-
PS27	85	1.95	1.75	5	175	0	-
PS28	85	1.95	2.0	5	175	0	-

ratio (Ser. 3), gas temperature (Ser. 4), superficial gas velocity (Ser. 5), and solid feed rate (Ser. 6)) on the PSD at the outlet has been tested. Two experiments have been selected as the setting references of each series of parameter study: the settings of Exp. No. 1 (BM1) and Exp. No. 2 (BM2) have been applied as benchmarks for the first series of parameter study (Ser. 1); On the other hand, Exp. No. 2 (BM2) was selected as the benchmark for the rest of the series (Ser. 2 to Ser. 6).

The effects of installing over- or underflow internal baffles as well as of changing the number of internal baffles have been firstly investigated. Here, the PSD of the washed particle from the microscope was used, and both 1D and 2D models have been simulated. Table 4.5 shows the simulation results of the parameter study Ser. 1. It appears that the mean diameter of the product does not change by adding internal baffles, no matter whether with overflow or underflow. Nevertheless, as plotted in Figs. 4.6(a) and 4.6(b), the standard deviation of the PSD decreases with increasing number of internal baffles. Besides, the standard deviation of the PSD from the 1D model is always smaller than the corresponding value from the 2D model when the height of the outlet weir is 175 mm. However, 2D size variance can be either higher or lower than 1D size variance when the outlet is lower (95 mm), which has also been observed during model validation. One possible explanation for this is that the distribution of the initial particle size is too insignificant when the outlet weir height is 95 mm, and the spread of the RTD has a more significant impact.

Table 4.5: A summary of the mean diameter and standard deviation from all simulations of parameter study Ser. 1.

$\tilde{H}_{weir}$: 95 mm					$\tilde{H}_{weir}$: 175 mm				
	1D-PBC		2D-PBC			1D-PBC		2D-PBC	
ID	$d_{p,mean}$ [mm]	σ [mm]	$d_{p,mean}$ [mm]	σ [mm]	ID	$d_{p,mean}$ [mm]	σ [mm]	$d_{p,mean}$ [mm]	σ [mm]
BM1	1.84	0.070	1.83	0.067	BM2	1.96	0.082	1.95	0.095
PS1	1.84	0.061	1.83	0.060	PS5	1.96	0.073	1.95	0.089
PS2	1.84	0.049	1.83	0.051	PS6	1.96	0.062	1.95	0.082
PS3	1.84	0.063	1.83	0.061	PS7	1.96	0.054	1.95	0.078
PS4	1.84	0.042	1.83	0.045	PS8	1.96	0.071	1.95	0.088
					PS9	1.96	0.059	1.95	0.081
					PS10	1.96	0.051	1.95	0.077

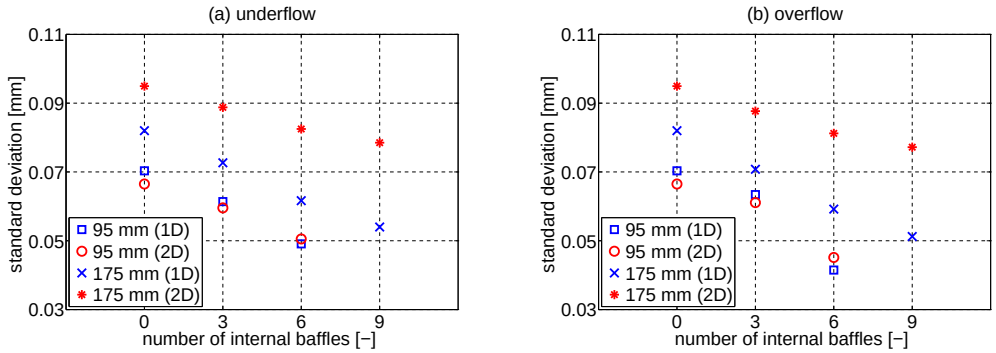

Figure 4.6: Model-based investigation of the influence of the number of internal baffles on the standard deviation of PSD at the outlet when the baffles are respectively installed in (a) underflow or (b) overflow configuration.

In the other five series of the parameter study, the measured PSD of washed particles from the Camsizer of experiment No. 2 was applied as the initial condition, and all the simulations were carried out based on the 2D model. The calculated mean diameters and standard deviations are summarized in Table 4.6.

As seen from the results of the second series of the parameter study, the average particle size at the outlet stays unchanged when changing the height of the outlet weir. Because, although the mean residence time of particles increases with increasing the outlet weir height, the total number of particles in the bed also increases. Besides, an increase of outlet weir height could result in a higher particle back-mixing effect, which causes a broader spread of PSD at the outlet (Fig. 4.7(a)).

The ratio between length and width of the fluidized bed is in the focus of the parameter study in Ser. 3. The width of the bed was fixed at 200 mm for all simulations in this series, that is, only the length of the bed was varied. The relationships between the ratio length/width and the mean diameter as well as the standard deviation are plotted in Figs. 4.7(b) and 4.7(c). It can be inferred that the mean value and the standard deviation of the PSD both decrease with increasing aspect ratio (length/width) of the bed.

Although coating models have been developed based on pure particle growth in this study, since the gas temperature can influence the properties of process gas, which are related to the hydrodynamic properties of the particles as well as the coating layer porosity, the effect of changing gas temperature was studied

Table 4.6: A summary of the mean diameter and standard deviation from all simulations of Ser. 2 to Ser. 6 of the parameter study.

Ser. 2			Ser. 3		
ID	$d_{p,mean}$ [mm]	σ [mm]	ID	$d_{p,mean}$ [mm]	σ [mm]
PS11	2.002	0.173	PS14	1.996	0.169
BM2	2.002	0.172	PS15	1.999	0.170
PS12	2.002	0.170	BM2	2.002	0.172
PS13	2.002	0.168	PS16	2.007	0.175
Ser. 4			Ser. 5		
ID	$d_{p,mean}$ [mm]	σ [mm]	ID	$d_{p,mean}$ [mm]	σ [mm]
PS17	1.996	0.169	PS20	2.000	0.173
PS18	1.998	0.170	BM2	2.002	0.172
BM2	2.002	0.172	PS21	2.004	0.173
PS19	2.009	0.175	PS22	2.007	0.173
Ser. 6					
ID	$d_{p,mean}$ [mm]	σ [mm]	ID	$d_{p,mean}$ [mm]	σ [mm]
PS23	2.078	0.228	PS26	1.973	0.160
PS24	2.029	0.188	PS27	1.964	0.157
BM2	2.002	0.172	PS28	1.958	0.155
PS25	1.985	0.164			

in Ser. 4 of the parameter study and the corresponding results can be found in Figs. 4.7(d) and 4.7(e). The mean particle size decreases by raising the temperature of process gas, which could be due to the porosity of the coating layer becoming smaller when the temperature is higher (according to Eqs. 4.16 and 4.17). Additionally, a decrease in the standard deviation of the PSD can also be achieved by increasing the process gas temperature.

Parameter study in Ser. 5 investigated the influence of the superficial gas velocity. It seems that the average size of the products would become smaller by increasing the gas velocity (Fig. 4.7(f)). Nevertheless, the variation of gas velocity does not have much influence on the mean diameter of the product.

The last series in the parameter study focused on the effect of varying solid feed rate on PSD at the outlet, and Figs. 4.7(g) and 4.7(h) show respectively how the mean diameter and the standard deviation would change with increasing solid flow rate. A decrease in average size reduction and gradually narrower

distributions of particle size can be observed when increasing the feed rate of solids. The effect of solids flow rate on these two properties is non-linear.

4.5 Conclusion

The focus of this chapter was on the modeling of the particle coating process in a horizontal fluidized bed. Results of four coating experiments from the previous work of our group were selected as references for further model validation. These experiments were performed in a pilot-scale horizontal fluidized bed with the same operation parameters but different equipment configurations (e.g., different heights of outlet weir, presence/absence of internal baffles of either underflow or overflow geometry). In each experiment, γ-Al_2O_3 particles were coated with sodium benzoate solution, and a sample was taken at the outlet of the fluidized bed at the end of the experiment. The samples were subjected to microscope and Camsizer measurements, and respective PSDs at the outlet have been obtained. Each sample was washed, dried, and analyzed afterward using the same methods. Accordingly, the PSDs obtained with the washed particles can be regarded as the distributions of particle size at the inlet. It can be observed that PSDs obtained from the Camsizer are much broader than the corresponding curves measured by the microscope, which is due to fact that the particles analyzed by the microscope were manually selected with pseudo-random behavior. Nevertheless, in general, no matter whether the PSD was measured with the microscope or the Camsizer, the PSD at the outlet is always wider than the initial PSD.

Further, a 1D-PBC model has been developed based on the pure particle coating approach and population balance theories. Since a distribution of residence time of goods always arises during continuous processing in the horizontal fluidized bed, the 1D-PBC model considered the RTD as its only property coordinate. However, based on the experimental data, a variety of particle sizes already exist in the feed. Therefore, size was added as a secondary property coordinate of the population, and accordingly, a 2D-PBC model was developed. Two simulation series were then conducted with the obtained PSDs of the feed, and the simulation results were compared with the outlet PSDs. The results indicate that both the 1D- and the 2D-PBC model can well predict the coating process of the particulate goods when the PSD of the feed is relatively narrow. On the contrary, when the PSD is broad at the inlet, simulation results

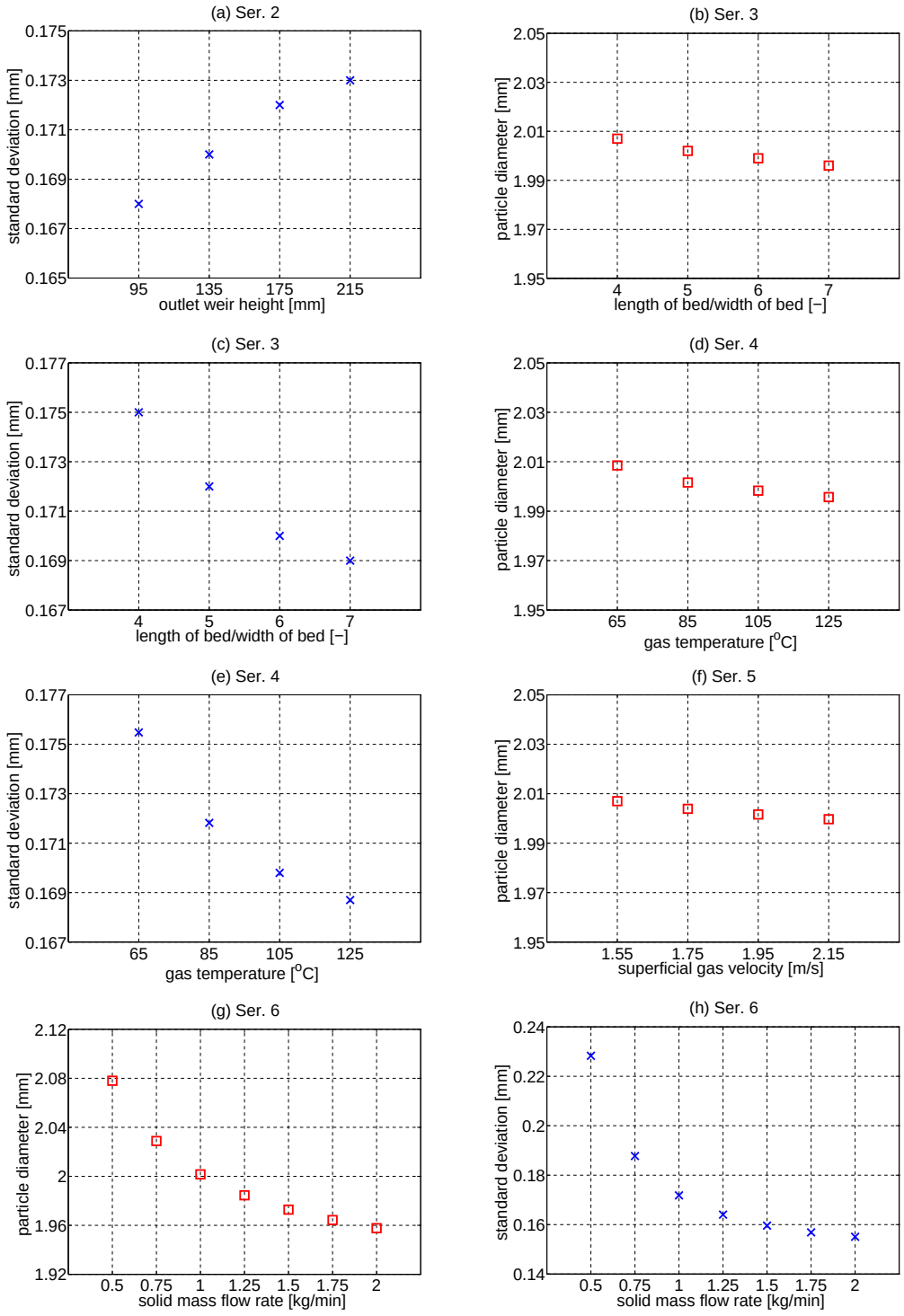

Figure 4.7: Relationships between different operation parameters and product properties based on simulation results from Ser. 2 to Ser. 6 of the parameter study: (a) outlet weir height and standard deviation; (b) length/width ratio and mean diameter; (c) length/width ratio and standard deviation; (d) gas temperature and mean diameter; (e) gas temperature and standard deviation; (f) superficial gas velocity and mean diameter; (g) solid mass flow rate and mean diameter; (h) solid mass flow rate and standard deviation.

by the 2D-PBC model are much more accurate.

After validation of the models, six series of parametric studies have been carried out with them. The influences of different operating parameters as well as of a variety of geometries of the process chamber on the PSD of the final product were investigated, and the following conclusions have been drawn:

- The average size of the product will not be influenced by adding internal baffles or increasing the height of the outlet weir;
- An increase in the number of internal baffles can reduce the spread of the PSD at the outlet, but a higher outlet weir will have the opposite effect;
- Both, the mean and the standard deviation of the PSD will decrease with increasing the length/width ratio of the fluidized bed; higher process gas temperature would have the same effect;
- The spread of PSD will not be influenced by changing superficial gas velocity. However, the mean diameter of particles decreases with increasing the velocity of process gas;
- The solid feed rate has a significant influence on the mean and standard deviation of product size. Both properties will increase with decreasing solids mass flow rate.

Chapter 5

Summary and Outlook

5.1 Summary

Horizontal fluidized bed is a type of continuously operated apparatus which has been successfully applied in industry for a variety of purposes. Taking a long-term view, the main goal of the present work was to reproduce some real processes operated in the horizontal fluidized bed using numerical tools as precisely as possible. This can significantly support the thorough understanding as well as the further innovation of continuous fluidized bed systems. Three particle related topics, RTD, drying, and coating, are involved in the main body of this dissertation. These topics appear independent, however, it should be stressed that they are closely interrelated.

A distribution of residence time among particles, which can directly affect the corresponding drying or coating process, is a common phenomenon in the horizontal fluidized bed. Thus, the performance of the apparatus can accordingly be characterized by the RTD curve. From the perspective of modeling, the RTD information needs to be implemented explicitly in some models, for instance, in the presented PBD and PBC models. Hence, an exhaustive study of particle RTD in horizontal fluidized bed was firstly required. In this work, three different strategies that can be used to acquire RTD data are described. Experiment is usually the most direct way to acquire RTD information, and thus it was also applied and analyzed first. On the basis of the experimentally measured particle RTDs, several important quantities such as the mean and variance, the number of theoretical tanks, the dispersion coefficient, as well as the Bodenstein number, which are all important for further model development, were obtained by means of mathematical methods. Moreover, experimentally measured particle RTD data sets can be applied

for model validation. It can be summarized that, no matter whether with wet or dry particles, the presence of a certain number of internal baffles in the horizontal fluidized bed can reduce the spread of residence time without influencing the mean residence time. The second approach made use of the CFD tools to simulate the particle RTD. Two alternative methods, the species method and the multi-solid method, were proposed. The simulation results indicated that both methods can adequately estimate the particle RTD of the pilot-scale horizontal fluidized bed, which implies that CFD has the potential of also simulating the long-term unsteady process. Moreover, the CFD simulation was found to be able to provide additional information regarding the gas-solid flow in the fluidized bed. For example, it enables to distinguish between macroscopic dispersion coefficients and microscopic diffusivity of particles and study their interrelation; the particle flow in the first compartment of the horizontal fluidized bed installed with internal baffles was found to be close to the behavior of one ideal CSTR. Lastly, it has been shown that particle RTD can be relatively accurately estimated by combining empirical correlations from the recent literature with mathematical models (e.g., the dispersion model solved with the predicted dispersion coefficient and bed mass). However, it was also recognized that RTD related properties calculated from the empirical correlations may differ from the actual value in some cases, and these values can only be corrected based on experimental data.

In general, the information about particle RTD in the pilot-scale horizontal fluidized bed can be accurately captured with various methods and processed for the next stage of this study, the numerical modeling of two different industrial processes that use a horizontal fluidized bed. The first process is drying in a horizontal fluidized bed dryer. In order to treat this process, a fluidized bed drying model was firstly presented based on the principle of single particle drying kinetics. Then, the movement of particles in the horizontal fluidized bed was considered, and different assumptions were respectively added to the drying model. Consequently, in total five models were developed. From the perspective of particle mean moisture content, the different features of each model were demonstrated. The PF model can describe the particle drying process along the fluidized bed from inlet to outlet and predicts the lowest particle mean moisture content at the outlet. Contrariwise, the highest mean moisture content of the product is simulated when the CSTR model is applied. Between these two limit cases, the TISMF model, 1D-PBD model, and 2D-PBD model all can

estimate the mean moisture content of the dried particles with relatively high accuracy. Additionally, this study was one of the first to focus on the spread of the particle moisture content distribution. A distribution of particle moisture content has always been observed in every sample from any reference drying experiment. By means of population balance approach, the 1D-PBD model and 2D-PBD model both not only can simulate particle mean moisture content but also reflect the spread of residual particle moisture distribution. Notably, the obtained outlet particle moisture content distributions from the 2D-PBD model agree well with the experimental data, since this model considers the influences of the particle RTD as well as of the moisture content distribution in the feed material.

Another essential application of the horizontal fluidized bed is the spray coating of particulate materials. In the present study, two properties, the particle mean diameter and the standard deviation of the PSD, which are directly related to the quality of coated particles have been investigated. By referring to the successful experience of using population balance theories to simulate the horizontal fluidized bed dryer, the 1D-PBC model, which implements the single particle growth model with particle RTD information, was established. The simulation results indicated that the 1D-PBC model can well predict the PSD of coated particles when the PSD of feed particles is relatively narrow. However, when the input PSD is getting broader, the simulated spread of coated PSD starts to differ significantly from measured data, even though the mean diameter is still met quite accurately. Hence, the 2D-PBC model, in which the particle size and residence time are specified for each particle class, has been derived. The outlet PSDs obtained with the 2D-PBC model agree well with the experimental results and are not influenced by the inlet PSD any more. After development of various models and validation, several series of model-based numerical experiments were finally conducted based on the PF model, the 2D-PBD model, and the 2D-PBC model, respectively. So far, the adequate modeling of particle drying and formulation processes in the horizontal fluidized bed, which had been the primary purposes of this study, have been achieved.

5.2 Outlook

This work began with the investigation of particle RTD in the horizontal fluidized bed. However, only mono-disperse particles (particles and tracer with the same properties) were used, and the material was relatively large (Geldart classification group D). Future work should address the RTD characteristics of small as well as poly-disperse particles, especially employing CFD tools, which could offer decisive support to designing and developing of industrial continuous fluidized bed equipment.

Several horizontal fluidized bed dryer models have been developed based on given RTD data from different methods. However, apart from the PF model, all the other models can only simulate the status of dried particles at the outlet, and the PF model was also developed by assuming an ideal particle flow pattern. In order to gain a more accurate understanding and insight on the drying process of particles moving along the horizontal fluidized bed, the following aspects could be considered in future work: (a) Specified experiments that can directly measure interior particle RTD should be conducted; (b) The back-flow effect of particles based on empirical correlations, for instance, the back-flow rate suggested by Roemer and Durbin (1967), should be implemented into the PF model; (c) Since the species method cannot fully and accurately provide internal RTD information, the multi-solid method seems to be the only alternative which should be able to predict the internal RTD information using Eulerian multiphase approach in CFD.

All the simulations of particle coating in the present study have neglected the drying of the sprayed solution on the particle surface, which might influence the coating process beyond the considered influence of global drying efficiency on coating layer porosity. Hence, a next step in improving the current coating models could be to consider the effect of drying, including the degree of surface wetness (Heinrich and Mörl (1999)), which would open the way for upgrading the population balance coating model from 2D to 3D.

Bibliography

Adeosun, J. T. and Lawal, A. (2009). Numerical and experimental studies of mixing characteristics in a T-junction microchannel using residence-time distribution. *Chemical Engineering Science*, 64(10):2422–2432.

Almohammed, N., Alobaid, F., Breuer, M., and Epple, B. (2014). A comparative study on the influence of the gas flow rate on the hydrodynamics of a gas–solid spouted fluidized bed using Euler–Euler and Euler–Lagrange/DEM models. *Powder Technology*, 264:343–364.

Andersson, M., Holmquist, B., Lindquist, J., Nilsson, O., and Wahlund, K.-G. (2000). Analysis of film coating thickness and surface area of pharmaceutical pellets using fluorescence microscopy and image analysis. *Journal of Pharmaceutical and Biomedical Analysis*, 22(2):325–339.

Arnaud, P., Brossard, D., and Chaumeil, J. C. (1998). Effect of the granulation process on nitrofurantoin granule characteristics. *Drug Development and Industrial Pharmacy*, 24(1):57–66.

Bachmann, P. (in preparation). *PhD Thesis (in preparation)*. Ph.d. thesis, Otto-von-Guericke University, Magdeburg.

Bachmann, P., Bück, A., and Tsotsas, E. (2016). Investigation of the residence time behavior of particulate products and correlation for the Bodenstein number in horizontal fluidized beds. *Powder Technology*, 301:1067–1076.

Bachmann, P., Bück, A., and Tsotsas, E. (2017). Experimental investigation and correlation of the Bodenstein number in horizontal fluidized bed with internal baffles. *Powder Technology*, 308:378–387.

Bachmann, P., Chen, K., Bück, A., and Tsotsas, E. (in preparation). Prediction of the particle size and layer thickness distributions in a continuous horizontal fluidized bed coating process. *in preparation*.

Baker, C., Khan, A., Ali, Y., and Damyar, K. (2006). Simulation of plug flow fluidized bed dryers. *Chemical Engineering and Processing*, 45(8):641–651.

Barnocky, G. and Davis, R. H. (1988). Elastohydrodynamic collision and rebound of spheres: Experimental verification. *Physics of Fluids*, 31:1324–1329.

Baskakov, A., Berg, B., Vitt, O., Filippovsky, N., Kirakosyan, V., Goldobin, J., and Maskaev, V. (1973). Heat transfer to objects immersed in fluidized beds. *Powder Technology*, 8(5):273–282.

Basu, P. (1999). Combustion of coal in circulating fluidized-bed boilers: A review. *Chemical Engineering Science*, 54(22):5547–5557.

Benyahia, S., Syamlal, M., and O'Brien, T. J. (2007). Study of the ability of multiphase continuum models to predict core-annulus flow. *AIChE Journal*, 53(10):2549–2568.

Bertin, D. E., Cotabarren, I., Piña, J., and Bucalá, V. (2013). Granule size distribution for a multi-chamber fluidized-bed melt granulator: Modeling and validation using process measurement data. *Chemical Engineering Science*, 104:319–329.

Bertin, D. E., Cotabarren, I. M., Bucalá, V., and Piña, J. (2011). Analysis of the product granulometry, temperature and mass flow of an industrial multichamber fluidized bed urea granulator. *Powder Technology*, 206(1–2):122–131.

Bertin, D. E., Mazza, G. D., Piña, J., and Bucalá, V. (2007). Modeling of an industrial fluidized-bed granulator for urea production. *Industrial & Engineering Chemistry Research*, 46(23):7667–7676.

Bizmark, N., Mostoufi, N., Sotudeh-Gharebagh, R., and Ehsani, H. (2010). Sequential modeling of fluidized bed paddy dryer. *Journal of Food Engineering*, 101(3):303–308.

Bück, A., Palis, S., and Tsotsas, E. (2015). Model-based control of particle properties in fluidised bed spray granulation. *Powder Technology*, 270:575–583.

Bück, A., Peglow, M., Tsotsas, E., Mangold, M., and Kienle, A. (2011). Model-based measurement of particle size distributions in layering granulation processes. *AIChE Journal*, 57(4):929–941.

Burgschweiger, J., Groenewold, H., Hirschmann, C., and Tsotsas, E. (1999). From hygroscopic single particle to batch fluidized bed drying kinetics. *Canadian Journal of Chemical Engineering*, 77:333–341.

Burgschweiger, J. and Tsotsas, E. (2002). Experimental investigation and modelling of continuous fluidized bed drying under steady-state and dynamic conditions. *Chemical Engineering Science*, 57(24):5021–5038.

Chang, J., Yang, S., and Zhang, K. (2011). A particle-to-particle heat transfer model for dense gas–solid fluidized bed of binary mixture. *Chemical Engineering Research and Design*, 89(7):894–903.

Chao, Z., Wang, Y., Jakobsen, J. P., Fernandino, M., and Jakobsen, H. A. (2011). Derivation and validation of a binary multi-fluid Eulerian model for fluidized beds. *Chemical Engineering Science*, 66(16):3605–3616.

Chao, Z., Wang, Y., Jakobsen, J. P., Fernandino, M., and Jakobsen, H. A. (2012a). Investigation of the particle-particle drag in a dense binary fluidized bed. *Powder Technology*, 224(Supplement C):311–322.

Chao, Z., Wang, Y., Jakobsen, J. P., Fernandino, M., and Jakobsen, H. A. (2012b). Multi-fluid modeling of density segregation in a dense binary fluidized bed. *Particuology*, 10(1):62–71.

Christensen, F. N. and Bertelsen, P. (1997). Qualitative description of the Wurster-based fluid-bed coating process. *Drug Development and Industrial Pharmacy*, 23(5):451–463.

Churchill, S. W. and Chu, H. H. (1975). Correlating equations for laminar and turbulent free convection from a horizontal cylinder. *International Journal of Heat and Mass Transfer*, 18(9):1049–1053.

Cody, W. J. (1976). An overview of software development for special functions. In Watson, G. A., editor, *Numerical Analysis*, pages 38–48. Springer, Berlin, Heidelberg.

Cooper, S. and Coronella, C. J. (2005). CFD simulations of particle mixing in a binary fluidized bed. *Powder Technology*, 151(1):27–36.

Daud, W. and Ramli, W. (2008). Fluidized bed dryers — Recent advances. *Advanced Powder Technology*, 19(5):403–418.

Deshmukh, S. S., Sathe, M. J., Joshi, J. B., and Koganti, S. B. (2009). Residence time distribution and flow patterns in the single-phase annular region of annular centrifugal extractor. *Industrial & Engineering Chemistry Research*, 48(1):37–46.

Dewettinck, K. and Huyghebaert, A. (1998). Top-spray fluidized bed coating: Effect of process variables on coating efficiency. *LWT - Food Science and Technology*, 31(6):568–575.

Dewettinck, K. and Huyghebaert, A. (1999). Fluidized bed coating in food technology. *Trends in Food Science & Technology*, 10(4):163–168.

Ding, J. and Gidaspow, D. (1990). A bubbling fluidization model using kinetic theory of granular flow. *AIChE Journal*, 36(4):523–538.

Du, W., Zhang, J., Bao, S., Xu, J., and Zhang, L. (2016). Numerical investigation of particle mixing and segregation in spouted beds with binary mixtures of particles. *Powder Technology*, 301:1159–1171.

Ennis, B. J., Tardos, G., and Pfeffer, R. (1991). A microlevel-based characterization of granulation phenomena. *Powder Technology*, 65(1):257–272.

Ergun, S. (1952). Fluid flow through packed columns. *Chemical Engineering Progress*, 48(2):89–94.

Fogler, H. S. (2006). *Elements of Chemical Reaction Engineering (4th Edition)*. Prentice Hall.

Furimsky, E. (2000). Characterization of cokes from fluid/flexi-coking of heavy feeds. *Fuel Processing Technology*, 67(3):205–230.

Fyhr, C. and Kemp, I. C. (1999). Mathematical modelling of batch and continuous well-mixed fluidised bed dryers. *Chemical Engineering and Processing*, 38(1):11–18.

Geldart, D. (1973). Types of gas fluidization. *Powder Technology*, 7(5):285–292.

Geldart, D. (1986a). Characterization of fludized powders. In Geldart, D., editor, *Gas Fluidization Technology*, pages 33–51. John Wiley & Sons.

Geldart, D. (1986b). Introduction. In Geldart, D., editor, *Gas Fluidization Technology*, pages 1–11. John Wiley & Sons.

Gelderbloom, S. J., Gidaspow, D., and Lyczkowski, R. W. (2004). CFD simulations of bubbling/collapsing fluidized beds for three Geldart groups. *AIChE Journal*, 49(4):844–858.

Gera, D., Syamlal, M., and O'Brien, T. J. (2004). Hydrodynamics of particle segregation in fluidized beds. *International Journal of Multiphase Flow*, 30(4):419–428.

Gidaspow, D. (1994). Kinetic theory approach. In *Multiphase Flow and Fluidization*, pages 239–296. Academic Press.

Gidaspow, D., Bezburuah, R., and Ding, J. (1991). Hydrodynamics of circulating fluidized beds: Kinetic theory approach. In *7th International Conference on Fluidization*, Gold Coast (Australia).

Glück, B. (1986). *Zustands- und Stoffwerte - Wasser, Dampf, Luft - Verbrennungsrechnung*. Verlag für Bauwesen GmbH Berlin.

Gnielinski, V. (1980). Wärme- und Stoffübertragung in Festbetten. *Chem.-Ing.-Tech.*, 52(3):228–236.

Grace, J. R. (1986). Contacting modes and behaviour classification of gas-solid and other two-phase suspensions. *Canadian Journal of Chemical Engineering*, 64:353–363.

Grace, J. R. (1990). High-velocity fluidized bed reactors. *Chemical Engineering Science*, 45(8):1953–1966.

Grasa, G. and Abanades, J. C. (2002). The use of two different models to describe the axial mixing of solids in fluidised beds. *Chemical Engineering Science*, 57(14):2791–2798.

Groenewold, H. and Tsotsas, E. (1997). A new model for fluid bed drying. *Drying Technology*, 15(6-8):1687–1698.

Groenewold, H. and Tsotsas, E. (1999). Predicting apparent Sherwood numbers for fluidized beds. *Drying Technology*, 17(7-8):1557–1570.

Groenewold, H. and Tsotsas, E. (2001). Experimental investigation and modeling of the influence of indirect heating on fluidized bed drying. *Drying Technology*, 19(8):1739–1754.

Hampel, N., Bück, A., Peglow, M., and Tsotsas, E. (2013). Continuous pellet coating in a Wurster fluidized bed process. *Chemical Engineering Science*, 86:87–98.

Hede, P. D., Bach, P., and Jensen, A. D. (2008). Top-spray fluid bed coating: Scale-up in terms of relative droplet size and drying force. *Powder Technology*, 184(3):318 – 332.

Hede, P. D., Bach, P., and Jensen, A. D. (2009). Batch top-spray fluid bed coating: Scale-up insight using dynamic heat- and mass-transfer modelling. *Chemical Engineering Science*, 64(6):1293–1317.

Heinrich, S. and Mörl, L. (1999). Fluidized bed spray granulation—A new model for the description of particle wetting and of temperature and concentration distribution. *Chemical Engineering and Processing*, 38(4):635–663.

Heinrich, S., Peglow, M., Ihlow, M., Henneberg, M., and Mörl, L. (2002). Analysis of the start-up process in continuous fluidized bed spray granulation by population balance modelling. *Chemical Engineering Science*, 57(20):4369–4390.

Herzog, N., Schreiber, M., Egbers, C., and Krautz, H. J. (2012). A comparative study of different CFD-codes for numerical simulation of gas-solid fluidized bed hydrodynamics. *Computers & Chemical Engineering*, 39:41–46.

Hoffmann, T., Rieck, C., Schmidt, M., Bück, A., Peglow, M., and Tsotsas, E. (2015). Prediction of shell porosities in continuous fluidized bed spray layering. *Drying Technology*, 33(13):1662–1670.

Horio, M., Nonaka, A., Hoshiba, M., Morishita, K., Kobukai, Y., Naito, J., Tachibana, O., Watanabe, K., and Yoshida, N. (1986). Coal combustion in a transparent circulating fluidized bed. In Basu, P., editor, *Circulating Fluidized Bed Technology*, pages 255 – 262. Pergamon, Oxford.

Hua, L., Wang, J., and Li, J. (2014). CFD simulation of solids residence time distribution in a CFB riser. *Chemical Engineering Science*, 117:264–282.

Jiang, Z., Bück, A., and Tsotsas, E. (2017). CFD-DEM study of residence time, droplet deposition, and collision velocity for a binary particle mixture in a Wurster fluidized bed coater. *Drying Technology*, 36(6):638–650.

Jones, D. M. (1988). Controlling particle size and release properties: Secondary processing techniques. In Risch, S. J. and Reineccius, G. A., editors, *Flavor Encapsulation*, chapter 17, page 158–176. American Chemical Society.

Kerkhof, P. J. A. M. (1994). The role of theoretical and mathematical modeling in scale-up. *Drying Technology*, 12(1-2):1–46.

Khanali, M., Rafiee, S., Jafari, A., and Banisharif, A. (2012). Study of residence time distribution of rough rice in a plug flow fluid bed dryer. *International Journal of Advanced Science and Technology*, 48:103–114.

Khanali, M., Rafiee, S., Jafari, A., and Hashemabadi, S. H. (2013). Experimental investigation and modeling of plug-flow fluidized bed drying under steady-state conditions. *Drying Technology*, 31(4):414–432.

Khongprom, P., Aimdilokwong, A., Limtrakul, S., Vatanatham, T., and Ramachandran, P. A. (2012). Axial gas and solids mixing in a down flow circulating fluidized bed reactor based on CFD simulation. *Chemical Engineering Science*, 73(Supplement C):8–19.

Kolhe, N., Mirage, Y., Patwardhan, A., Rathod, V., Pandey, N., Mudali, U. K., and Natarajan, R. (2011). CFD and experimental studies of single phase axial dispersion coefficient in pulsed sieve plate column. *Chemical Engineering Research and Design*, 89(10):1909–1918.

Koller, D., Hannesschläger, G., Leitner, M., and Khinast, J. (2011). Non-destructive analysis of tablet coatings with optical coherence tomography. *European Journal of Pharmaceutical Sciences*, 44(1):142–148.

Kristensen, J. and Hansen, V. (2006). Wet granulation in rotary processor and fluid bed: Comparison of granule and tablet properties. *AAPS PharmSciTech*, 7(1):E153–E162.

Kunii, D. and Levenspiel, O. (1991). *Fluidization Engineering*. Butterworth-Heinemann, 2nd edition.

Laksmana, F. L., van Vliet, L. J., Hartman Kok, P. J. A., Vromans, H., Frijlink, H., and van der voort Maarschalk, K. (2009). Quantitative image analysis for evaluating the coating thickness and pore distribution in coated small particles. *Pharmaceutical Research*, 26(4):965–976.

Launder, B. and Spalding, D. (1972). *Lectures in Mathematical Models of Turbulence*. Academic Press.

Léonard, A., Crine, M., and Stepanek, F. (2008). Use of x-ray tomography for drying-related applications. In Tsotsas, E. and Mujumdar, A. S., editors, *Modern Drying Technology*, volume 2, pages 143–186. Wiley-VCH, Weinheim.

Levenspiel, O. (1999). *Chemical Reaction Engineering (3rd Edition)*. John Wiley & Sons.

Levenspiel, O. (2012). *Tracer Technology: Modeling the Flow of Fluids*. Springer, New York.

Liu, Y., Lan, X., Xu, C., Wang, G., and Gao, J. (2012). CFD simulation of gas and solids mixing in FCC strippers. *AIChE Journal*, 58(4):1119–1132.

Lun, C. K. K., Savage, S. B., Jeffrey, D. J., and Chepurniy, N. (1984). Kinetic theories for granular flow: Inelastic particle in Couette flow and slightly inelastic particle in a general flowfield. *Journal of Fluid Mechanics*, 140:223–256.

Maa, Y.-F., Nguyen, P.-A., and Hsu, C. C. (1996). Spray-coating of rhDNase on lactose: Effect of system design, operational parameters and protein formulation. *International Journal of Pharmaceutics*, 144(1):47–59.

MacMullin, R. and Weber, M. (1935). The theory of short-circuiting in continuous-flow mixing vessels in series and kinetics of chemical reactions in such systems. *Transactions of American Institute of Chemical Engineers*, 31(2):409–458.

Martin, H. (2010). *VDI Heat Atlas (2nd Edition): Heat transfer in fluidized beds*, chapter M5, pages 1301–1309. Springer.

Mckay, G. (1988). Fluidized bed adsorption of pollutants on to activated carbon. *Chemical Engineering Journal*, 39(2):87–96.

Müller, D., Bück, A., and Tsotsas, E. (2019). Influence of separation properties and processing strategies on product characteristics in continuous fluidized bed spray granulation. *Powder Technology*, 342:572–584.

Mori, S. and Wen, C. Y. (1975). Estimation of bubble diameter in gaseous fluidized beds. *AIChE Journal*, 21(1):109–115.

Mörl, L., Heinrich, S., and Peglow, M. (2007). Chapter 2: Fluidized bed spray granulation. In Salman, A., Hounslow, M., and Seville, J., editors, *Granulation*, volume 11 of *Handbook of Powder Technology*, pages 21–188. Elsevier Science B.V.

Morris, A. J. and Jensen, R. F. (1976). Fluidized-bed chlorination rates of Australian rutile. *Metallurgical and Materials Transactions B*, 7:89–93.

Murphree, E. V., Brown, C. L., Fischer, H. G. M., Gohr, E. J., and Sweeney, W. J. (1943). Fluid catalyst process. catalytic cracking of petroleum. *Industrial & Engineering Chemistry*, 35(7):768–773.

Nilsson, L. and Wimmerstedt, R. (1988). Residence time distribution and particle dispersion in a longitudinal-flow fluidized bed. *Chemical Engineering Science*, 43(5):1153–1160.

Ogawa, S., Umemura, A., and Oshima, N. (1980). On the equations of fully fluidized granular materials. *Journal of Applied Mathematics and Physic (ZAMP)*, 31(4):483–493.

Palamanit, A., Prachayawarakorn, S., Tungtrakul, P., and Soponronnarit, S. (2016). Performance evaluation of top-spray fluidized bed coating for healthy coated rice production. *Food and Bioprocess Technology*, 9(8):1317–1326.

Palzer, S. (2007). Agglomeration of dehydrated consumer foods. In Salman, A., Hounslow, M., and Seville, J., editors, *Handbook of Powder Technology: Granulation*, pages 591–671. Elsevier. B. V.

Peglow, M., Antonyuk, S., Jacob, M., Palzer, S., Heinrich, S., and Tsotsas, E. (2008a). Particle formulation in spray fluidized beds. In Tsotsas, E. and Mujumdar, A. S., editors, *Modern Drying Technology*, volume 3, pages 295–378. Wiley-VCH, Weinheim.

Peglow, M., Cunäus, U., and Tsotsas, E. (2011). An analytical solution of population balance equations for continuous fluidized bed drying. *Chemical Engineering Science*, 66(9):1916–1922.

Peglow, M., Metzger, T., Lee, G., Schiffter, H., Hampel, R., Heinrich, S., and Tsotsas, E. (2008b). Measurement of average moisture content and drying kinetics for single particles, droplets and dryers. In Tsotsas, E. and Mujumdar, A. S., editors, *Modern Drying Technology*, volume 2, pages 1–71. Wiley-VCH, Weinheim.

Poling, B. E., Prausnitz, J. M., and O'Connell, J. P. (2000). *The Properties of Gases and Liquids (5th Edition)*. McGraw-Hill.

Pronk, P. (2006). *Fluidized bed heat exchangers to prevent fouling in ice slurry systems and industrial crystallizers*. PhD thesis, Delft University of Technology.

Reay, D. (1978). Particle residence time distribution in plug-flow fluid bed dryers. In *Proceedings of 1st Internation Drying Symposium*, Montreal, Canada.

Reh, L. (1977). Trends in research and industrial application of fluidization. *Verfahrenstechnik*, 11(6):381–384.

Rieck, C., Hoffmann, T., Bück, A., Peglow, M., and Tsotsas, E. (2015). Influence of drying conditions on layer porosity in fluidized bed spray granulation. *Powder Technology*, 272:120–131.

Roemer, M. H. and Durbin, L. D. (1967). Transient response and moments analysis of backflow cell model for flow systems with longitudinal mixing. *Industrial & Engineering Chemistry Fundamentals*, 6(1):120–129.

Saleh, K. and Guigon, P. (2007). Coating and encapsulation processes in powder technology. In Salman, A., Hounslow, M., and Seville, J., editors, *Handbook of Powder Technology: Granulation*, pages 323–375. Elsevier. B. V.

Satija, S. and Zucker, I. (1986). Hydrodynamics of vibro-fluidized beds. *Drying Technology*, 4(1):19–43.

Saxena, S. C. and Jotshi, C. K. (1994). Fluidized-bed incineration of waste materials. *Prog. Energy Combust. Sci.*, 20:281–324.

Schlünder, E.-U. and Tsotsas, E. (1988). *Wärmeübertragung in Festbetten, durchmischten Schüttgütern und Wirbelschichten*. Georg Thieme Verlag Stuttgart.

Schmidt, M., Bück, A., and Tsotsas, E. (2015a). Experimental investigation of process stability of continuous spray fluidized bed layering with internal separation. *Chemical Engineering Science*, 126:55–66.

Schmidt, M., Rieck, C., Bück, A., and Tsotsas, E. (2015b). Experimental investigation of process stability of continuous spray fluidized bed layering with external product separation. *Chemical Engineering Science*, 137:466–475.

Schulz, H. (1999). Short history and present trends of Fischer-Tropsch synthesis. *Applied Catalysis A: General*, 186(1):3–12.

Shamlou, P. A., Liu, Z., and Yates, J. G. (1990). Hydrodynamic influences on particle breakage in fluidized bed. *Chemical Engineering Science*, 45(4):809–817.

Smolders, K. and Baeyens, J. (2000). Overall solids movement and solids residence time distribution in a CFB-riser. *Chemical Engineering Science*, 55(19):4101–4116.

Sondej, F., Bück, A., Koslowsky, K., Bachmann, P., Jacob, M., and Tsotsas, E. (2015). Investigation of coating layer morphology by micro-computed X-ray tomography. *Powder Technology*, 273:165–175.

Span, R. (2010). Properties of dry air. In VDI-GVC, editor, *VDI Heat Atlas*, chapter D2.2. Springer-Verlag Berlin Heidelberg.

Srinivas, G. and Setty, Y. P. (2013). Drying behavior of uniform and binary mixture of solids in a batch fluidized bed dryer. *Powder Technology*, 241:181–187.

Srinivasan, N. (2002). Reduction of iron oxides by carbon in a circulating fluidized bed reactor. *Powder Technology*, 124(1):28–39.

Srivastava, S. and Mishra, G. (2010). Fluid bed technology: Overview and parameters for process selection. *International Journal of Pharmaceutical Sciences and Drug Research*, 2:236–246.

Stenström, S., Bonazzi, C., and Foucat, L. (2008). Magnetic resonance imaging for determination of moisture profiles and drying curves. In Tsotsas, E. and Mujumdar, A. S., editors, *Modern Drying Technology*, volume 2, pages 91–142. Wiley-VCH, Weinheim.

Stone, H. N., Batchelor, J. D., and Johnstone, H. F. (1954). Low temperature carbonization rates in a fluidized bed. *Industrial & Engineering Chemistry*, 46(2):274–278.

Sun, J. and Battaglia, F. (2006). Hydrodynamic modeling of particle rotation for segregation in bubbling gas-fluidized beds. *Chemical Engineering Science*, 61(5):1470–1479.

Syamlal, M. (1987). The particle-particle drag term in a multiparticle model of fluidization. *Springfield: National Technical Information Service*.

Syamlal, M., Rogers, W., and O'Brien, T. J. (1993). *MFIX Documentation Theory Guide*.

Taghipour, F., Ellis, N., and Wong, C. (2005). Experimental and computational study of gas–solid fluidized bed hydrodynamics. *Chemical Engineering Science*, 60(24):6857–6867.

Tashimo, T., Suto, T., Murota, J., and Kato, K. (1999). Calcination of fine limestone particles by a powder-particle fluidized bed. *Journal of Chemical Engineering of Japan*, 32(3):374–378.

Taylor, G. (1953). Dispersion of soluble matter in solvent flowing slowly through a tube. *Proceedings of the Royal Society of London A: Mathematical, Physical and Engineering Sciences*, 219(1137):186–203.

Teunou, E. and Poncelet, D. (2002). Batch and continuous fluid bed coating – Review and state of the art. *Journal of Food Engineering*, 53(4):325–340.

Tsotsas, E. (1994). From single particle to fluid bed drying kinetics. *Drying Technology*, 12(6):1401–1426.

Tsotsas, E., Heinrich, S., Jacob, M., Peglow, M., and Mörl, L. (2008). Intensification of fluidized-bed processes for drying and formulation. In Tsotsas, E. and Mujumdar, A. S., editors, *Modern Drying Technology*, volume 5, chapter 4, pages 85–130. Wiley-VCH, Weinheim.

Tsotsas, E., Metzger, T., Gnielinski, V., and Schlünder, E.-U. (2010). Drying of solid materials. In *Ullmann's Encyclopedia of Industrial Chemistry*, volume 11, pages 581–619. Wiley-VCH, Weinheim.

Uhlemann, H. (1990). Kontinuierliche Wirbelschicht-Sprühgranulation. *Chemie Ingenieur Technik*, 62(10):822–834.

van Deemter, J. (1980). Mixing patterns in large-scale fluidized beds. In Grace, J. R. and Matsen, J. M., editors, *Fluidization*, pages 69–89. Springer, Boston, MA.

van Meel, D. A. (1958). Adiabatic convection batch drying with recirculation of air. *Chemical Engineering Science*, 9:36–44.

Čatipović, N. M., Jovanović, G. N., and Fitzgerald, T. J. (1978). Regimes of fluidization for large particles. *AIChE Journal*, 24(3):543–547.

Vedantam, S., Joshi, J. B., and Koganti, S. B. (2006). CFD simulation of RTD and mixing in the annular region of a Taylor-Couette contactor. *Industrial & Engineering Chemistry Research*, 45(18):6360–6367.

Vejahati, F., Mahinpey, N., Ellis, N., and Nikoo, M. B. (2009). CFD simulation of gas-solid bubbling fluidized bed: A new method for adjusting drag law. *Canadian Journal of Chemical Engineering*, 87(1):19–30.

Vreman, A., van Lare, C., and Hounslow, M. (2009). A basic population balance model for fluid bed spray granulation. *Chemical Engineering Science*, 64(21):4389–4398.

Vuppala, M. K., Parikh, D. M., and Bhagat, H. R. (1997). Application of powder-layering technology and film coating for manufacture of sustained-release pellets using a rotary fluid bed processor. *Drug Development and Industrial Pharmacy*, 23(7):687–694.

Wagner, N. J., Coertzen, M., Matjie, R., and van Dyk, J. (2008). Coal gasification. In Suárez-Ruiz, I. and Crelling, J. C., editors, *Applied Coal Petrology*, chapter 5, pages 119–144. Elsevier.

Wang, H., Dyakowski, T., Senior, P., Raghavan, R., and Yang, W. (2007). Modelling of batch fluidised bed drying of pharmaceutical granules. *Chemical Engineering Science*, 62(5):1524–1535.

Wanjari, A. N., Thorat, B. N., Baker, C. G. J., and Mujumdar, A. S. (2006). Design and modeling of plug flow fluid bed dryers. *Drying Technology*, 24(2):147–157.

Wen, C. Y. and Yu, Y. H. (1966). Mechanics of fluidization. *Chemical Engineering Progress Symposium Series*, 62:100–111.

Wesdyk, R., Joshi, Y., Jain, N., Morris, K., and Newman, A. (1990). The effect of size and mass on the film thickness of beads coated in fluidized bed equipment. *International Journal of Pharmaceutics*, 65(1):69–76.

Wnukowski, P. and Setterwall, F. (1989). The coating of particles in a fluidized bed (residence time distribution in a system of two coupled perfect mixers). *Chemical Engineering Science*, 44(3):493–505.

Wong, P. M., Chan, L. W., and Heng, P. W. S. (2013). Investigation on side-spray fluidized bed granulation with swirling airflow. *AAPS PharmSciTech*, 14(1):211–221.

Zens, F. A. (1997). Fluidization phenomena and fluidized bed technology. In Fayed, M. E. and Otten, L., editors, *Handbook of Powder Science & Technology*, chapter 9, pages 487–531. Springer, Boston, MA.

Zhang, Y., Wang, Z., Jin, Y., Li, Z., and Yi, W. (2015). CFD simulation and experiment of residence time distribution in short-contact cyclone reactors. *Advanced Powder Technology*, 26(4):1134–1142.

Zhao, Y., Cheng, Y., Wu, C., Ding, Y., and Jin, Y. (2010). Eulerian-Lagrangian simulation of distinct clustering phenomena and RTDs in riser and downer. *Particuology*, 8(1):44–50.

Appendices

A Gas-solid heat and mass transfer in fluidized bed

In this work, the apparent Sherwood number Sh_{app} is calculated according to the model of Groenewold and Tsotsas (1999), which is an extension of the work of Gnielinski (1980), with the following equations:

$$Re^* = \frac{Re_{mf}}{\psi_{mf}} \tag{A.1}$$

$$Sc = LePr \tag{A.2}$$

$$Sh_{lam} = 0.664\sqrt{Re^*}Sc^{1/3} \tag{A.3}$$

$$Sh_{tu} = \frac{0.037\,(Re^*)^{4/5}\,Sc}{1 + 2.443(Re^*)^{-1/10}\,(Sc^{2/3} - 1)} \tag{A.4}$$

$$Sh_{sp} = 2 + \sqrt{Sh_{lam}^2 + Sh_{tu}^2} \tag{A.5}$$

$$Sh_{fb} = (1 + 1.5\,(1 - \psi_{mf}))\,Sh_{sp} \tag{A.6}$$

$$Sh_{app} = \frac{ReSc}{A_V \tilde{H}_b} ln\left(1 + \frac{Sh_{fb} A_V \tilde{H}_b}{ReSc}\right) \tag{A.7}$$

Moreover, the apparent Nusselt number Nu_{app} can also be calculated by substituting the Schmidt number Sc with the Prandt number Pr in Eqs. A.3, A.4 and A.7. Thus, the heat and mass transfer coefficient between gas and solid can be calculated with:

$$\tilde{\alpha}_{gp} = \frac{Nu_{app}\lambda_g}{d_p} \tag{A.8}$$

$$\tilde{\beta}_{pg} = \frac{Sh_{app}\tilde{D}_v}{d_p} \tag{A.9}$$

B Material values

B.1 Properties of dry air

Molecular mass (Span (2010))

$$\tilde{M}_g = 28.9583 \tag{B.1}$$

Unit: kg/kmol

Specific gas constant (Span (2010)):

$$R_g = 287.12 \tag{B.2}$$

Unit: J/(kgK)

Diffusion volume (Poling et al. (2000))

$$V_g = 19.7 \tag{B.3}$$

Unit: $-$

Density (ideal gas law):

$$\rho_g = \frac{101325}{R_g(273.15 + \vartheta_g)} \tag{B.4}$$

Unit: kg/m^3

Dynamic viscosity (Glück (1986))

$$\tilde{\mu}_g = A + B\vartheta_g + C\vartheta_g^2 + D\vartheta_g^3 \tag{B.5}$$

$$A = +1.705568 \cdot 10^{-5}$$

$$B = +4.511012 \cdot 10^{-8}$$

$$C = -8.766234 \cdot 10^{-12}$$

$$D = -3.382035 \cdot 10^{-15}$$

Unit: Pas
Range of application: p = 0.1 MPa; $-20^{o}\text{C} \leq \vartheta_g \leq 200^{o}\text{C}$
Maximum error: 0.6%

Kinematic viscosity

$$\nu_g = \frac{\tilde{\mu}_g}{\rho_g} \tag{B.6}$$

Unit: m^2/s

Heat conductivity (Glück (1986))

$$\tilde{\lambda}_g = A + B\vartheta_g + C\vartheta_g^2 + D * \vartheta_g^3 \tag{B.7}$$

$$A = +2.45211 \cdot 10^{-2}$$

$$B = +7.501414 \cdot 10^{-5}$$

$$C = -2.593344 \cdot 10^{-8}$$

$$D = +5.292884 \cdot 10^{-11}$$

Unit: W/(mK)
Range of application: p = 0.1 MPa; $-20^{o}\text{C} \leq \vartheta_g \leq 200^{o}\text{C}$
Maximum error: 0.08%

Specific heat capacity (Glück (1986))

$$c_g = A + B\vartheta_g + C\vartheta_g^2 + D\vartheta_g^3 \tag{B.8}$$

$$A = +1006.256$$

$$B = -2.120536 \cdot 10^{-2}$$

$$C = -4.180195 \cdot 10^{-4}$$

$$D = +1.521916 \cdot 10^{-7}$$

Unit: J/(kgK)
Range of application: p = 0.1 MPa; $-20^{o}\text{C} \leq \vartheta_g \leq 200^{o}\text{C}$
Maximum error: 0.05%

Prandtl number

$$Pr = \frac{\tilde{\mu}_g c_g}{\tilde{\lambda}_g} \tag{B.9}$$

Unit: –

B.2 Properties of wet air

Molecular mass of water (Poling et al. (2000))

$$\tilde{M}_w = 18.015 \tag{B.10}$$

Unit: kg/kmol

Diffusion volume of water (Poling et al. (2000))

$$V_w = 13.1 \tag{B.11}$$

Unit: –

Specific heat capacity of water (Glück (1986))

$$c_w = A + B\vartheta + C\vartheta^2 + D\vartheta^3 \tag{B.12}$$

$$A = +4174.785$$

$$B = +1.785308 \cdot 10^{-2}$$

$$C = -5.097403 \cdot 10^{-4}$$

$$D = +4.216721 \cdot 10^{-5}$$

Unit: J/(kgK)
Range of application: $-20^{\circ}\mathrm{C} \leq \vartheta \leq \vartheta_{sat}(p)$ or 200°C
Maximum error: 0.43%

Diffusion coefficient of water vapor (Poling et al. (2000))

$$\tilde{D}_v = \frac{0.00143\vartheta_g^{1.75}}{p\sqrt{2\left(1/\tilde{M}_w + 1/\tilde{M}_g\right)^{-1}}\left(V_w^{1/3} + V_g^{1/3}\right)^2} \tag{B.13}$$

Unit: m^2/s

Saturated pressure of water vapor (Glück (1986))
The saturated pressure of water vapor is a function of saturated gas temperature:

$$p_{sat} = A\exp\left(\mathrm{B}\vartheta_{\mathrm{sat}} + \mathrm{C}\vartheta_{\mathrm{sat}}^2 + \mathrm{D}\vartheta_{\mathrm{sat}}^3 + \mathrm{E}\vartheta_{\mathrm{sat}}^4\right) \tag{B.14}$$

$$A = +611$$

$$B = +7.257 \cdot 10^{-2}$$

$$C = -2.937 \cdot 10^{-4}$$

$$D = +9.810 \cdot 10^{-7}$$

$$E = -1.901 \cdot 10^{-9}$$

Unit: Pa
Range of application: $0^{\mathrm{o}}\mathrm{C} \leq \vartheta_{sat} \leq 100^{\mathrm{o}}\mathrm{C}$
Maximum error: 0.2%

Lewis number

$$Le = \frac{\tilde{\lambda}_g}{c_g \rho_g \tilde{D}_v} \tag{B.15}$$

Unit: –

Specific heat capacity of water vapor (Glück (1986))

$$c_v = A + B\vartheta + C\vartheta^2 + D\vartheta^3 \tag{B.16}$$

$$A = +1862$$

$$B = +2.858485 \cdot 10^{-1}$$

$$C = +6.148483 \cdot 10^{-4}$$

$$D = -2.060606 \cdot 10^{-7}$$

Unit: J/(kgK)
Range of application: 0.001 MPa $\leq p \leq$ 0.01 MPa; $25^{\mathrm{o}}\mathrm{C} \leq \vartheta_g \leq 400^{\mathrm{o}}\mathrm{C}$
Maximum error: 0.06%